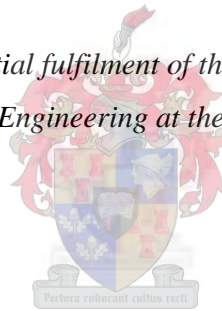# A numerical investigation of air-cooled steam condenser performance under windy conditions

by

Michael Trevor Foxwell Owen

Thesis presented in partial fulfilment of the requirements for the degree
Master of Science in Engineering at the University of Stellenbosch

Supervisor: Prof. Detlev Kröger

Department of Mechanical and Mechatronic Engineering

March 2010

Declaration

By submitting this thesis electronically, I declare that the entirety of the work contained therein is my own, original work, that I am the owner of the copyright thereof (unless to the extent explicitly otherwise stated) and that I have not previously in its entirety or in part submitted it for obtaining any qualification.

Date: 10 February 2010

Abstract

This study is aimed at the development of an efficient and reliable method of evaluating the performance of an air-cooled steam condenser (ACSC) under windy conditions, using computational fluid dynamics (CFD). A two-step modelling approach is employed as a result of computational limitations. The numerical ACSC model developed in this study makes use of the pressure jump fan model, amongst other approximations, in an attempt to minimize the computational expense of the performance evaluation. The accuracy of the numerical model is verified through a comparison of the numerical results to test data collected during full scale tests carried out on an operational ACSC. Good correlation is achieved between the numerical results and test data. Further verification is carried out through a comparison to previous numerical work. Satisfactory convergence is achieved for the most part and the few discrepancies in the results are explained. The effect of wind on ACSC performance at El Dorado Power Plant (Nevada, USA) is investigated and it is found that reduced fan performance due to distorted flow at the inlet of the upstream fans is the primary contributor to the reduction in performance associated with increased wind speed in this case. An attempt is subsequently made to identify effective wind effect mitigation measures. To this end the effects of wind screens, solid walkways and increasing the fan power are investigated. It is found that the installation of an appropriate wind screen configuration provides a useful means of reducing the negative effects of wind on ACSC performance and an improved wind screen configuration is suggested for El Dorado. Solid walkways are also shown to be beneficial to ACSC performance under windy conditions. It is further found that ACSC performance increases with walkway width but that the installation of excessively wide walkways is not justifiable. Finally, increasing the fan power during periods of unfavourable ambient conditions is shown to have limited benefit in this case. The model developed in this study has the potential to allow for the evaluation of large ACSC installations and provides a reliable platform from which further investigations into improving ACSC performance under windy conditions can be carried out.

Opsomming

Hierdie studie is daarop gemik om die ontwikkeling van 'n geskikte en betroubare metode van evaluering van die verrigting van 'n lugverkoelde stoom-kondensator (air-cooled steam condenser, ACSC) onder winderige toestande, met behulp van numeriese vloei-dinamika. 'n Twee-stap modelleringsbenadering is aangewend as gevolg van rekenaar beperkings. Die numeriese ACSC-model wat in hierdie studie ontwikkel is, maak gebruik van die druksprong waaier model, asook ander benaderings, in 'n poging om die berekeningskoste van die verrigting-evaluering te verminder. Die akkuraatheid van die numeriese model is bevestig deur middel van 'n vergelyking van die numeriese resultate met toetsdata ingesamel tydens die volskaal toetse uitgevoer op 'n operasionele ACSC. Goeie korrelasie is bereik tussen die numeriese resultate en toetsdata. Verdere bevestiging is uitgevoer deur middel van 'n vergelyking met vorige numeriese werk. Bevredigende konvergensie is in die algemeen bereik en die paar verskille in die resultate word verduidelik. Die effek van wind op ACSC verrigting by El Dorado Power Plant (Nevada, VSA) is ondersoek, en daar is bevind dat verlaagde waaierverrigting, as gevolg van vervormde vloei by die inlaat van die stroomop waaiers, die primêre bydraer is tot die afname in ACSC werkverrigting geassosieer met verhoogde windsnelheid in hierdie geval. 'n Poging word dan aangewend om effektiewe wind-effek velagingsmaatreëls te identifiseer. Windskerms, soliede wandelvlakke en die verhoging van die waaierkrag word gevolglik ondersoek. Daar is bevind dat die installasie van 'n toepaslike windskerm-opset 'n nuttige middel tot 'n vermindering van die negatiewe effekte van wind op ACSC verrigting bied, en 'n verbeterde windskerm opset is voorgestel vir El Dorado. Soliede wandelvlakke word ook aanbeveel as voordelig vir ACSC verrigting onder winderige toestande. Dit is verder bevind dat die ACSC prestasie verhoog met wandelvlak breedte, maar dat die installasie van 'n te ruim wandelvlak nie regverdigbaar is nie. Ten slotte, word bewys dat die verhoging van die waaierkrag tydens periodes van ongunstige omgewingsomstandighede 'n beperkte voordeel in hierdie geval het. Die model wat ontwikkel is in hierdie studie het die potensiaal om voorsiening te maak vir die evaluering van groot ACSC- installasies en bied 'n betroubare platform vanwaar verdere ondersoeke tot die verbetering van ACSC verrigting onder winderige toestande uitgevoer kan word.

Acknowledgements

I would like to express my sincerest gratitude to the following people/organizations for their contribution towards making this study possible:

Table of contents

List of Figures

List of Tables

Nomenclature

Symbols

A -   Area, m^2

B -   Variable

C -   Constant or inertial loss coefficient, m^{-1}

c -   Specific heat

d -   Diameter, m

E -   East

e -   Effectiveness

F -   Force, N

G -   Turbulent kinetic energy generation,

H -   Height, m

i -   Unit vector or latent heat, J/kg

j -   Unit vector

K -   Loss coefficient

k -   Thermal conductivity, W/mK; turbulent kinetic energy, m^2/s^2; or unit vector

L -   Length, m

m -   Mass flow rate, kg/s

N -   Number, North or fan speed, rpm

Ny -   Characteristic heat transfer parameter, m^{-1}

n -   Number

P -   Power, W

Pr -   Prandtl number

p -   Pressure, N/m^2

Q -   Heat transfer rate, W

Ry -   Characteristic flow parameter, m^{-1}

S -   Source term, South or modulus of the mean strain rate tensor

T -   Temperature, $°C$ or K

TP	-	Test period
U*	-	Function
UA	-	Overall heat transfer coefficient, *W/K*
u	-	x-component of velocity, *m/s*
V	-	Volume, m^3; or volume flow rate, *m^3/s*
v	-	Velocity or y-component of velocity, *m/s*
W	-	West
w	-	z-component of velocity, *m/s*
x	-	Co-ordinate or distance, *m*
Y	-	Approach velocity factor
y	-	Co-ordinate
z	-	Co-ordinate or elevation, *m*

Greek symbols

ϕ	-	Expansion factor
1/α	-	Viscous loss coefficient, *m^{-2}*
β	-	Thermal expansion coefficient, *K^{-1}*
Γ	-	Diffusion coefficient
Δ	-	Change
ε	-	Turbulent energy dissipation rate, *m^2/s^3*
η	-	Efficiency or variable
θ	-	Direction, °
μ	-	Viscosity, *kg/ms*
ρ	-	Density, *kg/m^3*
σ	-	Turbulent Prandtl number or ratio
Φ	-	Energy dissipation term
φ	-	Variable
ψ	-	Blade angle, °

Subscripts

0	-	Reference or ambient
a	-	Air
adj	-	Adjusted
b	-	Bundles
b	-	Buoyancy, support beam or bellmouth shroud
CV	-	Control volume
c	-	Casing or contraction
d	-	Design
dj	-	Downstream jetting loss
do	-	Downstream
E	-	Energy
ED	-	El Dorado
e	-	Effective
F	-	Fan
f	-	Face index
fg	-	Vaporisation
fr	-	Frontal
Gen	-	Generic
g	-	Gas
h	-	Hub
he	-	Heat exchanger
i	-	Inlet or numerical index
id	-	Ideal
j	-	Numerical index
k	-	Numerical index or turbulent kinetic energy
M	-	Momentum
m	-	Mean
o	-	Outlet

orig	-	Original
p	-	Constant pressure
r	-	Rows
ref	-	Reference
s	-	Static, shear or fan inlet screen
sc	-	Screen
st	-	Steam turbine
T	-	Temperature
t	-	Total or turbulent
tb	-	Tube bundles
ts	-	Tower supports
up	-	Upstream
v	-	Vapour or constant velocity
vp	-	Vapor passes
w	-	Wind or windwall
x	-	Direction
y	-	Direction
z	-	Direction
θ	-	Finned tube heat exchanger

1.   Introduction

1.1   Background and motivation

Air-cooled condensers (ACCs) use ambient air to cool and condense a process fluid. Mechanical draft ACCs are used extensively in the chemical and process industries and are finding increasing application in the global electric power producing industry due to economic and environmental considerations (Kröger, 2004).

The generation of electric power is traditionally a water intensive activity, and with the sustainability of fresh water resources becoming a major concern in many parts of the world, there is increasing pressure on this industry to find ways to reduce their fresh water consumption. Modern thermoelectric power plants with steam turbines are equipped with a cooling system to condense the turbine exhaust steam and maintain a certain turbine exhaust pressure (often referred to as turbine backpressure) in a closed cycle (Kröger, 2004), as illustrated in Figure 1.1 for a combined cycle gas/steam power plant. To date, most power plants employ a wet-cooling system which typically accounts for a vast majority of plant water consumption (DiFillipo, 2008). Alternative means of cooling therefore represent the greatest potential for water consumption reduction in thermoelectric power plants.
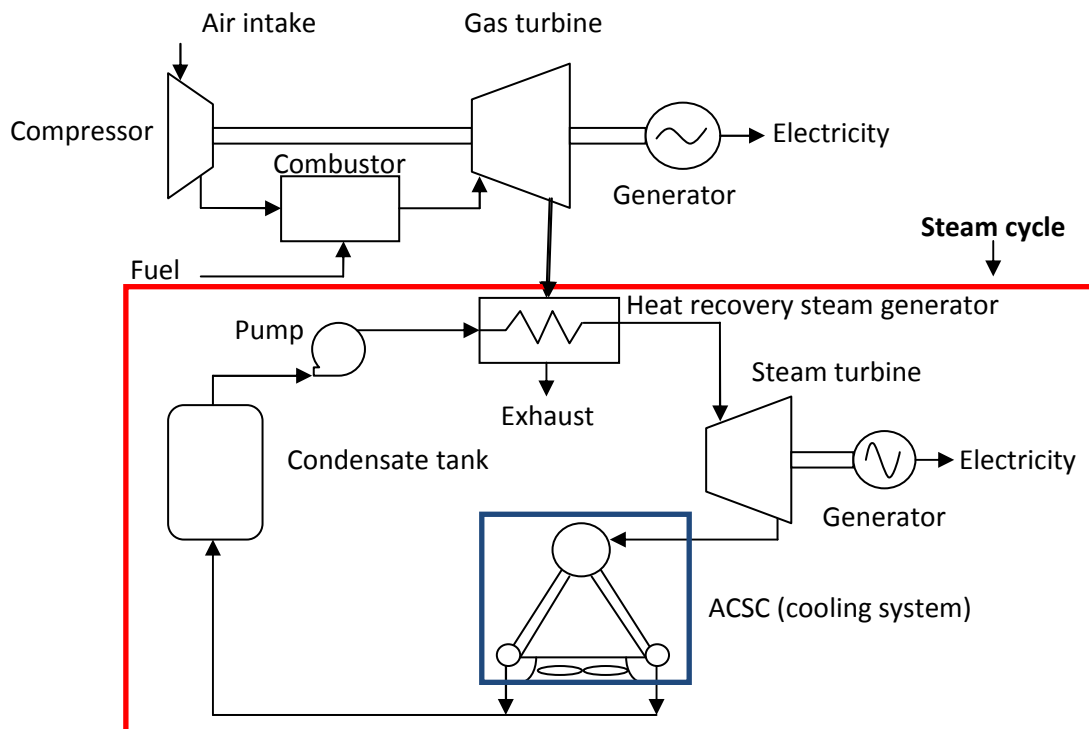
Figure 1.1:   **Combined cycle power plant schematic**

Mechanical draft air-cooled steam condensers (ACSCs) consisting of multiple fan units are used in direct cooled thermoelectric power plants to condense steam in a closed cycle using ambient air as the cooling medium (Kröger, 2004). No water is directly consumed in the cooling process and as such the total fresh water consumption of a power plant with an ACSC is significantly less than one employing wet-cooling. There are a number of advantages over and above water consumption reduction, such as increased plant site flexibility and shortened licensing periods, associated with the use of ACSCs.

In a direct cooled steam turbine cycle with an ACSC, low pressure steam is ducted from the turbine exhaust to steam headers that run along the apex of a number of ACSC fan units (also referred to as A-frame units or cells). A typical forced draft ACSC fan unit, shown in Figure 1.2, consists of an axial flow fan located below a finned tube heat exchanger bundle. The steam condenses inside the finned tubes as a result of heat transfer to ambient air forced through the heat exchanger by the fan. The finned tubes are typically arranged in an A-frame configuration for cooling applications of this magnitude so as to maximize the available heat transfer surface area while keeping the ACSC footprint to a minimum. The inclined tube configuration also aids in the effective drainage of the condensate which is ultimately pumped back to the boiler (Kröger, 2004), or heat recovery steam generator in the case of a combined-cycle plant, to complete the closed cycle.
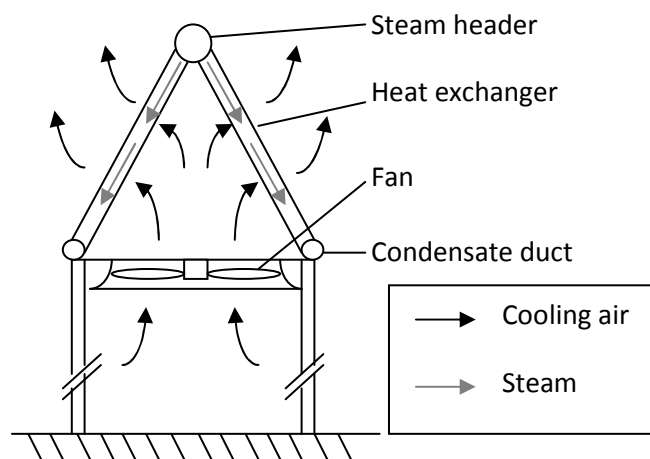
(a)

(b)

Figure 1.2: Mechanical draft ACSC fan unit, (a) Schematic, (b) During installation (courtesy Wurtz and Nagel, 2006)

The use of air as the cooling medium in an ACSC means that the heat transfer rate is influenced by ambient conditions such as wind, temperature and atmospheric instabilities. Under unfavourable operating conditions, for instance hot and/or windy periods, the performance of ACSCs has been found to decrease. Due to the dynamic relationship between the ACSC and the steam turbine, a decrease in ACSC heat transfer rate results in increased turbine backpressure and subsequently reduced turbine efficiency. The steam turbine output and/or plant fuel consumption is therefore affected by ACSC performance.

As the use of ACSCs becomes more widespread the importance of ensuring adequate and predictable cooling performance becomes critical to the efficient operation of the plant and ultimately the entire energy network (Maulbetsch and DiFilippo, 2007). An understanding of the flow in the vicinity of an ACSC can be applied in an attempt to optimize the performance of these systems. This study will use computational fluid dynamics (CFD) to investigate the effects of wind on ACSC performance characteristics.

1.2   Literature study

Securing sufficient supplies of fresh water for societal, industrial and agricultural uses, while protecting the natural environment, is becoming increasingly difficult (Barker, 2007). In the USA, thermoelectric power production accounts for approximately 40% of the total annual fresh water withdrawals and about 2% of the total fresh water consumption, corresponding to 27% of non-agricultural consumption (Carney, 2008). Approximately 48% of existing power plants make use of evaporative or wet cooling (Carney, 2008). These cooling systems loose approximately 2% of the cooling water they withdraw to evaporation and drift. Approximately a further 0.4% must be continuously discharged to prevent the build up of impurities. A 480 MW power plant that employs evaporative cooling would thus consume approximately 14.4 ML of fresh water on a daily basis (Gadhamshetty et al., 2006). It is therefore clear that power plants can have a major impact on local water availability.

With water sustainability being a major concern in most areas of the world where population pressures are mounting (Barker, 2007), increased concerns regarding the effects of climate variability on fresh water resources (Mills, 2008), and increasing demand for environmental protection and enhancement (Turnage, 2008), the electric power sector is under increasing pressure to reduce water consumption. Considering that in a wet cooled power plant the cooling system accounts for more than 80% of the total plant water consumption (DiFilippo, 2008), specific emphasis must be placed on cooling. This point is substantiated by the United States Environmental Protection Agency's fairly recent proposal that power plants that utilize more than 7.6 ML of fresh water a day, in other words any plant exceeding approximately 250 MW capacity, must consider alternative means of cooling (Gadhamshetty et al., 2006).

As mentioned previously, ACSCs use air as the cooling medium and so no water is required. Over and above the water conservation advantages of ACSCs, many other environmental drawbacks associated with wet cooling are eliminated. These drawbacks include plume formation, brine disposal and Legionella health risks (Gadhamshetty et al., 2006). ACSCs also hold potential economic and collateral advantages since power plant location will no longer be dependent on the location of abundant water supplies. Plants can therefore be located closer to load centres; resulting in reduced transmission losses, increased supply reliability, and increased security (Gadhamshetty et al., 2006). Recently ACSCs are being selected for use in projects where the "time-to-market" is an important consideration since

the use of dry-cooling can significantly reduce the power plant licensing process (EPRI, 2004).

Dry cooling systems such as ACSCs are, however, more capital intensive and typically exact a penalty in terms of plant performance and subsequently increase the cost of power generation (Barker, 2008). This is primarily due to the poor thermo-hydraulic properties of air as a cooling medium. Air's low density and specific heat mean that large volumes need to be circulated through the heat exchanger in order to achieve satisfactory cooling. Fan power consumption in ACSCs is therefore significant. Expensive finned tubes are also required to maximize heat transfer. Also, the allowable pressure drop across the ACSC is low if adequate circulation is to be achieved (Hassani et al., 2003). This means that the air flow velocity has to be kept low and subsequently large cross-sectional flow areas are required in order to achieve the required mass flow rate for adequate heat transfer. As a result of the above, the capital cost of an ACSC can be as much as three times that of a wet cooling system of equivalent capacity, while the annual running costs are typically double (at current water prices) (Maulbetsch, 2008). However, with escalating water prices and the potential transmission cost savings associated with dry cooling, the annual costs of the two cooling alternatives mentioned are expected to become increasingly comparable (Gadhamshetty et al., 2006).

Cost issues aside, a general reluctance exists in the power producing industry to accept ACSC technology. In the USA less than 1% of power plants are dry cooled (Carney, 2008). The primary reason for this reluctance is the reduced performance ACSCs experience during periods of high ambient temperatures and strong winds. ACSCs can experience losses in cooling effectiveness of up to 10% under the above mentioned conditions (Gadhamshetty et al., 2006), resulting in a measurable reduction in steam turbine efficiency.

A number of investigations have been undertaken to attempt to identify, quantify and reduce the effects of wind on ACSC performance. It has been found that the negative effects of wind are a result of both distorted fan inlet conditions and hot plume recirculation (Duvenhage and Kröger, 1996). Distorted inlet flow conditions (see Figure 1.3), identified experimentally by Van Aarde (1990), result in reduced flow rates through the fans and subsequently reduced ACSC heat transfer rates (Bredell, 2005). These distortions are predominant on the windward or leading edge fans in an ACSC, and can result in significant reductions in flow rates (50%

to 70%) in some of these fans (Maulbetsch, 2008; McGowan et al., 2008). With regard to plume recirculation, when hot plume air is drawn back into the ACSC the effective cooling air temperature is increased resulting in decreased heat transfer rates (Duvenhage and Kröger, 1996). This recirculation effect is most predominant at the downwind edges and corners of the ACSC. It has, however, been found that the magnitude of the hot air recirculation is small for most wind conditions at specific plants (Maulbetsch, 2008; McGowan et al., 2008; Liu et al., 2009).
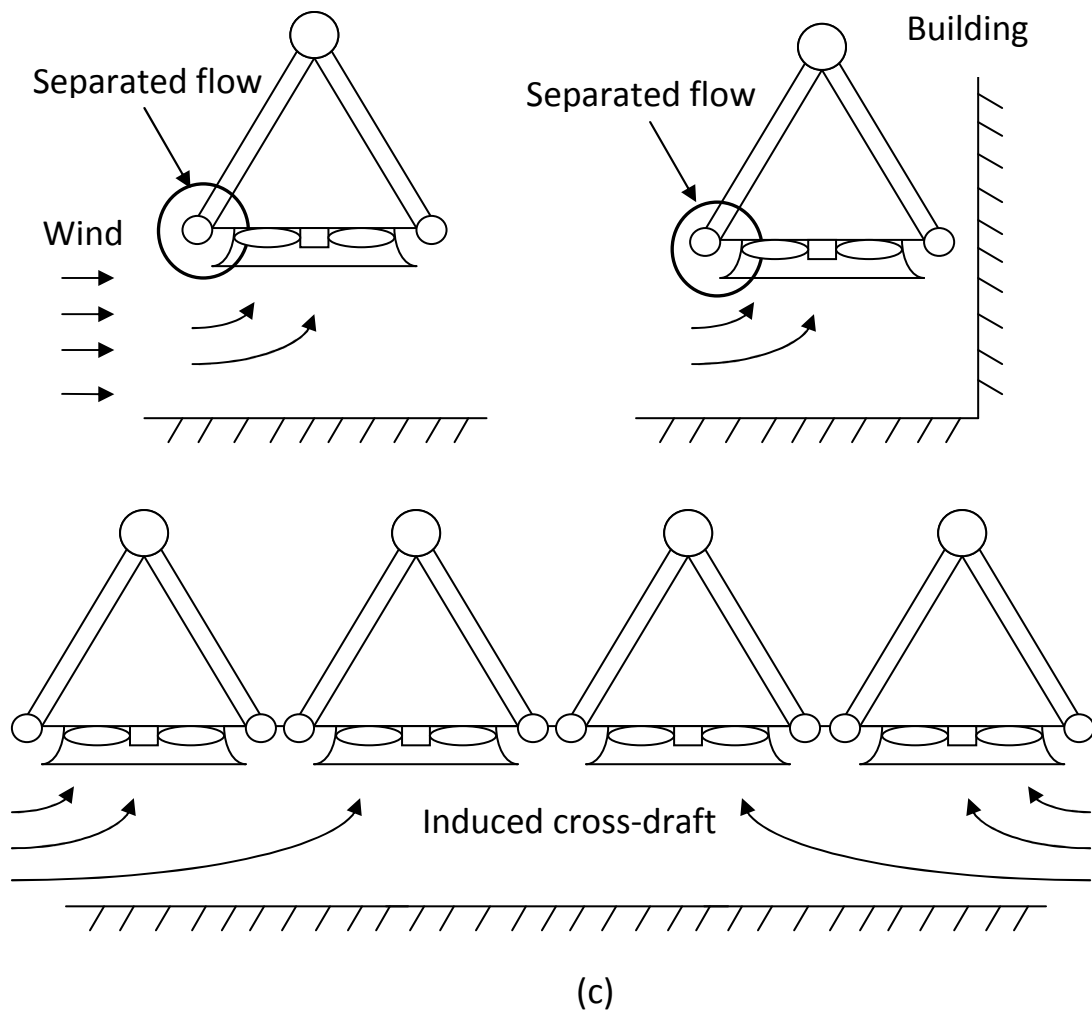
Figure 1.3: **Typical fan inlet flow distortions, caused by (a) wind effects, (b) the proximity of buildings, and (c) cross-draft induced by other fans**

Distorted fan inlet conditions occur during windless periods since flow can only enter at the edges of the fan platform and so the inner fans automatically induce a cross-flow component across the periphery fans (Stinnes and von Backström, 2002). This component may be

6

exacerbated by unfavourable wind conditions (Stinnes and von Backström, 2002) and result in off-axis inflow to the fans. The proximity of buildings or other structures can also contribute to these distorted inflow conditions (Thiart and von Backström, 1993). The flow rate through the fans is adversely affected by these distorted inflow conditions (Duvenhage and Kröger, 1996; Bredell et al., 2006) due to a reduction in the static pressure rise across each fan. This pressure rise reduction is caused by increased kinetic energy per unit volume at the fan exit, and greater dissipation through the fan itself (Hotchkiss et al., 2006).

Several approaches have been investigated in an attempt to minimize distorted inflow to fans in large ACSCs. It is well documented that fan performance can be improved by increasing the fan platform height above the ground (Salta and Kröger, 1995; Duvenhage and Kröger, 1996). This is primarily due to the fact that raising the fan platform results in an increase in the flow area under the fans and, subsequently, reduced cross-flow accelerations (Duvenhage and Kröger, 1996). An empirical relationship between fan volumetric effectiveness and fan platform height is derived by Salta and Kröger (1995). Furthermore, Salta and Kröger (1995) found through experimental methods that the addition of a solid walkway or skirt around the periphery of the ACSC at the fan platform height reduces the negative effects of wind on the performance of the periphery fans. This was later confirmed numerically by Bredell et al. (2006) and will be expanded on in subsequent chapters of this document. It has also been shown that the type of fan inlet shroud has a marked effect on fan performance under windy conditions (Duvenhage et al., 1996), but that the optimum shroud configuration is dependent on factors such as fan platform height amongst others (Meyer, 2005).

Computational Fluid Dynamics (CFD) has been identified as a useful tool to investigate large scale air-cooled heat exchangers that are characteristically difficult (Meyer, 2005) and prohibitively expensive (Meyer and Kröger, 2004) to investigate experimentally. This is in part due to the fact that CFD is an effective tool for generating detailed parametric studies that allow for the evaluation of far more design alternatives than build and test methods (Kelecy, 2000). CFD also provides more complete information than physical experimentation and thus provides more insight into reasons for designs performing in certain ways (Kelecy, 2000). CFD therefore provides extensive opportunities for rapid design optimization. It is, however, essential to validate CFD results with well documented test cases (Kelecy, 2000).

1.3 Problem statement and objectives

The effects of wind on ACSC performance will be investigated through CFD simulations of the flow about and through two ACSCs, illustrated in Figure 1.4. Both ACSCs consist of 30 fan units.
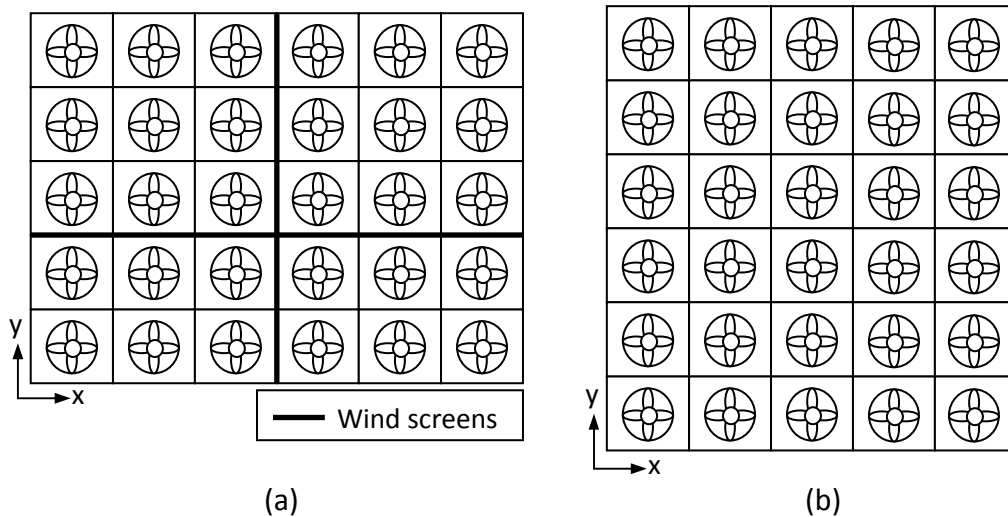
Figure 1.4: **ACSC fan unit configuration, (a) El Dorado, (b) Generic ACSC**

El Dorado power plant is a modern, high efficiency combined cycle plant located in the Mojave Desert in Nevada, USA. This study will focus primarily on the effects of wind on the performance of this specific ACSC (note that wind screens are installed under this ACSC in the locations indicated in Figure 1.4). The generic ACSC corresponds with that considered by Van Rooyen (2008). This ACSC provides a useful means of comparing the results generated in this study to previous numerical work, as well as providing a platform to investigate potential ACSC modifications that are not suited to El Dorado.

The objectives of this study are to generate an efficient and reliable method of modelling large ACSC installations, and to apply the resulting models in an effort to evaluate the performance of an ACSC under windy conditions. Furthermore, an attempt will be made to identify and evaluate strategies aimed at mitigating the negative effects of wind on ACSC heat transfer rates. The findings may increase the ability of El Dorado, and other power plants employing ACSCs, to ensure adequate and predictable cooling performance and subsequently maintain optimum steam turbine efficiencies and rated output.

2. System description

2.1 *System components*

A typical ACSC fan unit, is illustrated in Figure 2.1 (this particular unit is located at the ACSC periphery).
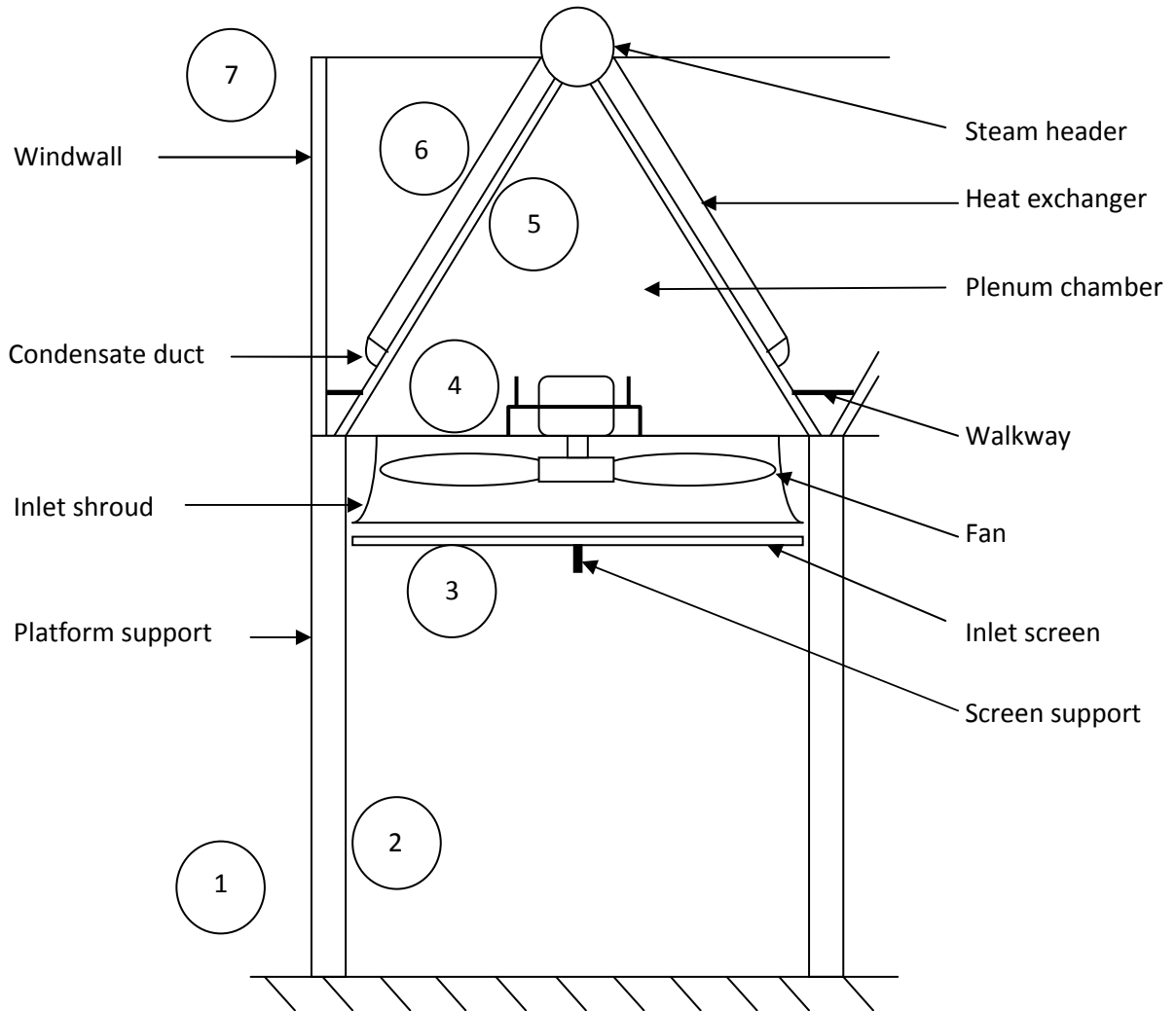
Figure 2.1:   **Schematic of a typical ACSC fan unit**

During operation, ambient air at (1) is accelerated towards the fan platform supports at (2) under the influence of the axial flow fan. The air flows through the fan inlet screen at (3) into the inlet shroud, through the fan, and into the plenum chamber at (4). Heat is transferred to the air as it is forced through the finned tube heat exchanger from (5) to (6) after which it is exhausted into the atmosphere at (7). Windwalls are installed along the periphery of the ACSC to reduce plume recirculation. The finned tube heat exchanger and axial flow fan are arguably the two most important components in the system and will be described in more detail hereafter.

2.1.1 Finned tube heat exchanger

Various finned tube heat exchanger configurations exist in practice. The ACSCs evaluated in this study make use of heat exchangers consisting of two rows of finned tubes. The tubes employed in the generic ACSC are flattened while those used at El Dorado are elliptically shaped, similar to the ones illustrated in Figure 2.2. The tubes are shaped in this way to reduce their resistance to flow while the rectangular plate fins serve to increase the air-side heat transfer area and in so doing increase the effective heat transfer coefficient through the heat exchanger. The flow and heat transfer characteristics of the finned tubes used in the ACSC heat exchangers considered in this study are described in Appendix A.1.

(a)   (b)
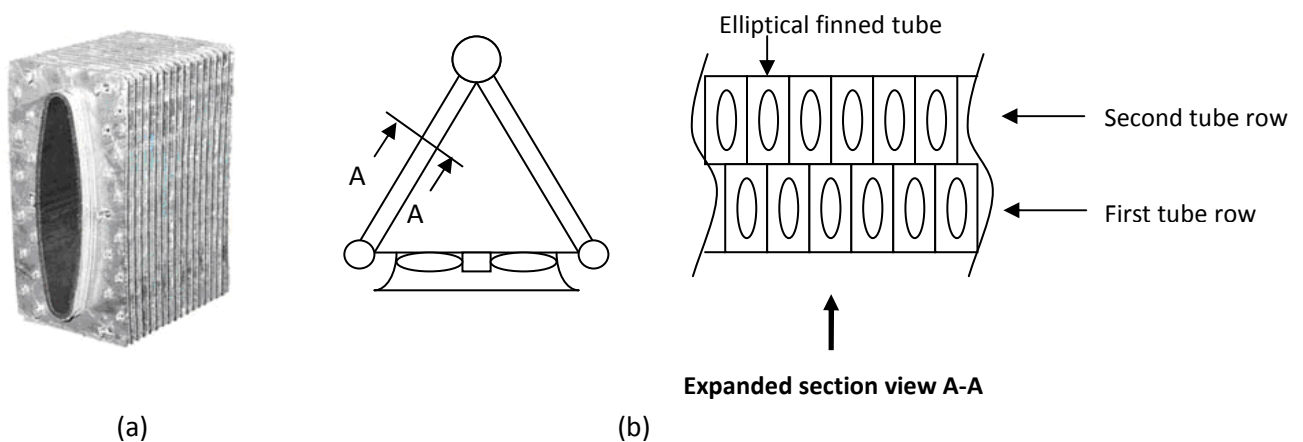
Figure 2.2:   **Finned tube heat exchanger (a) Typical elliptical finned tube, (b) Two tube row configuration**

The finned tubes are typically arranged in bundles consisting of a certain number of tubes, n_{tb1} and n_{tb2}, in the first and second tube rows respectively. The fin pitch is reduced in subsequent tube rows in an attempt to ensure a near uniform condensation rate in each row despite the increase in air temperature as it moves through the heat exchanger. The heat exchanger in each ACSC fan unit will consist of multiple tube bundles as illustrated in Figure 2.3. Details regarding the number of tube bundles, n_b, and the numbers of tubes per row in each bundle are included in Appendix A.1.
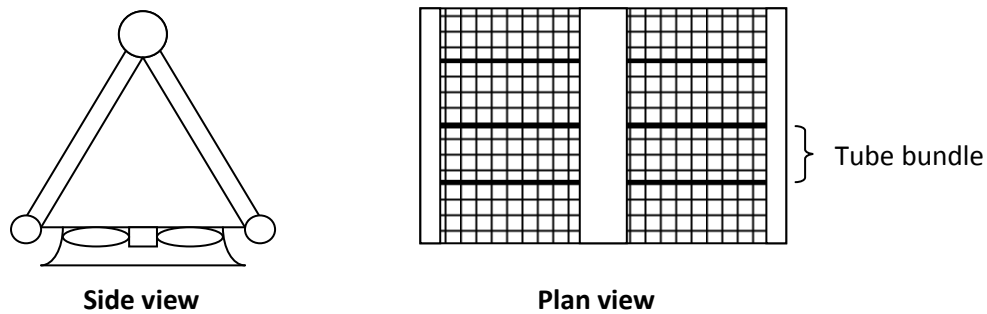
Figure 2.3: **Finned tube heat exchanger arrangement**

2.1.2 Axial flow fan

Axial flow fans typically provide high volume flow rates at relatively low pressure rise and are therefore ideally suited to dry cooling applications. A wide variety of fans are available for industrial applications. The selection of a fan is based primarily on its performance characteristics; however, factors such as cost, noise production and structural strength also play a role.

Fan characteristics are determined according to international test codes and standards. It is important to note, however, that the aforementioned tests are typically carried out on an isolated fan under axial inlet flow conditions in the absence of any significant flow distortions. Such conditions are hereafter referred to as ideal flow conditions. In actual fan installations, the proximity of buildings and other fans, as well as the presence of wind, may result in distorted, or off-axis, conditions at the fan inlet. It can therefore be expected that the performance of an operational full scale fan will differ somewhat from that predicted by the test data in conjunction with the fan laws. The degree to which fan performance in an actual installation conforms to the specified characteristics is primarily a function of the operating conditions and the ACSC geometry. The details of the fans used by the ACSCs considered in this investigation are included in Appendix A.2.

2.2 Thermal-flow analysis

The purpose of an ACSC is to reject a certain amount of heat to the atmosphere, and in so doing condense the required amount of steam, under prescribed operating conditions (Bredell, 2005). The heat transfer between the steam and the air in the heat exchanger is described by the energy equation. In order to facilitate the necessary heat transfer, air must

flow through the heat exchanger. This flow rate is a function of the relationship between the pressure rise induced by the fan and the losses associated with flow through the ACSC system. This relationship is described by the draft equation. In the thermal-flow analysis of an ACSC the draft and energy equations are inherently coupled and must be solved simultaneously. A description of the aforementioned equations, as given by Kröger (2004), follows.

2.2.1 Energy equation

The heat transfer between the condensing steam and the air flowing through the finned tube heat exchanger, consisting of n_r tube rows, in an ACSC is described by equation (2.1).

$$Q = \sum_{i=1}^{n_r} m_a c_{pa(i)} \left(T_{ao(i)} - T_{ai(i)} \right) = \sum_{i=1}^{n_r} m_a c_{pa(i)} e_{(i)} \left(T_v - T_{ai(i)} \right) \tag{2.1}$$

where $T_{ai(i)}$ and $T_{ao(i)}$ are respectively the air inlet and outlet temperatures for tube row i and T_v is the steam temperature. The heat transfer effectiveness of a finned tube bundle, $e_{(i)}$, is of the form shown in equation (2.2).

$$e_{(i)} = 1 - \exp\left(-UA_{(i)} / m_a c_{pa(i)} \right) \tag{2.2}$$

The overall heat transfer coefficient between the steam and the air, $UA_{(i)}$, is primarily dependent on the air-side heat transfer characteristics of the finned tube bundles due to the relatively low thermal resistance of the condensate film on the inside of the tubes, and is calculated as shown in equation (2.3)

$$UA_{(i)} = k_{a(i)} \Pr_{a(i)}^{0.333} n_b A_{fr(i)} Ny_{(i)} \tag{2.3}$$

where $A_{fr(i)}$ is the frontal area of a single tube bundle and $Ny_{(i)}$ is the characteristic heat transfer parameter of the tubes used in the bundle in question.

2.2.2 Draft equation

As air flows through the ACSC it experiences mechanical energy losses due to the presence of flow obstructions, such as screens, support beams, and the heat exchanger bundles. The pressure drop across a flow obstruction is described by means of a dimensionless loss coefficient as shown in equation (2.4).

$$K = \Delta p \Big/ \frac{1}{2}\rho v^2 \qquad (2.4)$$

where v is the characteristic flow velocity based on a prescribed area.

If the vertical pressure gradients in the stagnant ambient air are neglected then the draft equation for an ACSC fan unit, as illustrated in Figure 2.1, is as shown in equation (2.5).

$$
\begin{aligned}
p_{a1} - p_{a7} = {} & \frac{K_{ts}}{2\rho_{a56}}\left(\frac{m_a}{n_b A_{fr}}\right)^2 + \frac{K_{up}}{2\rho_{a3}}\left(\frac{m_a}{A_e}\right)^2 - \Delta p_{Fs} + \frac{K_{do}}{2\rho_{a3}}\left(\frac{m_a}{A_e}\right)^2 \\
& + \frac{K_{\theta t}}{2\rho_{a56}}\left(\frac{m_a}{n_b A_{fr}}\right)^2 \approx 0
\end{aligned}
\qquad (2.5)
$$

K_{ts}, K_{up} and K_{do} represent the losses due to the ACSC platform supports, and obstacles up and downstream of the fans respectively. $K_{\theta t}$ is the total loss coefficient over the heat exchanger and includes kinetic energy losses at the A-frame outlet (see Appendix D). Δp_{Fs} is the fan static pressure as described in Appendix A.2. A_e is the effective flow area through the fan as described in equation (2.6).

$$A_e = \pi\left(d_c^2 - d_h^2\right)\Big/4 \qquad (2.6)$$

where, d_c and d_h are the fan casing and hub diameters respectively.

3. Numerical modelling

3.1 CFD code overview

The commercially available CFD code, FLUENT, was used in this study. This section will discuss the governing equations, numerical methods and models, and boundary conditions applied in this study.

3.1.1 Governing equations

The governing equations of fluid flow represent mathematical statements of the conservation laws of mass, momentum and energy (Versteeg and Malalasekera, 2007). FLUENT numerically solves these equations using the finite volume method relevant to viscous incompressible fluids. The governing equations are presented in Table 3.1.

Table 3.1: Governing equations for steady flow of a viscous incompressible fluid

Continuity	$div(\rho\vec{v}) = 0$
x-momentum	$div(\rho u\vec{v}) = -\dfrac{\partial p}{\partial x} + div[(\mu + \mu_t)grad(u)] + S_{Mx}$
y-momentum	$div(\rho v\vec{v}) = -\dfrac{\partial p}{\partial y} + div[(\mu + \mu_t)grad(u)] + S_{My}$
z-momentum	$div(\rho w\vec{v}) = -\dfrac{\partial p}{\partial z} + div[(\mu + \mu_t)grad(u)] + S_{Mz}$
Energy	$div(\rho T\vec{v}) = -pdiv(\vec{v}) + div[kgrad(T)] + \Phi + S_E$

In Table 3.1 above $\vec{v}$ is the velocity vector as described in equation (3.1) while μ_t is the turbulent fluid viscosity and will be discussed later.

$$\vec{v} = u\vec{i} + v\vec{j} + w\vec{k} \tag{3.1}$$

where $\vec{i}$, $\vec{j}$ and $\vec{k}$ are unit vectors in the *x*, *y* and *z* directions respectively.

The momentum source terms S_{Mx}, S_{My} and S_{Mz} take into account viscous effects and make provision for the effects of external momentum sources or sinks such as gravity, buoyancy and flow obstructions. Φ is an energy dissipation term and is defined in equation (3.2).

$$\Phi = (\mu + \mu_t)\left\{\begin{array}{l}2\left[\left(\dfrac{\partial u}{\partial x}\right)^2 + \left(\dfrac{\partial v}{\partial y}\right)^2 + \left(\dfrac{\partial w}{\partial z}\right)^2\right] + \left(\dfrac{\partial u}{\partial y} + \dfrac{\partial v}{\partial x}\right)^2 + \left(\dfrac{\partial u}{\partial z} + \dfrac{\partial w}{\partial x}\right)^2 \\ + \left(\dfrac{\partial v}{\partial z} + \dfrac{\partial w}{\partial y}\right)^2\end{array}\right\} \tag{3.2}$$

Finally, the energy source term, S_E, makes provision for energy source or sink terms that may come about as a result of, amongst other phenomena, heat transfer to or from the fluid.

The governing equations are discretized, as described in Section 3.1.2 hereafter, and solved numerically using the SIMPLE solution algorithm for pressure-velocity coupling (Patankar, 1980).

3.1.2 Discretization

The governing equations are integrated over each control volume or cell in the numerical grid and then discretized. For convenience consider the generalized form of the steady state governing equations presented in equation (3.3).

$$div(\rho\varphi\vec{v}) = div\left[\Gamma_\varphi grad(\varphi)\right] + S_\varphi \tag{3.3}$$

In this equation, by setting the variable φ equal to 1, u, v, w or T and selecting appropriate values of the diffusion coefficient Γ_φ and source terms, the equations listed in Table 3.1 are obtained (Versteeg and Malalasekera, 2007).

Integrating equation (3.3) over a control volume yields,

$$\int_{CV} div(\rho\varphi\vec{v})dV = \int_{CV} div\left[\Gamma_\varphi grad(\varphi)\right]dV + \int_{CV} S_\varphi dV \tag{3.4}$$

where V represents the cell volume.

15

Using Gauss's divergence theorem it is possible to rewrite the first two terms in equation (3.4) as integrals over the bounding surfaces of the control volume as shown in equation (3.5).

$$\int_A \rho \varphi \vec{v} \bullet d\vec{A} = \int_A \Gamma_\varphi grad(\varphi) \bullet d\vec{A} + \int_{CV} S_\varphi dV \tag{3.5}$$

In equation (3.5) above $\vec{A}$ is the area vector of the control volume in question. Discretization of equation (3.5) yields,

$$\sum_{f=1}^{N_{faces}} \rho_f \varphi_f \vec{v}_f \bullet \vec{A}_f = \sum_{f=1}^{N_{faces}} \Gamma_\varphi grad(\varphi_f) \bullet \vec{A}_f + S_\varphi V \tag{3.6}$$

where the subscript f is a control volume face index. The variable φ_f therefore represents the value of φ at face f.

FLUENT stores discrete values of the flow parameters (represented by φ) at the control volume centres (Fluent Inc., 2006). Values for these parameters are required at the volume faces in order to solve equation (3.6). A first-order upwind scheme is used for this purpose. With this scheme the face value, φ_f, is set equal to the value of φ at the centre of the upstream volume.

The first-order upwind differencing scheme was selected for solution stability purposes. While numerical diffusion is a common disadvantage associated with the first-order upwind differencing scheme, it will always result in a physically realistic solution (Patankar, 1980). Higher order accuracy (based on the Taylor series truncation error) is achievable using the second-order upwind differencing scheme. However, this scheme is more unstable than the first-order scheme and requires a higher grid resolution to obtain convergence. Second-order differencing is therefore not suited to this investigation where large models are solved with fairly limited computational capacity.

3.1.3 Turbulence model

Turbulence is accounted for using the realizable k-ε turbulence model (Shih et al., 1995). This model is an improvement on the standard k-ε model (Launder and Spalding, 1974), used by Bredell (2005) and Van Rooyen (2008), and provides superior performance for flows involving separation, recirculation, rotation and boundary layers under strong adverse pressure gradients (Fluent Inc., 2006). The steady state governing equations for the turbulent kinetic energy, k, and the turbulent energy dissipation rate, ε, in a viscous incompressible fluid are presented in equations (3.7) and (3.8) respectively.

$$div(\rho k \bar{v}) = div\left[\left(\mu + \frac{\mu_t}{\sigma_k}\right)grad(k)\right] + G_k + G_b - \rho\varepsilon + S_k \tag{3.7}$$

$$div(\rho \varepsilon \bar{v}) = div\left[\left(\mu + \frac{\mu_t}{\sigma_\varepsilon}\right)grad(\varepsilon)\right] + \rho C_1 S\varepsilon - \rho C_2 \frac{\varepsilon^2}{k + \sqrt{\nu\varepsilon}} + C_{1\varepsilon}\frac{\varepsilon}{k}G_b + S_\varepsilon \tag{3.8}$$

In equations (3.7) and (3.8), G_k and G_b represent the generation of turbulent kinetic energy due to mean velocity gradients and buoyancy respectively (Fluent Inc., 2006), while S_k and S_ε respectively make provision for additional sources of turbulent kinetic energy or dissipation rate. The turbulent Prandtl numbers for turbulent kinetic energy and turbulent energy dissipation rate are represented by σ$_k$ and σ$_\varepsilon$ respectively (see Table 3.2). Furthermore,

$$C_1 = max\left[0.43, \eta/(\eta + 5)\right] \tag{3.9}$$

where,

$$\eta = S \cdot k/\varepsilon \tag{3.10}$$

and S is the modulus of the mean strain rate tensor as described in Shih et al. (1995).

The turbulent viscosity, which appears in Table 3.1 and equations (3.7) and (3.8), is defined as shown in equation (3.11).

$$\mu_t = \rho C_\mu k^2/\varepsilon \tag{3.11}$$

17

One of the primary differences between the standard and realizable k-ɛ turbulence models is that in the standard model C_μ is a constant while in the realizable model it is a function of the mean strain and rotation rates, as well as k and ε (Fluent Inc., 2006), as shown in equation (3.12) below.

$$C_\mu = \left(B_0 + B_s \frac{kU^*}{\varepsilon} \right)^{-1}$$

(3.12)

In equation (3.12), B_s is a function of the shear tensor and U^* is a function of both the shear tensor and the rate of rotation of the fluid as described in detail in Shih et al. (1995).

The values of the realizable k-ε turbulence model constants are given in Table 3.2 below.

Table 3.2: Realizable k-ɛ turbulence model constants

$C_{1\varepsilon}$	C_2	σ_k	σ_ε	B_0
1.44	1.90	1.00	1.20	4.04

3.1.4 Buoyancy effects

The effects of buoyancy due to air density gradients, caused by temperature variations in the flow domain, are taken into account using the Boussinesq model. This model treats density as a constant value in all the governing equations, except for the buoyancy term in the momentum equations (see Table 3.1) where the Boussinesq approximation shown in equation (3.13) is used.

$$\rho \approx \rho_0 (1 - \beta \Delta T)$$

(3.13)

In equation (3.13) ρ_0 is the air density at the ambient temperature, and ΔT represents the difference between the localized and ambient air temperatures. The thermal expansion coefficient, β, is approximated as a function of the ambient air temperature as illustrated in equation (3.14).

$$\beta = 1/T_a \qquad\qquad (3.14)$$

FLUENT also makes provision for the definition of fluid density as a function of temperature. Use of the Boussinesq model, however, results in more rapid convergence of the numerical solution than is possible for the previously mentioned case. Furthermore, density fluctuations as a result of temperature differences are small on average and have a negligible effect on the governing equations except in the buoyancy terms. Therefore, while the Boussinesq model results in an additional approximation in the numerical solution, the convergence rate advantage outweighs this drawback.

3.1.5 Boundary and continuum conditions

The solution of the governing equations requires specified boundary conditions. The appropriate selection and positioning of these numerical boundaries is of paramount importance to the accuracy of the results. The boundary conditions used in this study are discussed hereafter.

a) **Velocity boundary:** The velocity boundary condition allows the user to specify the inlet velocity vector on a flow domain boundary. Specification of the temperature and turbulence parameters is also required. The static pressure varies as required to meet the specified flow velocity. While this boundary condition is typically used as a flow domain inlet boundary, it is also possible to use it as an outlet boundary as long as overall continuity is maintained in the flow domain (Fluent Inc., 2006).

b) **Pressure boundary:** This boundary condition allows the user to specify the static pressure at a flow domain boundary where the flow rate and velocity profile across the boundary are unknown. Pressure boundaries allow flow to enter or leave the flow domain depending on the conditions adjacent to the boundary. When outflow takes place, the temperature and turbulence parameters at the boundary are extrapolated from the upstream cells. Inflow from a pressure boundary is always normal to the boundary and is subject to user specified temperature and turbulence parameters.

c) **Wall boundary:** This boundary condition is used to model all solid surfaces in the flow domain. As a default the no-slip condition is applied in FLUENT at the wall surface. FLUENT does, however, allow the user to specify a surface shear stress. A slip wall boundary condition can be achieved by setting the wall shear stress equal to zero.

d) **Pressure jump fan:** FLUENT's pressure jump fan model applies a discontinuous static-to-static pressure rise across an infinitely thin face. The pressure rise is determined as a function of the normal component of the flow velocity immediately upstream of the fan face. The pressure jump fan method will be described in greater detail in Section 3.2.2.1.

e) **Radiator:** The radiator boundary condition allows for the specification of a loss coefficient, of the form described in equation (2.4), and/or heat transfer coefficient based on the normal component of the flow through an infinitely thin radiator element.

f) **Interior face:** An interior face has no effect on the flow but provides a defined surface on which flow parameters can be monitored and/or recorded for later use.

g) **Porous zone:** A porous zone is a bounded cell zone within the flow domain in which an empirically determined momentum sink term is added to the governing momentum equations (Fluent Inc., 2006). The momentum sink term is defined by means of viscous and inertial loss coefficients (described in Section 3.2.2.2). Provision is also made for the addition of source or sink terms in the energy equation of the flow as it passes through the zone.

3.2   Numerical ACSC model

Due to computational limitations the numerical modelling of the ACSC was carried out in two stages. The first stage involves the solution of the flow field in the vicinity of a simplified representation of the ACSC. This stage is referred to as the global flow field stage. In the second stage, the ACSC is modelled in detail in a smaller flow domain with boundary conditions derived from the global flow field simulation results. The global flow field and detailed models are described in detail in the sections that follow.

An iterative solution procedure was followed during the numerical ACSC performance evaluation. First the global flow field was solved assuming all the fans are operating at the design point and the air temperature at the heat exchanger outlet is equal to the steam temperature. The necessary profiles were then extracted from the global flow field and applied to the boundaries of the detailed model. The predicted fan performances and average heat exchanger outlet temperature generated during the detailed model simulation were then used to update the ACSC behaviour in the global flow field model. The global flow field was subsequently solved again and updated profiles extracted for use in the final detailed model simulation. The sensitivity of the solution to the number of iterations was investigated and it was found that a single iteration was sufficient (see Section 4.1.2).

Numerical investigations of ACSCs of similar size to those considered in this study can be carried out using a single numerical model. The use of a single model simplifies and accelerates the solution process. However, for much larger installations consisting of many more fans a single model is not feasible. This investigation therefore serves as a useful means of evaluating the two-step solution procedure.

3.2.1 Global flow field

A schematic of the global flow field model is presented in Figure 3.1.

<div style="text-align:center">(a)   (b)</div>
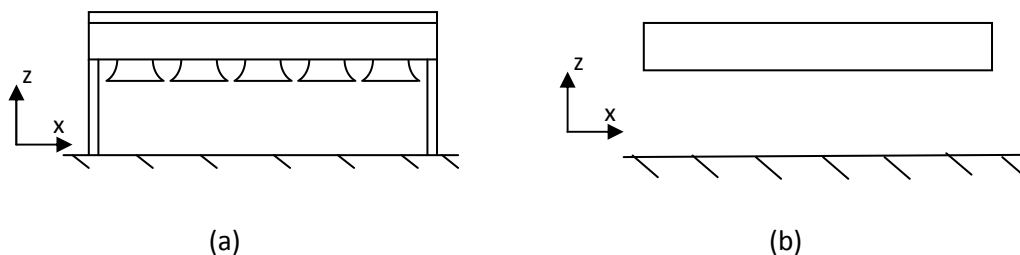
Figure 3.1:   Schematic of an ACSC, (a) Side elevation, (b) Side elevation (simplified for global flow field model)

In this model the ACSC is represented by a rectangle with uniform flow velocities specified across its inlet and outlet. The magnitudes of these velocities depend on the expected performance of the ACSC fans and the average density of the air at the ACSC inlet and outlet

respectively. The default turbulent kinetic energy and turbulent energy dissipation rate values of $k = 1\ m^2/s^2$ and $\varepsilon = 1\ m^2/s^3$ provided by FLUENT were applied at these boundaries.

The global flow field model is illustrated in Figure 3.2.
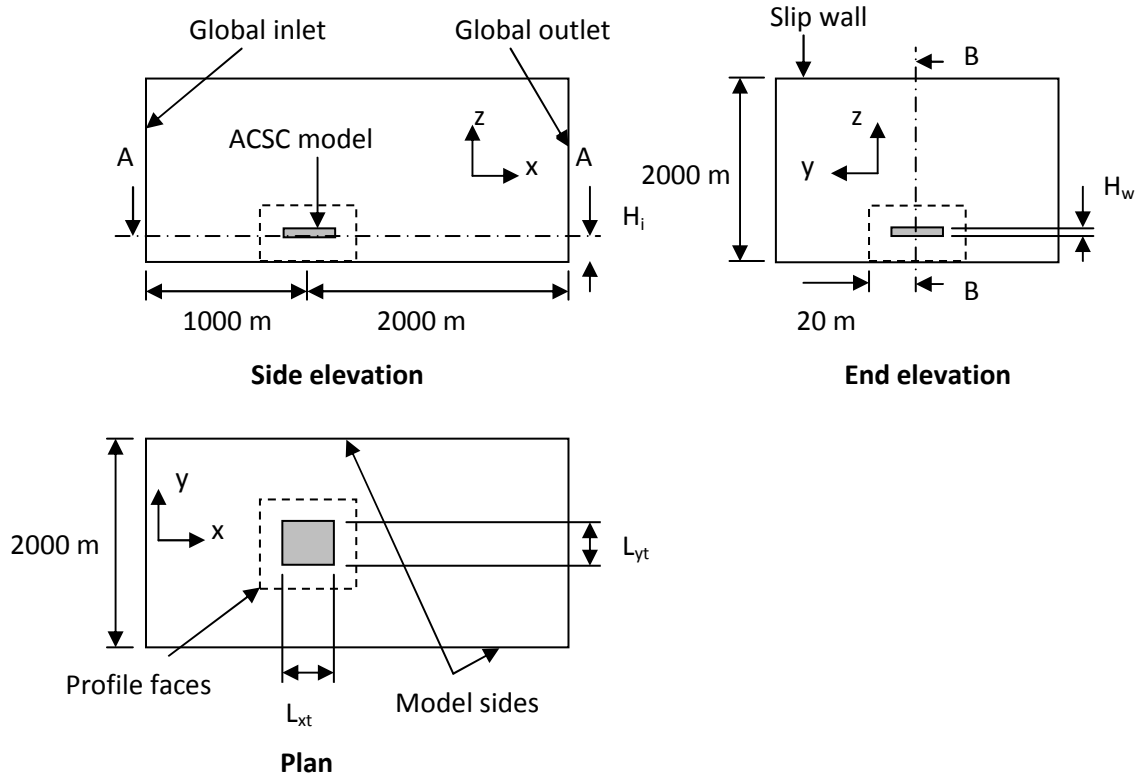
Figure 3.2:   Global flow field model

The flow domain sides are modelled using slip walls for straight-flow simulations and velocity inlet/pressure boundary conditions for cross-flow simulations. In this case straight-flow refers to a positive x-direction wind, while cross-flow describes a xy-direction wind (45° with respect to the x-direction). The flow domain roof is modelled using a slip wall for solution stability purposes. The side and roof boundaries are located sufficiently far from the ACSC and have a negligible influence on the flow in the region of interest. The ground is represented by a no slip wall. The dimensions of the El Dorado and generic global flow field models are included in Table 3.3.

Table 3.3: ACSC dimensions

	H_i, m	H_w, m	L_{xt}, m	L_{yt}, m
El Dorado	19.20	8.27	82.83	74.94
Generic system	20.00	10.00	59.00	63.36

A power law wind profile of the form shown in equation (3.15) is specified for the velocity inlet boundary used to represent the global inlet.

$$v_z = v_w \left(z / H_i \right)^b \tag{3.15}$$

In equation (3.15) above, vw is the wind velocity at fan platform height H_i, while b is a constant. Where experimental data is absent, $b = 1/7$ as used by Bredell (2005) and Van Rooyen (2008).

The global outlet boundary is modelled using the pressure boundary condition with a specified backpressure of 0 *N/m²* (gauge). Once again, the default turbulence parameters were applied at these boundaries.

Interior faces were placed at a distance of 20 m from the ACSC in all directions. Profiles of x-, y- and z-velocity, temperature, turbulent kinetic energy and turbulent energy dissipation rate were extracted from the global flow field model on these faces.

The computational grid makes use of a structured mesh in the vicinity of the ACSC while an unstructured mesh was used far from the region of interest. The unstructured mesh enabled sufficient grid resolution to be maintained in critical regions of the global flow field model while staying within the computational limitations by coarsening the grid in non-critical regions. The global flow field computational grid is illustrated in Figure 3.3.

(a)   **(b)**
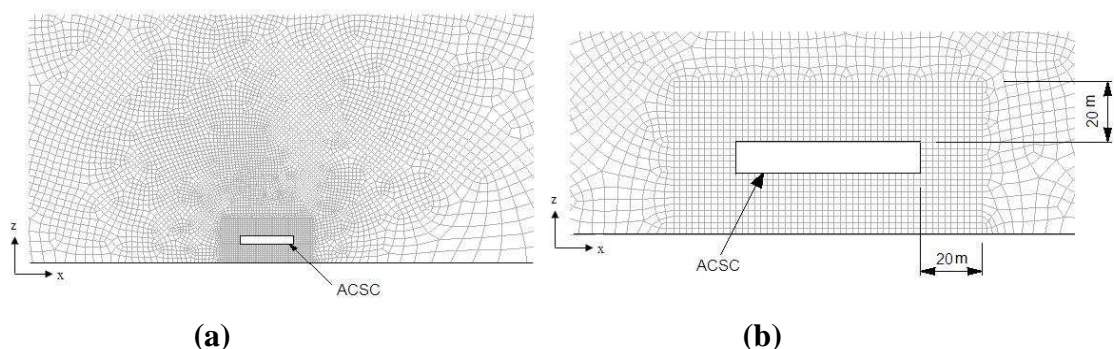
Figure 3.3:   **Section view (B-B) of the global flow field computational grid (a) Expanded view illustrating mesh expansion in non-critical areas, (b) Close-up view of the mesh in the region of interest**

23

3.2.2 Detailed ACSC model

A schematic of the detailed ACSC model is shown in Figure 3.4 below (dimensions are as given in Table 3.3). In this model the ground is represented using the no slip wall boundary condition. The flow domain boundaries are represented using the velocity boundary condition and profiles of x-, y- and z-velocity, temperature, turbulent kinetic energy and turbulent energy dissipation rate, extracted from the global flow field model, are applied to these boundaries. The ACSC consists of multiple fan units arranged in an array, as described in Section 1.3. The modelling of each fan unit and its components is described hereafter.
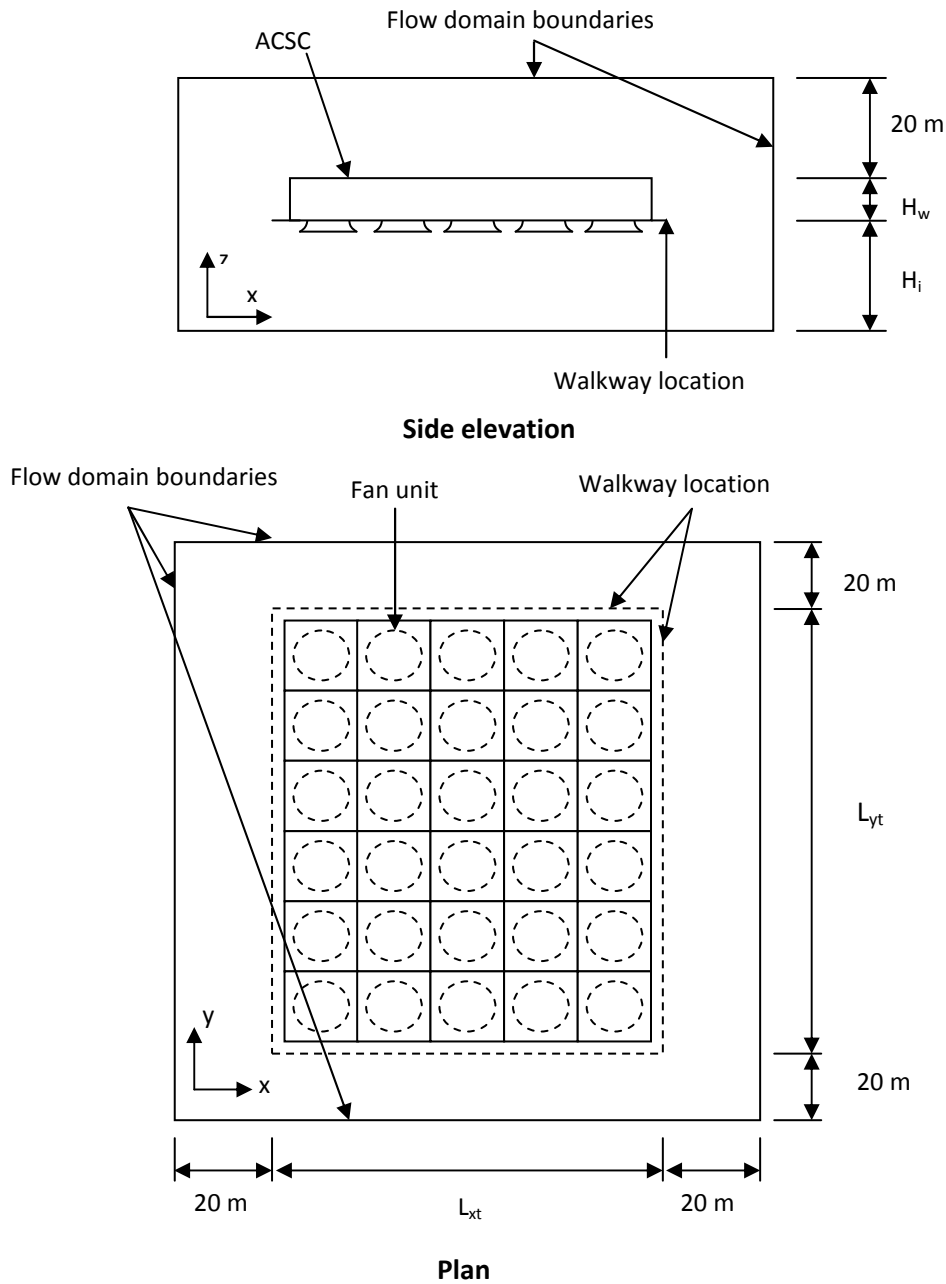
Figure 3.4: **Detailed ACSC model schematic**

Each ACSC fan unit (see Figure 2.1) consists of a fan inlet shroud, a fan, a plenum chamber and a heat exchanger; and is modelled as illustrated in Figure 3.5 below.
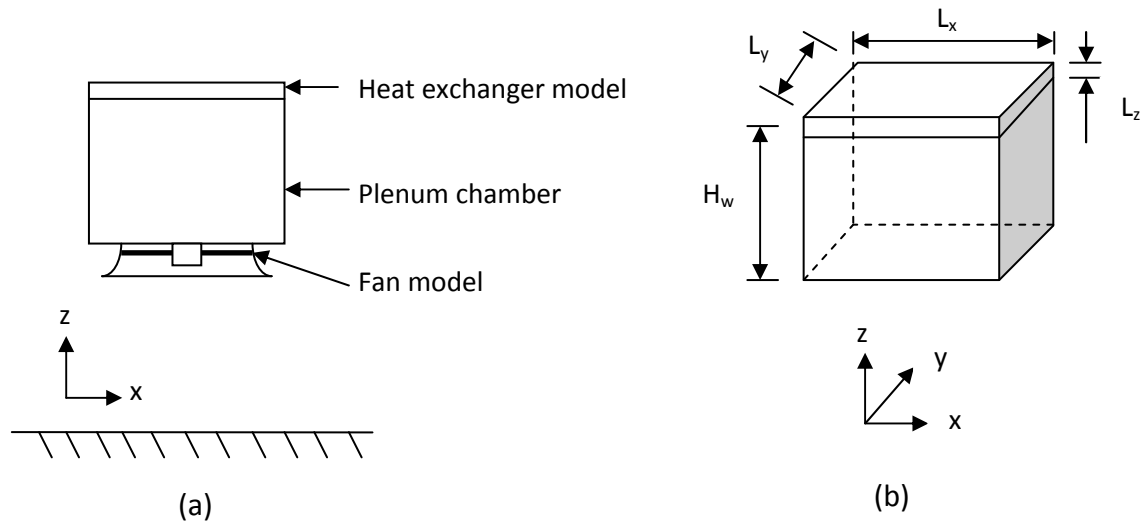
Figure 3.5:   ACSC fan unit, (a) Numerical model, (b) Numerical model dimensions

Table 3.4 gives the dimensions of the fan unit models for El Dorado and the generic ACSC. The fan and heat exchanger models are described in Sections 3.2.2.1 and 3.2.2.2 respectively. The computational grid in the vicinity of each fan unit is illustrated in Figure 3.6.

Table 3.4: ACSC fan unit numerical model dimensions

	L_x, m	L_y, m	L_z, m
El Dorado	13.805	14.988	0.2
Generic system	11.8	10.56	0.2
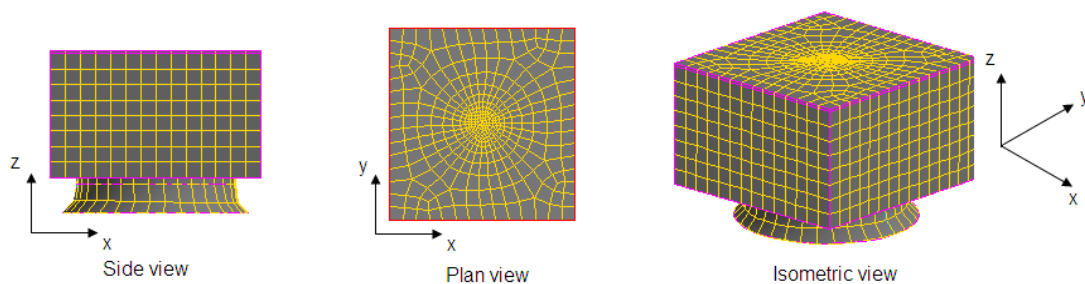
Figure 3.6:   Computational grid in the region of each ACSC fan unit

The effect of modelling the actual A-frame heat exchanger as opposed to using the simplified version (see Figure 3.7) was investigated and was found to have a negligible effect on the

numerically predicted ACSC fan performances. Furthermore, the modelling of the A-frame did not significantly affect the nature of the flow in the vicinity of the ACSC. A comparison of the results generated using the different heat exchanger models is included in Appendix B.1. The use of the simplified ACSC fan unit model is therefore reasonable since the purpose of this study is to investigate fan and ACSC performance and not the flow in the plenum or at the heat exchanger outlet (Van Rooyen, 2008).
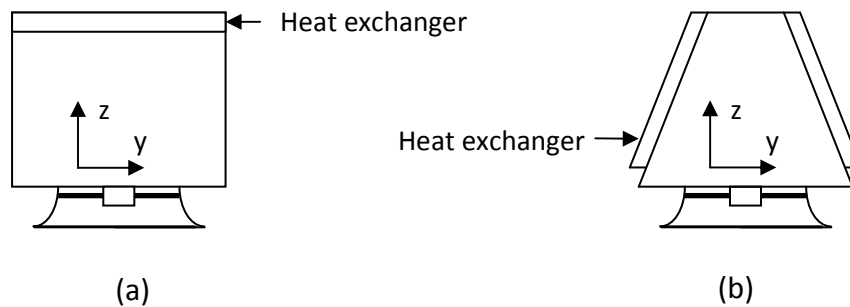
Figure 3.7: **ACSC fan unit models, (a) Simplified version, (b) A-frame version**

3.2.2.1 Numerical fan model

The pressure jump method (default FLUENT model) was used to represent the fans in the detailed ACSC model. As mentioned previously, the pressure jump across the fan is defined as a static-to-static pressure jump. The pressure jump method calculates the static pressure jump to be added to the static pressure term in the linear momentum equation in the flow field immediately upstream of the fan (Van der Spuy et al., 2009) based on a user-defined fan performance characteristic. This characteristic is sourced from the fan specifications. It must, however, be noted that the fan static pressure rise, as referred to by suppliers, is actually a total-to-static pressure rise since performance tests are carried out with a settling chamber immediately upstream of the fan. It is therefore necessary to add the dynamic pressure at the fan inlet to the specified fan static pressure characteristic, as described in Appendix C, in order to ensure realistic performance of the pressure jump fan model.

Due to the lack of information regarding the fan behaviour at very low flow rates or during backflow, it was assumed that the static-to-static pressure rise across the fan remains constant under these conditions. This assumption is reasonable since only small segments of a few fans operate under backflow conditions in the simulations carried out in this study. The

performance characteristics of the fans used in ACSCs considered in this study are illustrated in Figure 3.8 below (the units have been removed from El Dorado's fan performance characteristic for confidentiality purposes).

(a)

(b)
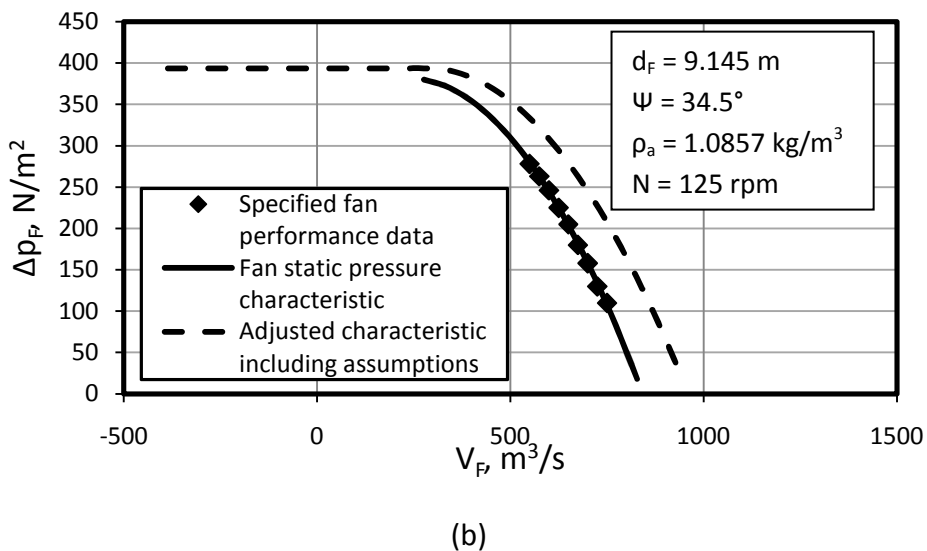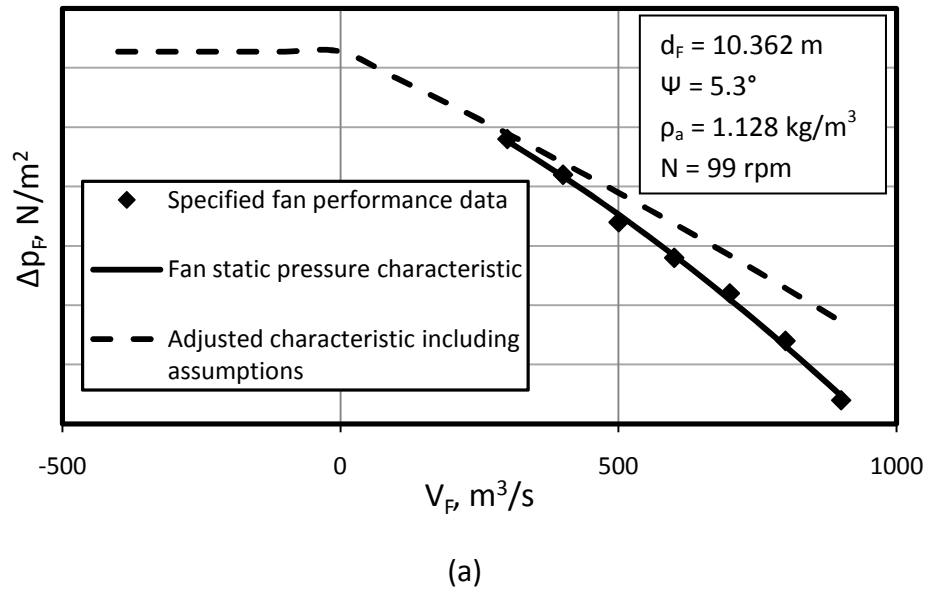
Figure 3.8: **Fan performance characteristics (a) El Dorado, (b) Generic system**

3.2.2.2 Heat exchanger model

The heat exchanger is modelled using FLUENT's porous zone continuum condition which accounts for losses in the mechanical energy of the air due to the effective system resistance to the flow, as well as heat transfer to the air.

The effective system resistance, as presented in equation (3.16), is modelled as a momentum sink term in the momentum conservation equations corresponding to the flow direction (Bredell, 2005).

$$\Delta p_e = -\left[\frac{K_{ts}}{2\rho_{a1}} \left(\frac{m_a}{n_b A_{fr}} \right)^2 + \frac{K_{up}}{2\rho_{a3}} \left(\frac{m_a}{A_e} \right)^2 + \frac{K_{do}}{2\rho_{a3}} \left(\frac{m_a}{A_e} \right)^2 + \frac{K_{\theta t}}{2\rho_{a56}} \left(\frac{m_a}{n_b A_{fr}} \right)^2 \right] \tag{3.16}$$

The loss coefficients listed in equation (3.16) are defined and evaluated in Appendix D. FLUENT's porous zone continuum condition allows these momentum sink terms to be specified as a function of the flow velocity, as illustrated in Table 3.5.

Table 3.5: Momentum sink terms for the heat exchanger model

Direction	Momentum sink, N/m^3
x	$-\left(C_x \dfrac{\rho\|\vec{v}\|u}{2} + \dfrac{\mu}{\alpha_x} u \right)$
y	$-\left(C_y \dfrac{\rho\|\vec{v}\|v}{2} + \dfrac{\mu}{\alpha_y} v \right)$
z	$-\left(C_z \dfrac{\rho\|\vec{v}\|w}{2} + \dfrac{\mu}{\alpha_z} w \right)$

The momentum sink terms consist of a viscous and an inertial resistance term. It follows therefore that $1/\alpha_i$ and C_i are respectively the viscous and inertial loss coefficients. The values of these coefficients were determined as shown in Appendix E and are shown in Table 3.6. The inertial loss coefficients in the x- and y-directions were chosen to be 10^3 times larger than in the z-direction in an attempt to model the straightening effect of the heat exchanger on the flow. The viscous loss coefficients in the x- and y-directions were set equal to zero.

Table 3.6: Heat exchanger loss coefficients

	$1/\alpha_z$, m^{-2}	C_z, m^{-1}
El Dorado	2.272 x 10^6	113.9784
Generic system	1.897 x 10^6	59.1364

An energy source term of the form shown in equation 3.17 is added to the energy conservation equation to account for heat transfer to the air as it passes through the heat exchanger. The derivation of this source term and its application in the numerical model are illustrated in Appendix F.

$$S_E = \rho_a |w| c_{pa} (T_{ao} - T_{ai}) / L_z \tag{3.17}$$

3.2.3 Ideal flow model

In order to determine the effects of wind on fan performance in an ACSC it is first necessary to determine the performance of the fan when operating under ideal flow conditions. A schematic of the numerical model used for this purpose is shown in Figure 3.9. The fan unit model is as described in Section 3.2.2.
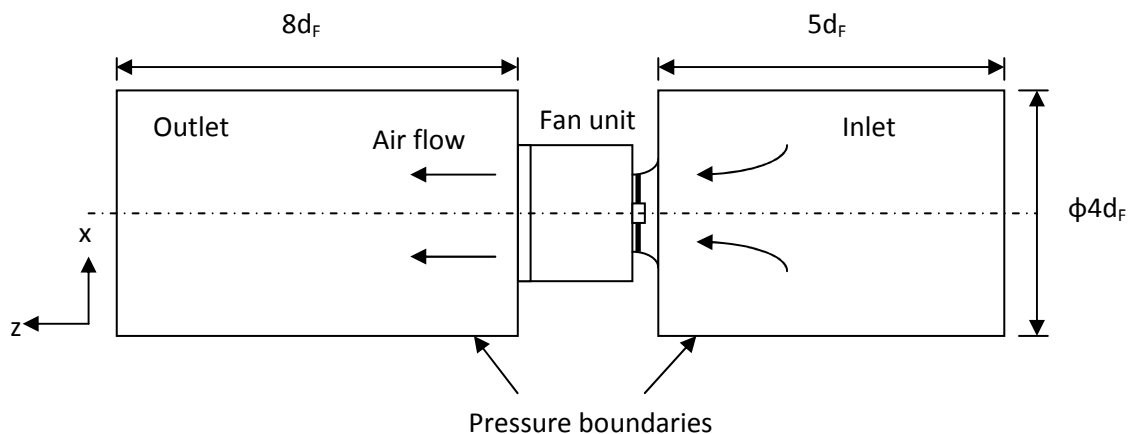
Figure 3.9:   Ideal flow model schematic

The numerical grid employed in the ideal flow model is illustrated in Figure 3.10 below. The meshing of the fan unit is as illustrated in Figure 3.6.
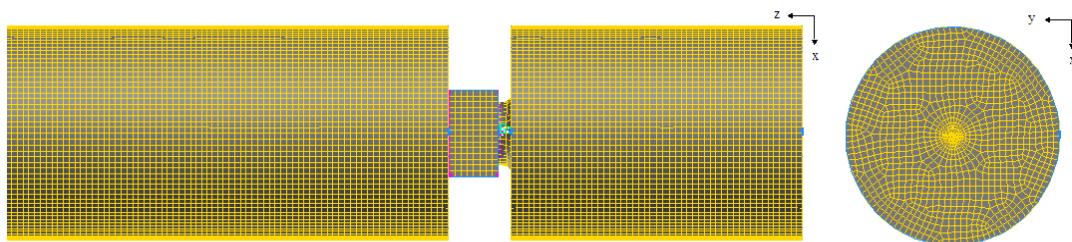
Figure 3.10:   Ideal flow model computational mesh

This model allowed the numerically determined operating point under ideal flow conditions to be compared to the theoretically calculated operating point to ensure that no significant errors had been introduced into the system through some of the assumptions and numerical simplifications made. A comparison of the two is illustrated in Appendix B.2.

3.3 Performance measures

In order to evaluate the performance of an ACSC and its components it is necessary to identify performance measures that provide meaningful information. In this study three performance measures were identified and utilized.

a) **Fan volumetric effectiveness** describes the performance of individual ACSC fans by comparing the volumetric flow rate through the fan under the prescribed operating conditions to the volumetric flow rate through the fan under ideal conditions.

$$Volumetric\ effectiveness = V_F / V_{F(id)} \tag{3.18}$$

Fan volumetric effectiveness is a useful means of identifying where fan inlet distortions are most severe.

b) **Heat transfer effectiveness** describes the performance of individual ACSC fan units by comparing the heat transfer rate achieved by the fan unit under the prescribed operating conditions to the heat transfer rate expected under ideal operating conditions. The heat transfer rate associated with a fan unit is given by,

$$Q = e m_a c_{pa} \left(T_v - T_{ai} \right) \tag{3.19}$$

where e is the heat transfer effectiveness of the finned tube heat exchanger as described in Section 2.2.1. The thermal effectiveness is defined as,

$$Heat\ transfer\ effectiveness = Q / Q_{id} \tag{3.20}$$

30

This measure can also be applied to an ACSC consisting of n_F fan units to determine the overall thermal effectiveness.

$$\text{Overall heat transfer effectiveness} = \sum_{j=1}^{n_F} Q_j \bigg/ n_F Q_{id} \qquad (3.21)$$

Heat transfer effectiveness takes into account the combined effects of reduced fan performance due to inlet distortions and plume recirculation, and is therefore a useful indicator of the effects of wind on ACSC performance.

c) **Steam turbine backpressure** is used as the final performance measure in this study. It has been mentioned previously that a dynamic relationship exists between the ACSC and the steam turbine, and that reduced ACSC performance results in increased turbine backpressure. Turbine backpressure is also monitored continuously at the power plant. It follows that steam turbine backpressure is a useful indicator of overall ACSC performance.

In order to calculate the steam turbine backpressure it is assumed that the heat rejected by the ACSC is constant for a given operating point regardless of wind conditions. This is untrue since the steam turbine efficiency is related to backpressure. The turbine efficiency therefore fluctuates with ACSC performance. For the same heat input, the heat to be rejected by the ACSC must therefore fluctuate along with the turbine backpressure. As a first approximation, however, it is useful to make the assumption that the heat rejected by the ACSC is constant.

The heat rejected by the ACSC under prescribed operating conditions is calculated as the sum of the heat rejected by each of the ACSC fan units.

$$Q = \sum_{j=1}^{n_F} m_{aj} c_{pa} e_j \left(T_{v(actual)} - T_{aij} \right) \qquad (3.22)$$

The heat transfer rate for the entire ACSC under ideal conditions can be calculated as shown in equation (3.23)

$$Q_{id} = n_F m_{a(id)} c_{pa} e_{id} (T_{v(id)} - T_a) \qquad (3.23)$$

Rearranging equation (3.22) and equating it to equation (3.23) yields the following expression used to calculate the actual steam turbine exhaust temperature under prescribed operating conditions,

$$T_{v(actual)} = \frac{Q_{id} + \sum_{i=1}^{6} \sum_{j=1}^{5} m_{aij} c_{pa} e_{ij} T_{aij}}{\sum_{i=1}^{6} \sum_{j=1}^{5} m_{aij} c_{pa} e_{ij}}$$

(3.24)

This actual steam turbine exhaust temperature can then be used to determine the steam turbine backpressure using equations (3.25) and (3.26), as given by Kröger (2004).

$$p_v = 10^z , \text{N/m}^2$$

(3.25)

where,

$$z = 10.79586\left(1 - 273.16/T_{v(actual)}\right) + 5.02808 \log_{10}\left(273.16/T_{v(actual)}\right)$$
$$+ 1.50474 \times 10^{-4} \left[1 - 10^{-8.29692\left(T_{v(actual)}/273.16 - 1\right)}\right]$$
$$+ 4.2873 \times 10^{-4} \left[10^{4.76955\left(1 - 273.16/T_{v(actual)}\right)} - 1\right] + 2.786118312$$

(3.26)

4. Evaluation of the numerical models

The accuracy of the numerical models used in this study will be examined in this section through a sensitivity analysis, as well as through a comparison of the results to test data and previous numerical work. The fan numbering scheme used hereafter is illustrated in Figure 4.1.

(a)   (b)
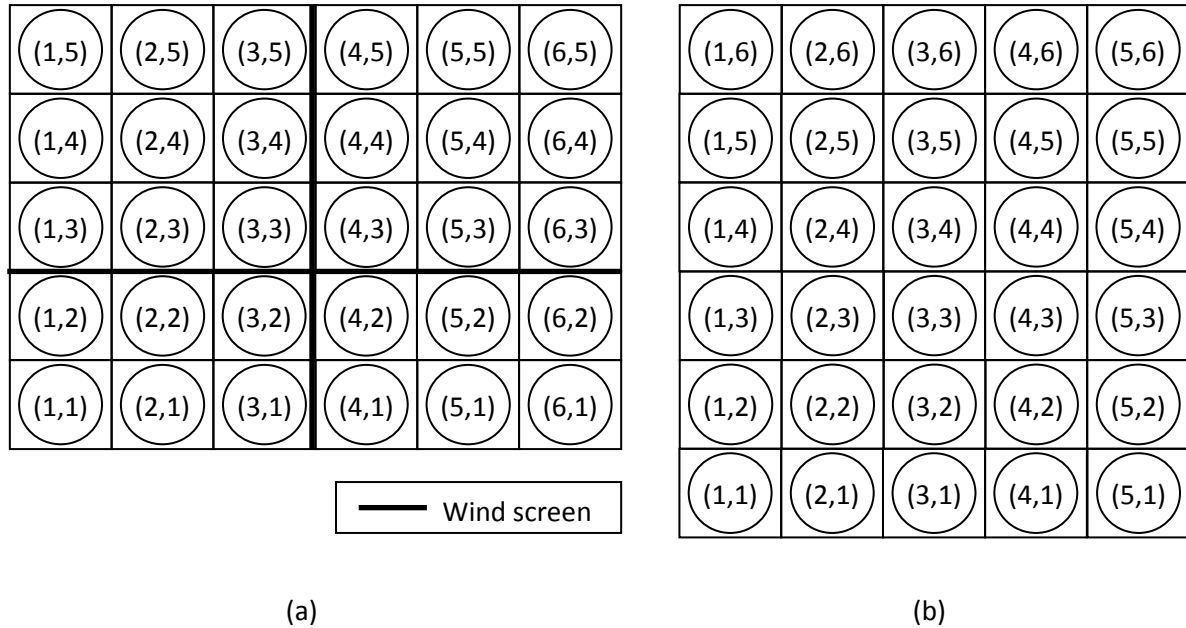
Figure 4.1:   Fan numbering scheme, (a) El Dorado, (b) Generic ACSC

4.1 Sensitivity analysis

Various user controllable model parameters have an influence on the accuracy of the results generated during a numerical simulation. It is necessary to design the numerical model to be as insensitive to these parameters as possible. The effects of grid resolution, profile boundary proximity to the ACSC, and global-to-detailed model iteration frequency are investigated in this section. The analyses were carried out using the generic ACSC subject to a straight-flow wind speed of $v_w = 3$ *m/s*.

4.1.1 Grid resolution

The effect of grid resolution on the numerical results was investigated through both manual and adaptive mesh refinement techniques. Special attention was paid to the region of the fan inlets and the upstream edge of the fan platform since it is expected that this is where

separation is likely to be most severe and, therefore, sufficient grid resolution most important. The effect of grid resolution on the numerical results is illustrated in Figure 4.2 for the cases described in Table 4.1.

Table 4.1: Grid resolution sensitivity cases: manual adaptation

Grid case number	Total number of cells	Number of cells on fan face
1	701 620	90
2	2 669 488	348
3	3 572 915	864
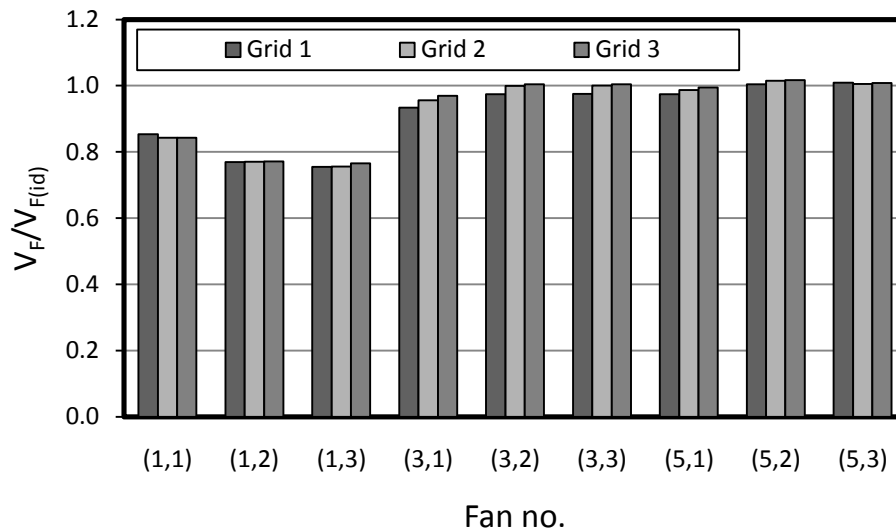
Figure 4.2: **The effect of grid resolution on the predicted volumetric effectiveness of certain ACSC fans**

Figure 4.2 indicates that the numerical results for grid cases 2 and 3 are similar and as such grid refinement beyond that of case 2 is not necessary. It can be concluded that the grid used in case 2 is of sufficient resolution that the results are largely grid independent.

Adaptive meshing was also used to investigate grid dependence in the numerical model. FLUENT's dynamic adaptive grid tool allows the user to run simulations where the grid is automatically refined in regions where a flow parameter gradient exceeds a set value. Gradients of static pressure were selected as the grid refinement criterion in an attempt to isolate grid refinement to the primary regions of interest, namely, in the vicinity of the fans

and in regions where separation occurs. Grid case 1 was used as the starting point and the solution finally converged at a grid resolution of $1.326 \mathrm{x} 10^{6}$ total cells with 1440 cells on the upstream fan faces. The predicted fan volumetric effectivenesses were comparable to those generated using grid case 2. The higher grid resolution on the fan face in the adaptive meshing solution, as opposed to grid case 2, can be attributed to the fact that FLUENT refines the grid in regions of high static pressure gradient. The static pressure discontinuity across the fan face will result in this face being refined during every refining operation.

Grid case 2 is of sufficient resolution that further mesh refinement is not justified. This grid was used in all simulations carried out as part of this study.

4.1.2 Boundary proximity

The effect of the proximity of the profile faces to the ACSC was investigated. These faces are the surfaces on which the necessary profiles are extracted from the global flow field model (see Figure 3.2), and form the flow domain boundaries in the detailed model (see Figure 3.4). The cases described below, and illustrated in Figure 4.3, were considered.

a) **Case 1**:   All boundaries located 20 m from the ACSC (as for Figure 3.2).

b) **Case 2**:   The upstream and downstream boundaries were moved to 50 m (x-direction expansion) while the top and side boundaries remained at 20 m.

c) **Case 3**:   The side boundaries were moved to 50 m (y-direction expansion) while the upstream, downstream and top boundaries remained at 20 m.

d) **Case 4**:   The top boundary was moved to 50 m (z-direction expansion) while the upstream, downstream and side boundaries remained at 20 m.
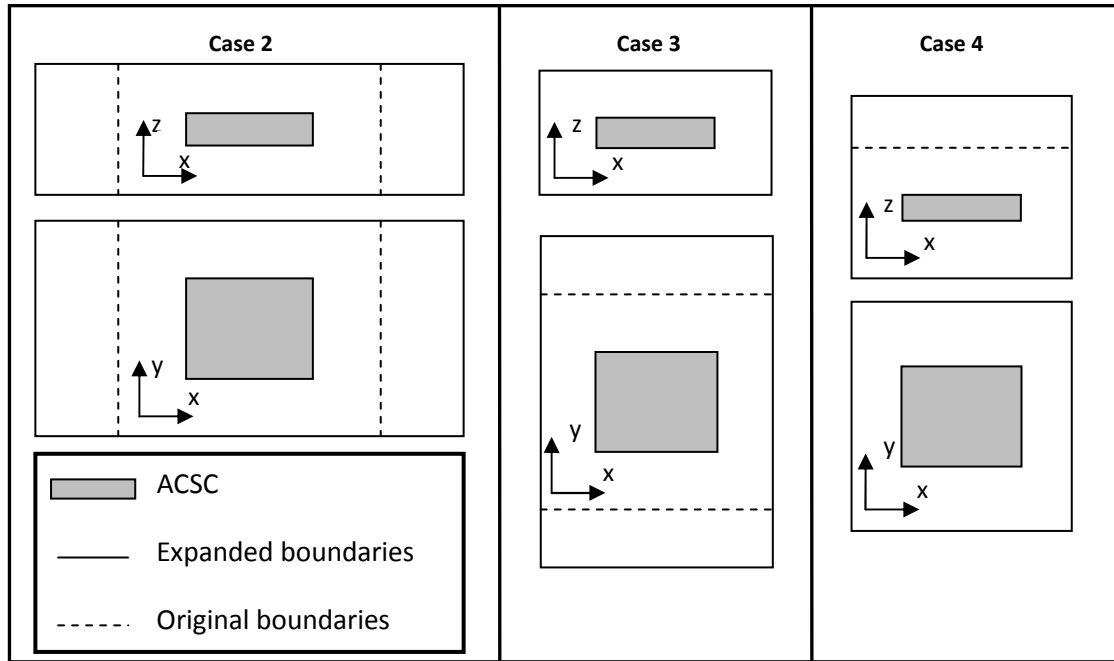
Figure 4.3: **Boundary proximity cases**

The effect of profile boundary proximity on the predicted fan volumetric effectiveness is illustrated in Figure 4.4.
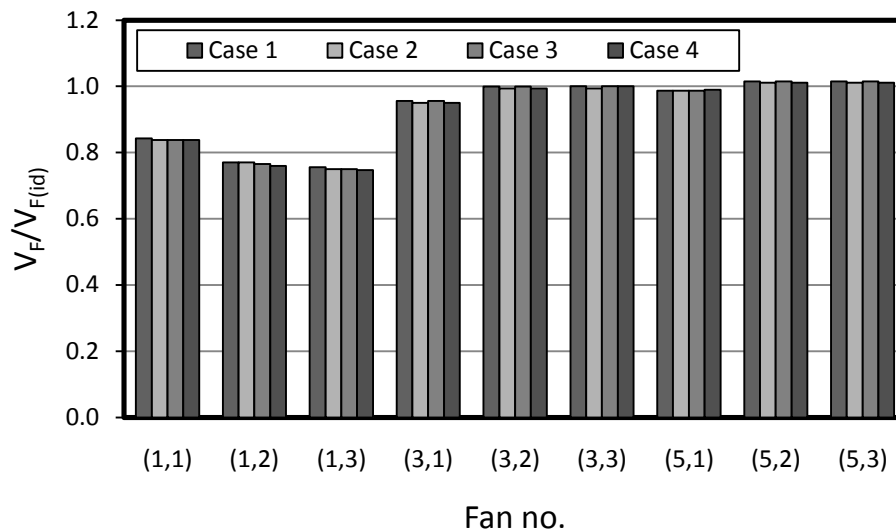
Figure 4.4: **The effect of profile boundary proximity on the predicted volumetric effectiveness of certain ACSC fans**

It is clear from Figure 4.4 that the simulation results are relatively insensitive to the proximity of the input boundaries to the ACSC in the detailed ACSC model. Case 1 was therefore selected for use in all simulations.

4.1.3 Global-to-detailed ACSC model iteration frequency

The iterative process followed during the numerical simulation of ACSC performance was described in Section 3.2. The effect of the number of global-to-detailed ACSC model iterations was investigated using the cases described below. A comparison of the simulation results, presented in Figure 4.5, clearly indicates that only a single iteration is necessary.

a) **Zero iterations**:   The profiles used in the detailed model are extracted from the global flow field model with the ACSC inlet and outlet velocities based on fan performance under ideal conditions.

b) **Single iteration**:   The ACSC inlet and outlet velocities in the global flow field model are updated using the predicted fan performance based on the zero iteration boundary profiles. The updated profiles from the global flow field are then used in the detailed model.

c) **Double iteration**: The fan performance determined in the detailed ACSC model based on the single iteration boundary profiles is used to determine the ACSC inlet and outlet velocities in the global flow field model and generate an updated set of profiles for use in the detailed model.
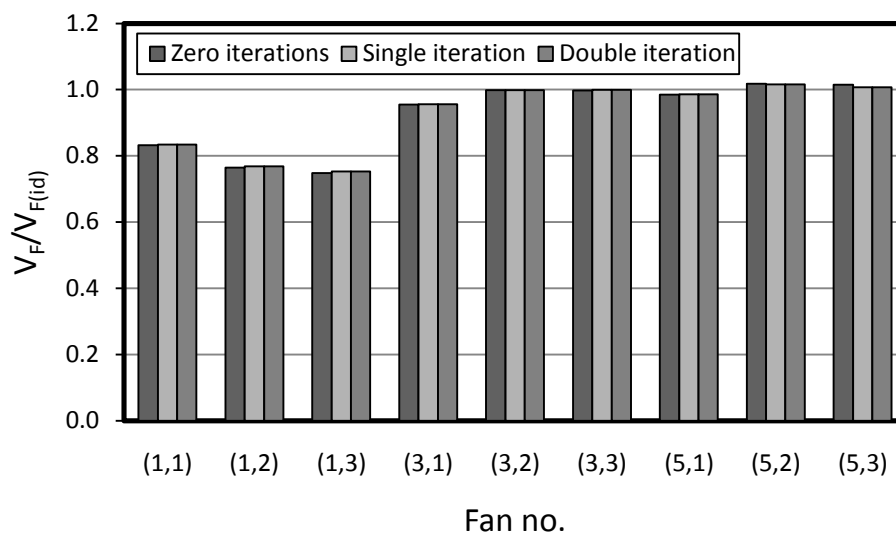
Figure 4.5:   **The effect of global-to-detailed ACSC model iteration frequency on the predicted volumetric effectiveness of certain ACSC fans**

4.2 Evaluation of the numerical model through a comparison to test data

In any numerical investigation it is necessary to validate the results through a comparison with test or experimental data. Full scale ACSC performance tests were carried out at El Dorado during September 2007 as described in Owen (2007). The data collected during these tests will be used for the purpose of verification of the numerical models employed in this study.

4.2.1 Turbine operation under ideal conditions

In order to determine the effect of various parameters on ACSC performance it is first necessary to know how the ACSC is expected to perform under ideal operating conditions. The turbine performance under ideal conditions is illustrated in Figure 4.6 (units have been removed for the purpose of confidentiality). This characteristic is based on test data for periods where there was no wind present ($v_w \leq 0.5$ m/s) and all ACSC fans were operating at full speed.
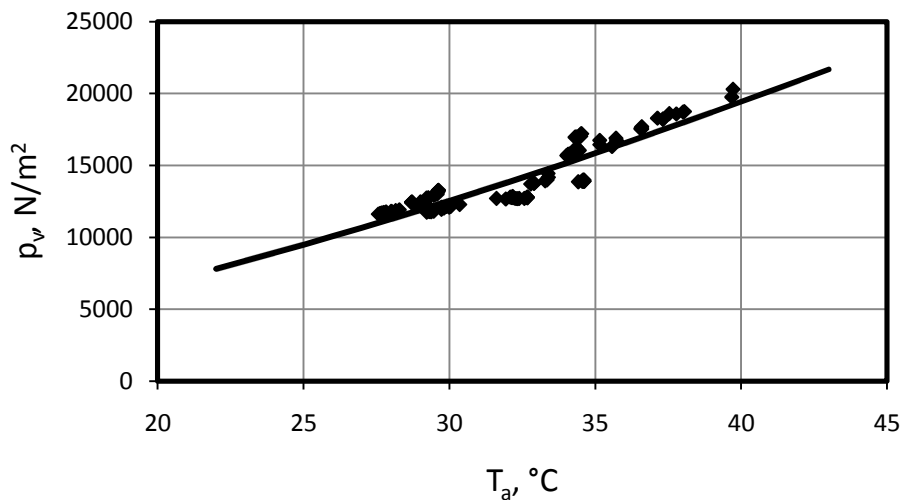
Figure 4.6:   **Turbine performance under ideal conditions**

A curve fit through the data yields a power law relationship between turbine backpressure and ambient temperature (in *°C*) under ideal operating conditions with all ACSC fans operating at full speed, as illustrated in equation (4.1).

$$p_{v(id)} = C_1 T_a^{C_2}$$

(4.1)

The turbine exhaust steam temperature, calculated as being the saturation temperature of steam at the turbine backpressure, is determined according to equation (4.2), as given by Kröger (2004).

$$
\begin{aligned}
T_v = {} & 164.630366 + 1.832295 \times 10^{-3}\, p_v + 4.27215 \times 10^{-10}\, p_v^2 + 3.738954 \times 10^3\, p_v^{-1} \\
& - 7.01204 \times 10^5\, p_v^{-2} + 16.161488 \ln(p_v) - 1.437169 \times 10^{-4}\, p_v \ln(p_v)
\end{aligned}
\tag{4.2}
$$

4.2.2 Test operating points

Periods of relatively stable wind conditions needed to be identified to provide suitable data for comparison with the numerical results. Wind speed stability was the primary consideration in the selection of suitable test periods. It was, however, attempted to select periods exhibiting consistent wind directions as well. Ultimately, four test periods, described in Table 4.2, were identified for comparison with the numerical results. Full descriptions of the wind and temperature data for each test period are included in Appendix G.

Table 4.2: Test data operating points

	TP1	TP2	TP3	TP4
T_a, $^\circ C$	30.1814	38.4999	36.2650	32.7049
$p_{v(actual)}$, N/m^2	14078.29	20692.84	18615.79	14164.87
v_w, m/s	5.5981	11.4495	7.9316	4.3333
θ_w, $^\circ$	206.2440	234.1740	236.503	261.1180
b	0.2850	0.2040	0.2179	0.1475
m_v, kg/s	128.9389	132.6066	131.1391	128.4598

In Table 4.2 T_a is the ambient temperature at fan platform height, $p_{v(actual)}$ is the pressure measured at the turbine exhaust. The mean wind direction over the test period is given by θ_w. The wind velocity at fan platform height and power law exponent, as described in equation (3.15), are given by v_w and b respectively. The mass flow rate of dry steam measured at the turbine exhaust is represented by m_v.

4.2.3 Comparison of numerical results to test data

The numerically predicted steam turbine backpressures at the four operating points described above are compared to the measured backpressures in Figure 4.7.
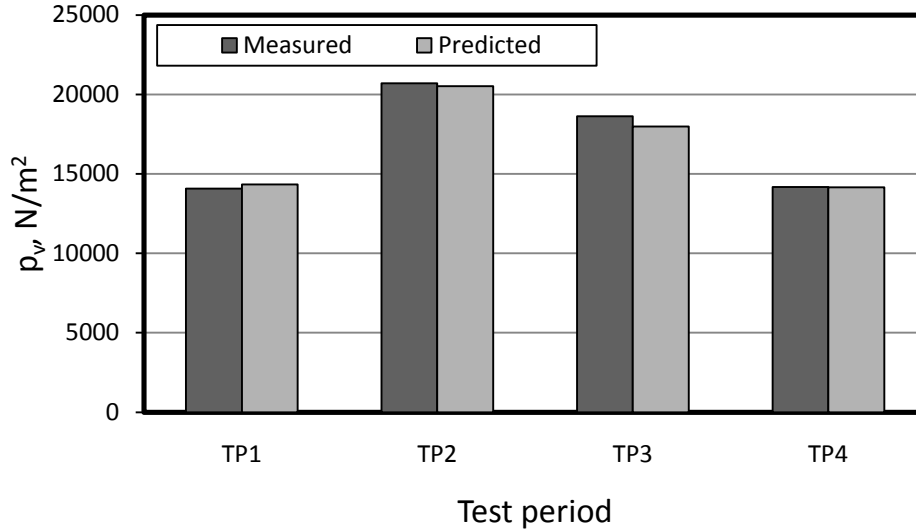
Figure 4.7: **Comparison of numerically predicted and measured steam turbine backpressure**

It should be noted that it was possible to calculate the heat to be rejected by the ACSC for each test operating point as follows,

$$Q_{TP} = m_v i_{fg} \tag{4.3}$$

where i_{fg} is the latent heat of vaporization of saturated water as given by Kröger (2004) and illustrated in equation (4.4).

$$i_{fg} = 3.4831814 \times 10^6 - 5.8627703 \times 10^3 T_v + 12.139568 T_v^2 - 1.40290431 \times 10^{-2} T_v^3 \tag{4.4}$$

Substitution of Q_{TP} in place of Q_{id} in equation (3.24) results in the removal of the constant heat transfer rate assumption and therefore yields more accurate numerical results.

A very good correlation is achieved between the numerical results and test data, with the largest discrepancy being a 3.4% under prediction of the steam turbine backpressure, corresponding to a $0.74°C$ discrepancy in the turbine exhaust steam temperature, for TP3.

Possible reasons for the small discrepancies include slight instabilities in the ambient conditions over the test periods (fluctuations in wind speed and direction for example); as well as numerical inaccuracies brought about by the pressure jump fan model, two step modelling approach and simplified heat exchanger model.

4.3 Evaluation of the numerical model through a comparison to previous numerical work

Van Rooyen (2008) carried out a numerical performance analysis on the generic ACSC considered in this study. The results generated using the numerical model described in this document will be compared to those presented by Van Rooyen (2008) in this section. Straight and cross-flow wind speeds of $v_w = 3\ m/s$, $v_w = 6\ m/s$ and $v_w = 9\ m/s$ were considered. Figure 4.8 illustrates a comparison of the numerically predicted volumetric effectivenesses of selected ACSC fans.

(a)

(b)
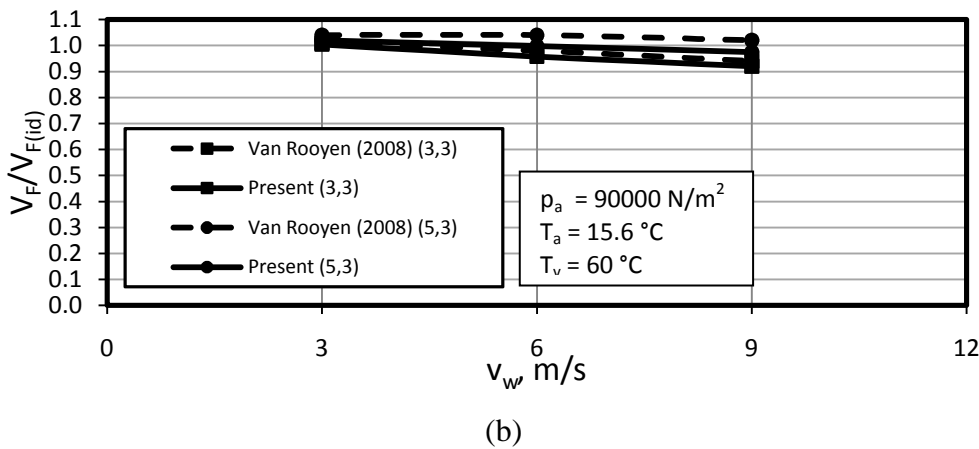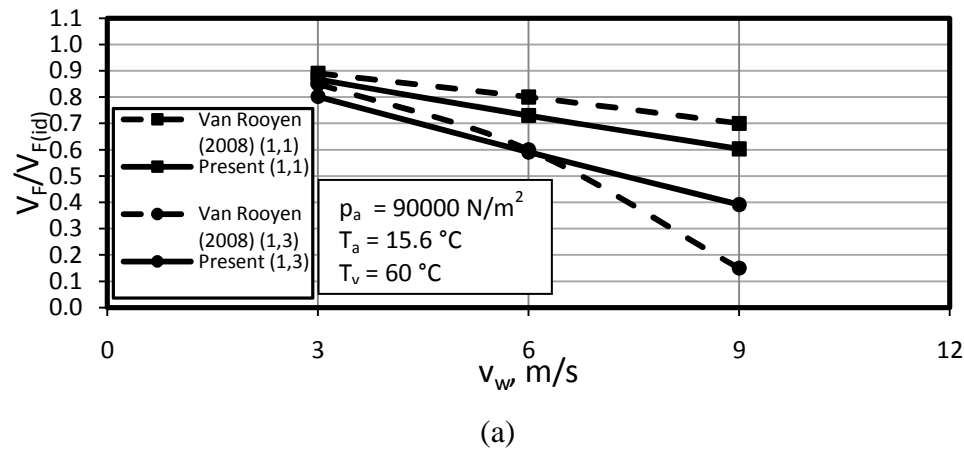
Figure 4.8: **Comparison of the numerically predicted volumetric effectivenesses of fans in (a) the upstream fan row, and (b) non-upstream fan rows, under straight-flow wind conditions**

41

The fan volumetric effectivenesses predicted under cross-flow wind conditions exhibit similar trends to those shown in Figure 4.8. A good correlation exists between the fan volumetric effectivenesses predicted by this study and those of Van Rooyen (2008) for most of the fans. The greatest discrepancies in the trends exist at the upstream fans under strong wind conditions. This is to be expected since it is here that the fan inlet flow conditions are most distorted. Any deficiencies in the fan models will therefore be exposed most severely at these fans. It is known that the actuator disk fan model, used by Van Rooyen (2008), deviates from true fan behaviour under highly distorted inflow conditions (Thiart and von Backström, 1993). It is also known that the pressure jump fan model used in this study provides limited accuracy where severe maldistribution of the flow occurs at the fan inlet (Van der Spuy et al., 2009). It can therefore be concluded that the use of different fan models contributes to the discrepancies in the results for these fans. Furthermore, the relatively low values found by Van Rooyen (2008) at $v_w = 9\ m/s$ for fan (1,3), as illustrated in Figure 4.8 (a), are in part due to the fact that he did not follow an iterative solution procedure. Subsequent to the publication of the results, Van Rooyen used the predicted fan performances to update the global flow field and generate a modified set of input profiles for use in the detailed ACSC model. The results of this iterative procedure saw a higher fan performance predicted at the wind speed in question, and as such, improves the agreement between the results.

A comparison of the predicted ACSC thermal effectivenesses is illustrated in Figure 4.9. Despite the discrepancies in the volumetric effectivenesses predicted for the upstream fans at high wind speeds, the thermal effectivenesses exhibit a strong correlation.
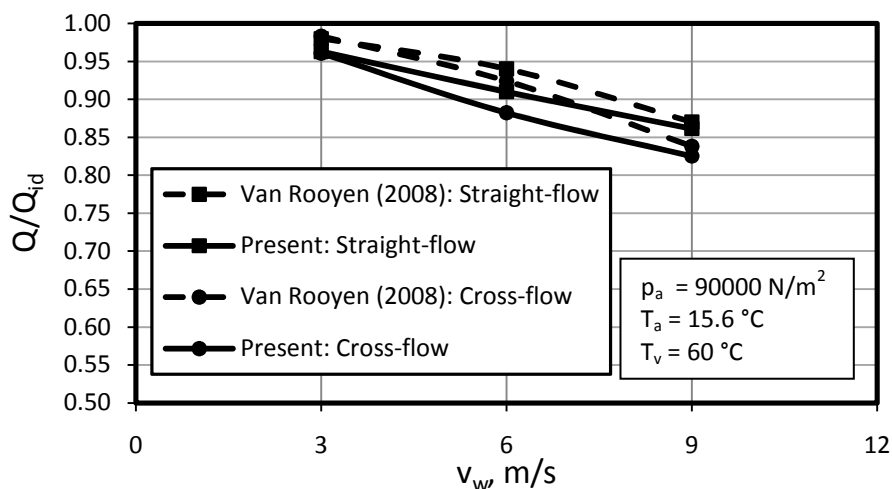
Figure 4.9: **Comparison of the numerically predicted ACSC thermal effectiveness**

5.   ACSC performance under windy conditions

Since air is used as the cooling medium in ACSCs, the achievable heat transfer rate is strongly influenced by atmospheric conditions. Gadhamshetty et al. (2006) mentions reductions in ACSC cooling effectiveness of up to 10% under unfavourable atmospheric conditions, namely strong winds and high ambient temperatures. Figure 5.1 illustrates the numerically predicted effect of wind and ambient temperature on ACSC heat transfer effectiveness at El Dorado.

(a)

(b)
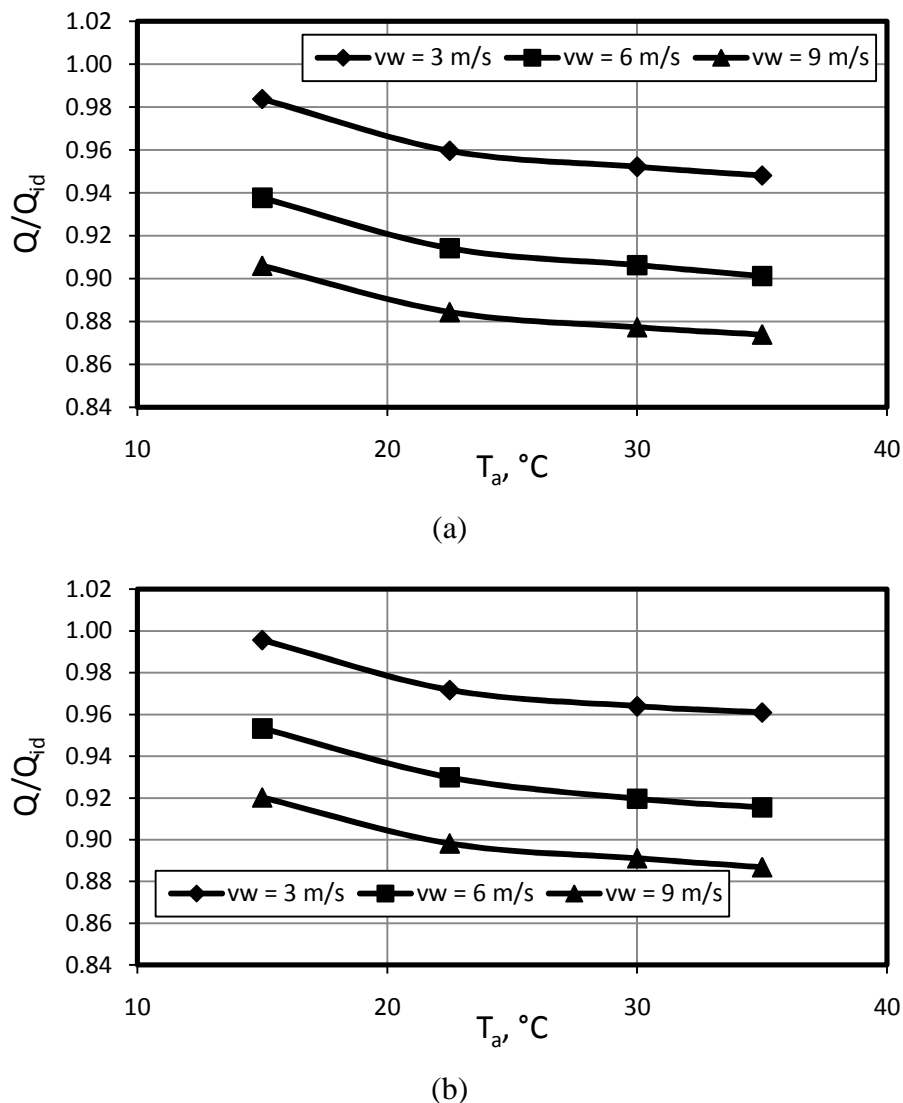
Figure 5.1:   Effect of ambient conditions on ACSC heat transfer effectiveness under (a) Straight-flow, and (b) cross-flow wind conditions

Figure 5.1 clearly illustrates the negative effect of both high ambient temperatures and strong winds on ACSC performance. It can be seen that an increase in ambient temperature of $\Delta T_a =$

20°C results in a decrease in ACSC heat transfer effectiveness in the region of 4%, while increasing the wind speed from $v_w = 3$ *m/s* to $v_w = 9$ *m/s*, at a constant ambient temperature results in a heat transfer effectiveness reduction in the region of 8%. It is clear that wind has a significant impact on ACSC performance. The effect of winds on ACSC performance will therefore be the focus of this study.

The effect of the decreased ACSC heat transfer effectiveness, illustrated in Figure 5.1, on the steam turbine backpressure, is illustrated in Figure 5.2. The trends exhibited in this figure correspond well with those identified by Maulbetsch and DiFilippo (2007) using test data from a number of ACSCs.

(a)

(b)
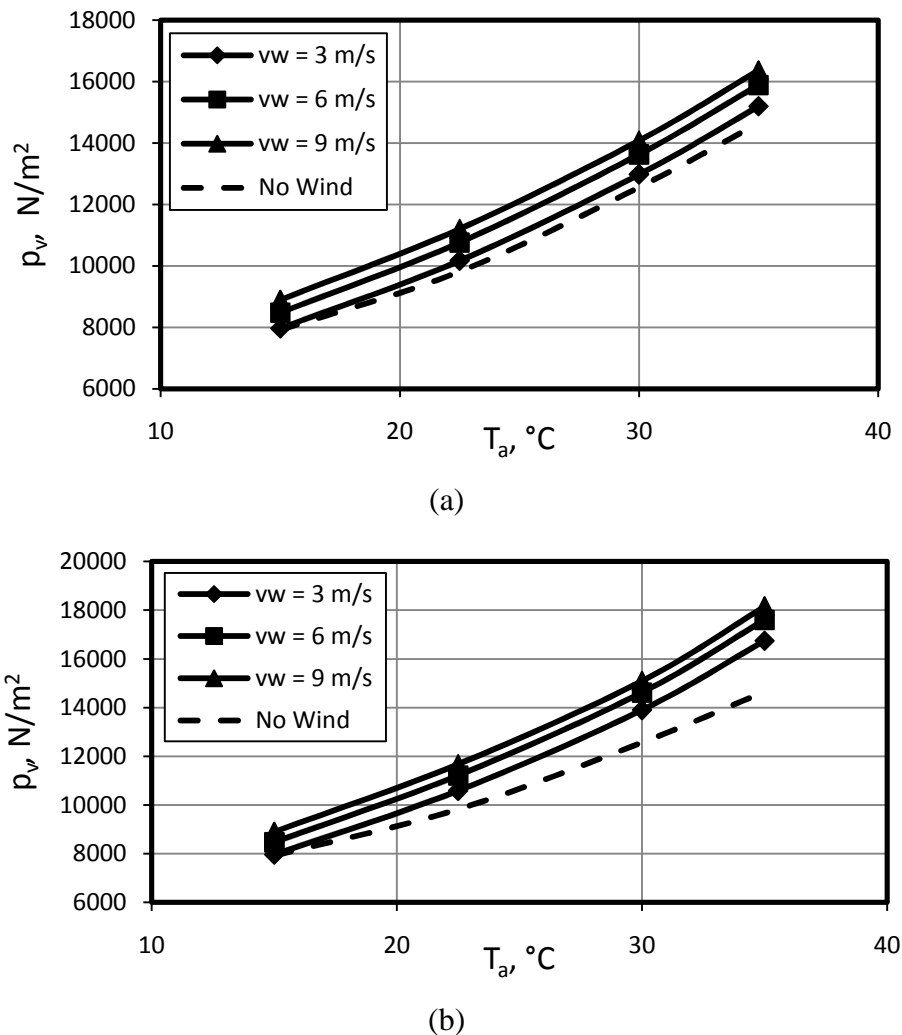
Figure 5.2: **Effect of ambient conditions on steam turbine backpressure under (a)**
Straight-flow, and (b) cross-flow wind conditions

44

Duvenhage and Kröger (1996) found that the negative effects of wind are as a result of reduced fan performance, brought about by distorted flow at the fan inlets, and hot plume recirculation. These phenomena will be examined in more detail hereafter.

5.1   Reduced fan performance due to distorted inlet conditions

Reduced fan performance due to distorted flow at the fan inlets occurs predominantly at the windward, or leading edge, fans. Previous studies have found reductions in the flow rates through these fans to be as high as 50% to 70% (Maulbetsch, 2008; McGowan et al., 2008). Figure 5.3 illustrates the numerically predicted fan volumetric effectivenesses for El Dorado under straight-flow wind conditions.
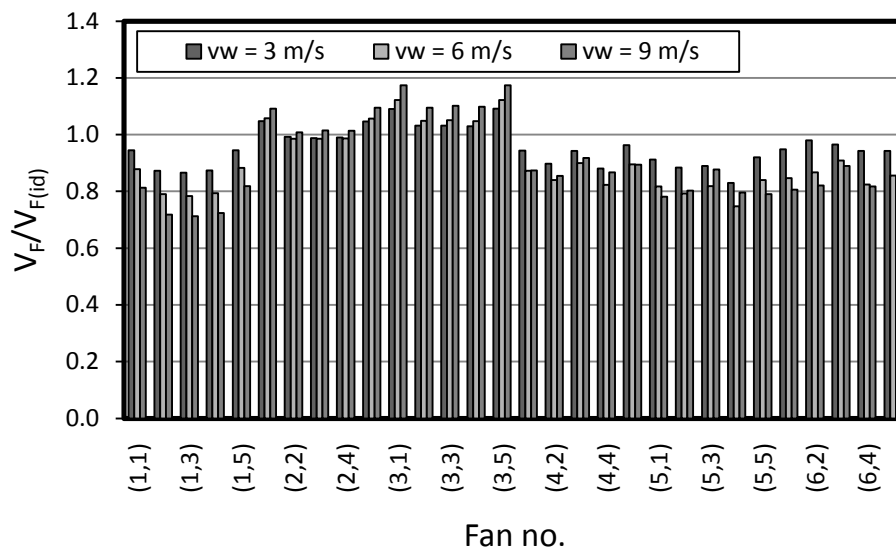
Figure 5.3:   **Fan volumetric effectiveness under straight-flow wind conditions**

It can be seen that the performance of the windward fans, namely fans (1,1) - (1,5), are the worst affected by wind. This is the result of distorted, or off-axis, flow conditions at the inlet to these fans caused by separation of the flow as it strikes the upstream edge of the ACSC. Figure 5.4 illustrates the low pressure zone under fan (1,1), as well as the off-axis flow at the fan inlet, caused by this separation.

<table>
<tr><td>(a)</td><td>(b)</td></tr>
</table>
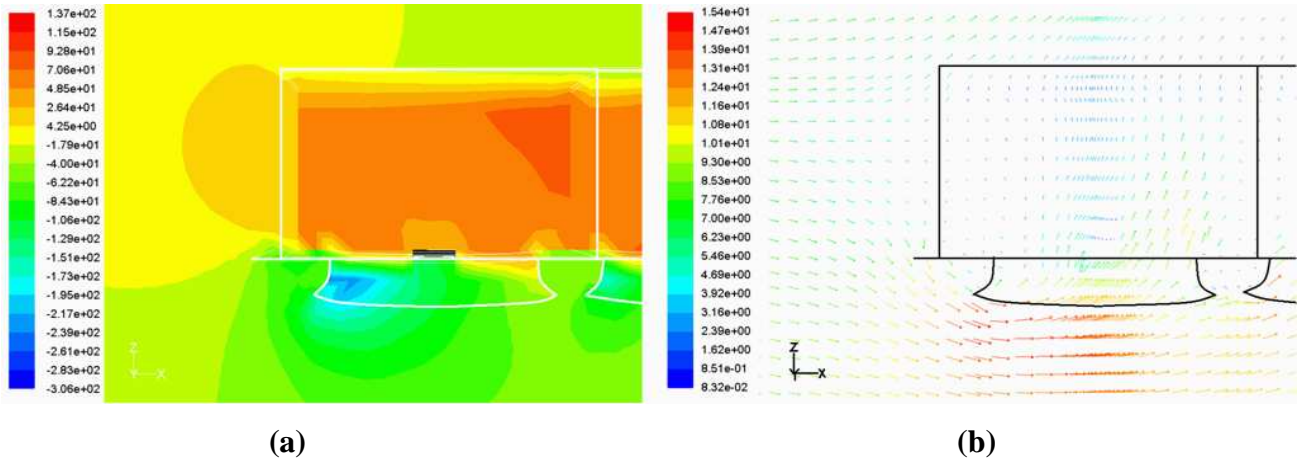
Figure 5.4: **Reason for the reduced performance of the windward fans: (a) Static pressure (p_s, N/m2), and (b) Vector plot (v, m/s) on a section through the centre of fan (1,1) for a straight wind speed of $v_w = 9m/s$**

It should also be noted that the fans located immediately upstream of the windscreens, namely fans (2,1) - (2,5) and (3,1) - (3,5), perform well under windy conditions. It is predicted that the performance of some of these fans can be enhanced above that achieved under ideal conditions. This can be attributed to the stagnation effect of the wind screens on the flow immediately upstream of their location, as illustrated in Figure 5.5.
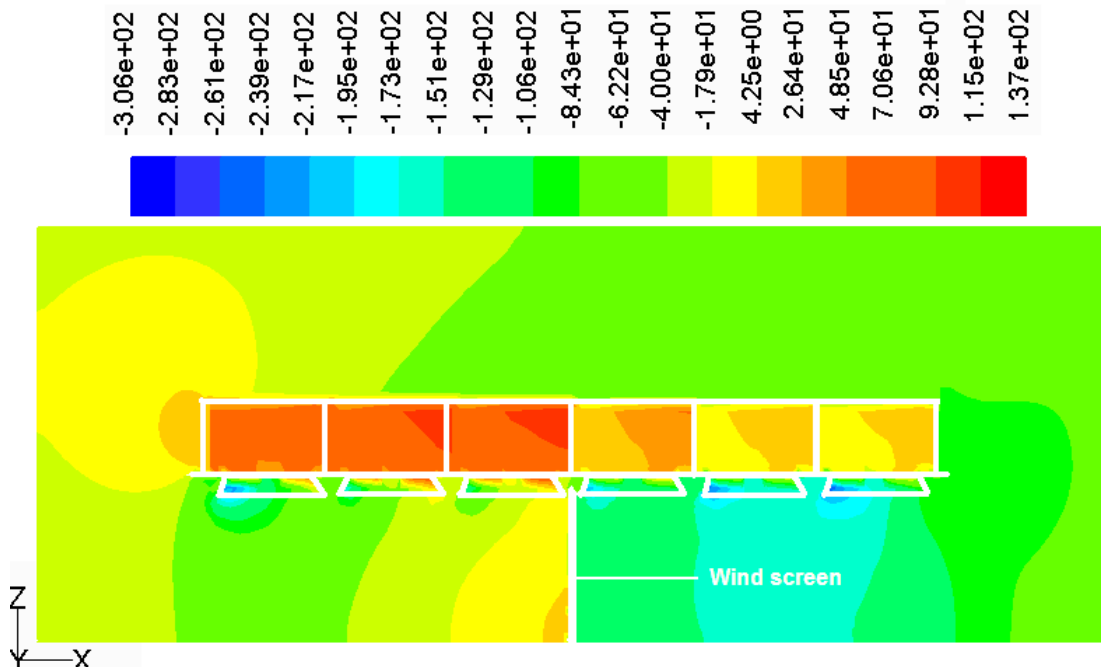
Figure 5.5: **Static pressure (p_s, N/m2) along a fan row for a straight wind speed of $v_w = 9m/s$**

The installation of windscreens therefore holds potential for improving ACSC performance under windy conditions and warrants further investigation. With El Dorado's current screen configuration, however, the fans immediately downstream of the windscreens perform relatively poorly. It is suspected that the current screen configuration may be causing an excessive blockage effect and is effectively suffocating the downstream fans. The identification of some optimum windscreen configuration where the performance of the upstream fans is improved without reducing the performance of the downstream fans significantly would be a worthwhile exercise and is addressed later in this document.

5.2   Hot plume recirculation

Hot plume recirculation is predominant at the downstream ACSC edges and corners, as illustrated in Figure 5.6 where the inlet temperatures of the fans (5,1) - (5,5) and (6,1) - (6,5) are higher than the ambient temperature of $T_a = 19.44°C$.
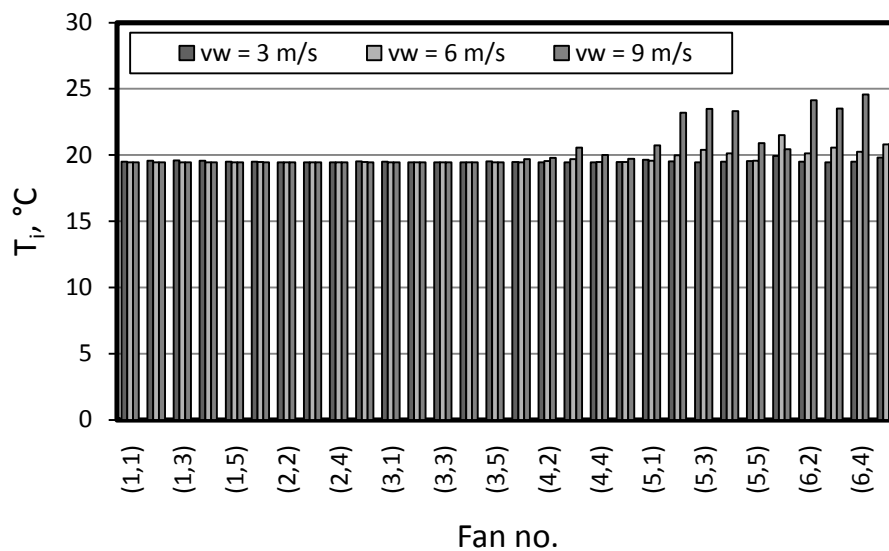
Figure 5.6:   **Inlet temperatures at ACSC fans under straight-flow wind conditions**

Plume recirculation is caused by entrainment of hot air from the heat exchanger outlet in vortex's that form from the leading edge of the fan platform under windy conditions. Figure 5.7 illustrates the vortex formed at El Dorado's ACSC for a straight wind speed of $v_w = 9 \, m/s$. The size of the vortex increases in the downstream direction resulting in increased entrainment of the plume. Eventually the vortex diameter grows large enough to force hot air below the fan platform and into the region from which the fans draw their air. The downstream fans lie in this large vortex region and are therefore worst affected by plume

recirculation. Figure 5.6 also illustrates an increase in the severity of recirculation with increasing wind speed. This can be attributed to the plume being forced closer to horizontal with increasing wind speed. This effect is shown in Figure 5.8
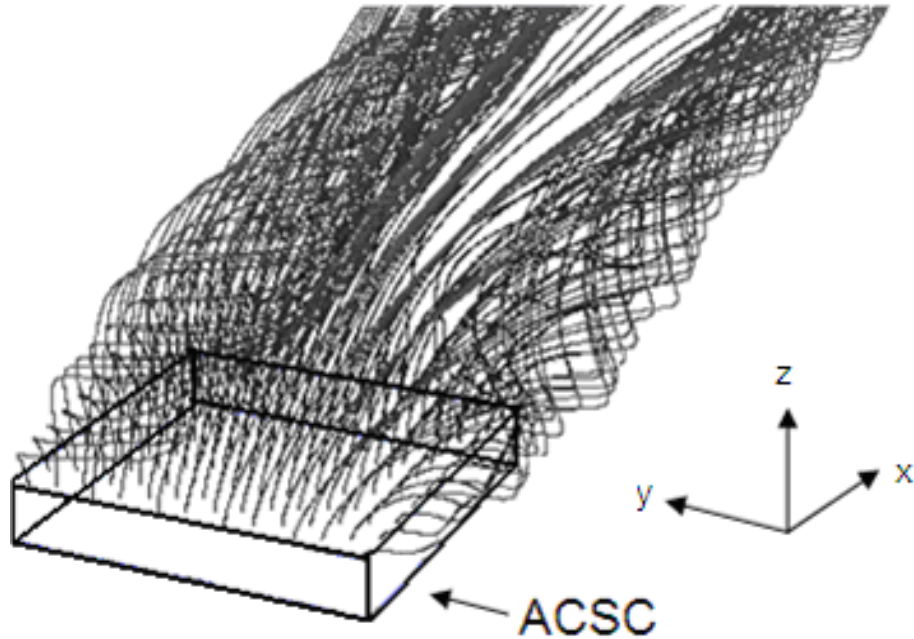
Figure 5.7: **Vortex formed due to the presence of a straight wind ($v_w = 9m/s$)**
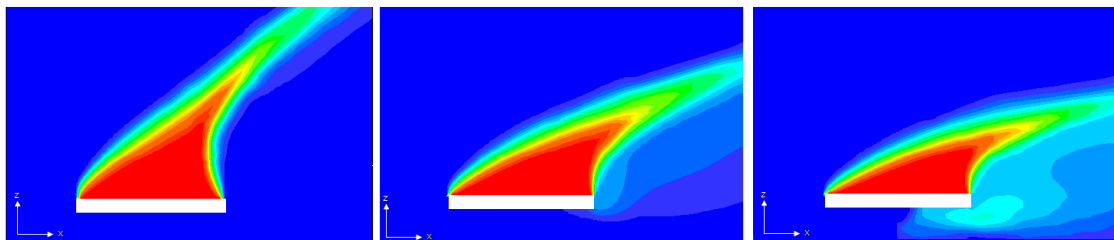
Figure 5.8: **Plume angle for straight wind speeds of (a) $v_w = 3 \ m/s$,**
(b) $v_w = 6 \ m/s$, and (c) $v_w = 9 \ m/s$

5.3 Identification of the primary cause of ACSC performance reduction under windy conditions

Maulbetsch (2008) states that, at the ACSCs tested by him, the effect of hot plume recirculation on ACSC performance is small for most wind conditions while fan performance reductions are often significant. The separate effects of reduced fan performance and plume recirculation on ACSC heat transfer effectiveness, as well as the effect of the two phenomena combined, is illustrated in Figure 5.9. Reduced fan performance is clearly the largest

contributor to the reduction in ACSC performance under windy conditions and will subsequently be the focus of the remainder of this study.
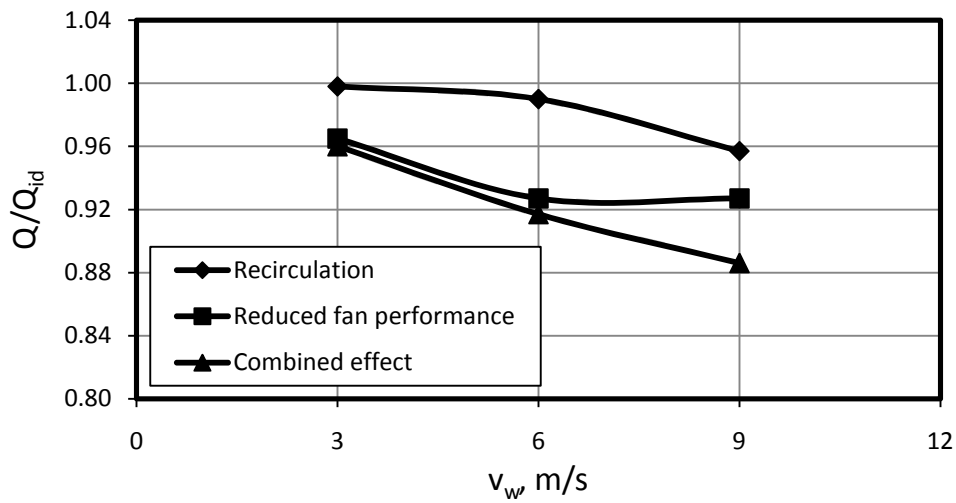
Figure 5.9: **Illustration of the contribution of reduced fan performance and hot plume recirculation to reduced ACSC performance under straight-flow wind conditions at El Dorado**

6. Evaluation of wind effect mitigation measures

6.1 Wind screens

The previous section of this document indicated that the installation of wind screens can result in an increase in the performance of certain ACSC fans under windy conditions. Since the ACSC heat transfer rate is directly proportional to the mass flow rate of air through the finned tube heat exchangers, it follows that the installation of wind screens can potentially reduce the negative effect of wind on ACSC performance. The results presented in the previous section also indicated, however, that certain fans, those immediately downstream of the wind screen location in particular, can be adversely affected by the presence of these screens. The installation of an appropriate wind screen configuration is therefore important to ensure maximum benefit. An attempt will be made to identify an optimum wind screen configuration for El Dorado's ACSC in this section.

6.1.1 Evaluation of the current wind screen configuration at El Dorado

El Dorado has wind screens installed in a configuration as illustrated in Figure 6.1 and described in Table 6.1. The location of the screens below the platform is illustrated in Figure 4.1.
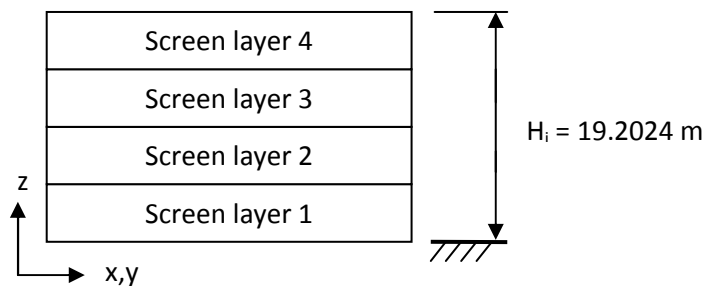
Figure 6.1:   Wind screen configuration at El Dorado

Table 6.1:   Loss coefficients (K_{sc}) of wind screens used in the current configuration at El Dorado

	N-S screens	E-W screens
Screen layer 4	2	5
Screen layer 3	10	10
Screen layer 2	∞	∞
Screen layer 1	∞	∞

Three wind screen materials are used at El Dorado; namely a 90% closed area screen material, a 65% closed area screen material, and a 55% closed area screen material. A double layer of the 65% closed area wind screen material is installed in Screen layer 3 of both the N-S and E-W orientated wind screen configurations. Wind tunnel tests were used to determine the loss coefficients of the wind screen materials (see Appendix H for a full description of the test setup and results). The screen material loss coefficients are listed in Table 6.2.

Table 6.2: Wind screen material loss coefficients

Wind screen material description	$K_{sc} = \rho_a v_a^2 / 2$
55% closed area	2
65% closed area	5
90% closed area	∞

The 55% and 65% closed area wind screens were represented using the radiator boundary condition (see Section 3.1.5) in the numerical ACSC model, with the loss coefficients as listed in Table 6.2, and with the radiator heat transfer coefficient set to zero. The 90% closed area screen material essentially behaved as a solid obstruction to the flow in the wind tunnel tests and these screens were subsequently modelled using the wall boundary condition.

Figure 6.2 illustrates the effect of El Dorado's current wind screen configuration on ACSC performance under windy conditions. It is clear from this figure that the wind screens are beneficial to ACSC performance under windy conditions.
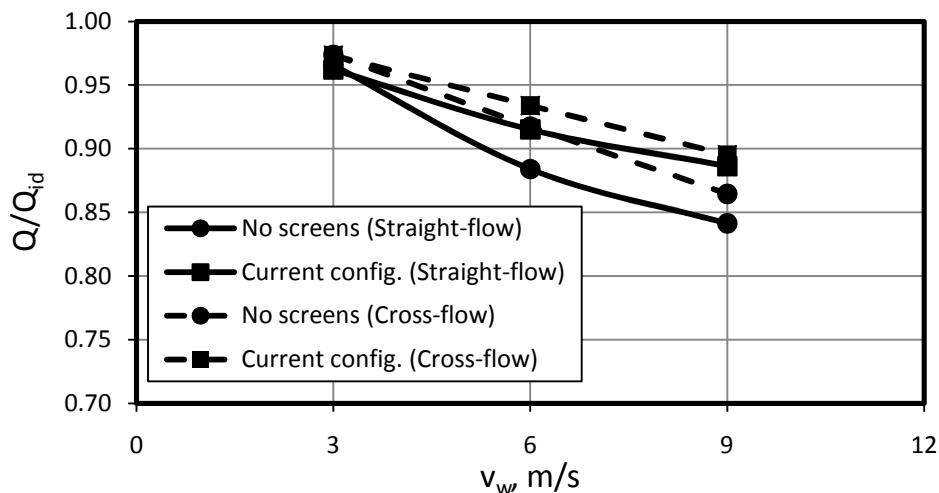
Figure 6.2: **Effect of current wind screen configuration on ACSC performance at El Dorado**

It can be seen in Figure 6.3, however, that while the presence of the wind screens improves the volumetric effectiveness of the fans upstream of the screen location (refer to Figure 4.1), the volumetric effectivenesses of the fans downstream of the screen location are adversely affected. While the net effect on ACSC performance is still positive in this case, it could be possible to achieve even greater improvement if some optimum screen configuration can be found that has similar positive effects on the upstream fans but less of a negative effect on the downstream fans.
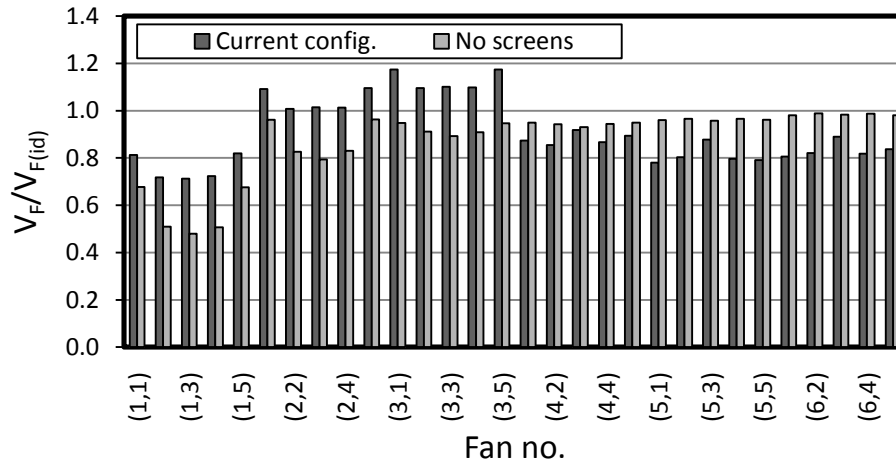
Figure 6.3: **Effect of current wind screen configuration on fan volumetric effectiveness for a straight-flow wind speed of v_w = 9 m/s at El Dorado**

6.1.2 Evaluation of alternative wind screen configurations

Six alternative wind screen configurations were evaluated in an attempt to find an improved configuration at El Dorado. Table 6.3 describes the configurations considered (note that the same configuration is used for the N-S and E-W orientated screens). It was decided not to investigate changing the wind screen locations.

Table 6.3: Alternative wind screen configurations

	Config. 1	Config. 2	Config. 3	Config. 4	Config. 5	Config. 6
$K_{sc} = \rho_a v_a^2 / 2$						
Screen layer 4	5	5	2	5	0	0
Screen layer 3	10	10	5	5	10	0
Screen layer 2	∞	10	5	∞	∞	∞
Screen layer 1	∞	∞	∞	∞	∞	∞

The effect of the wind screen configurations on ACSC heat transfer effectiveness is illustrated in Figure 6.4.
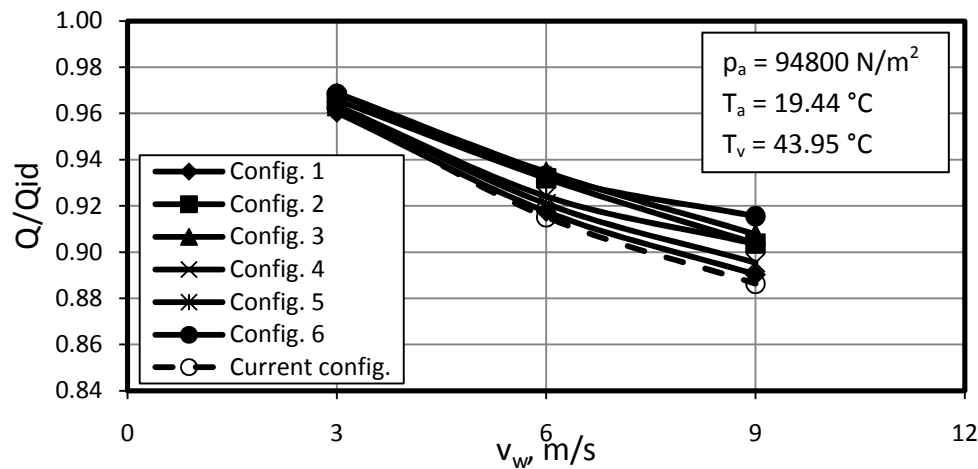
(a)
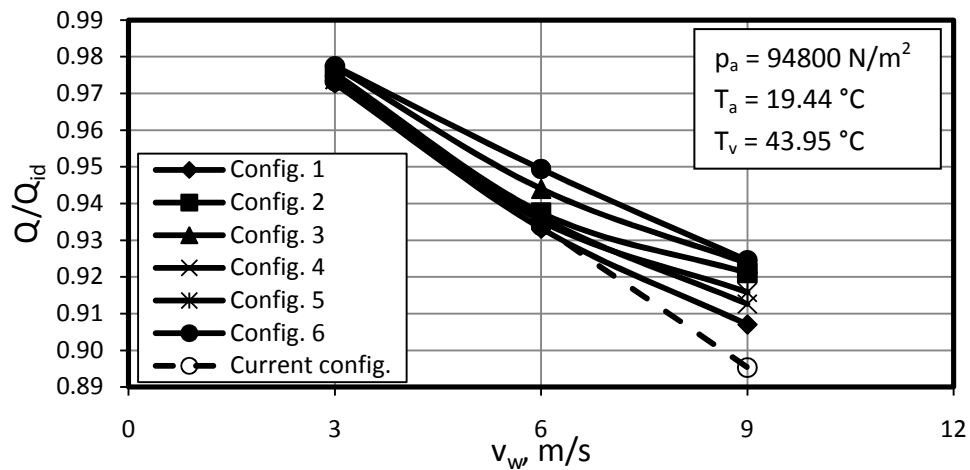
(b)

Figure 6.4:   **Effect of alternative wind screen configuration on ACSC performance for (a) Straight-flow, and (b) Cross-flow wind conditions**

Figure 6.4 shows that it is possible to improve the ACSC performance at El Dorado through the installation of an alternative wind screen configuration in the current wind screen location. Configuration 6 (where high loss coefficient screens are installed to a height of $H_{sc}/H_i = 0.5$) appears to provide the best performance in general, with performance enhancements comparable to the other configurations at low and intermediate wind speeds and superior performance at high wind speeds.

A comparison of the volumetric effectivenesses of the ACSC fans for the current screen configuration and Configuration 6 is shown in Figure 6.5. It can be seen that the current wind

screen configuration has a larger positive effect on the performance of the fans upstream of the wind screen location. This is to be expected since the current configuration provides a greater obstruction to the flow under the ACSC and as such has a more significant stagnation effect. The superior performance of Configuration 6 is as a result of the improved performance of the fans downstream of the wind screen location. This is caused by a reduction of the choking effect of the wind screens on the downstream fans brought about by the removal of the screens in Screen layers 3 and 4.
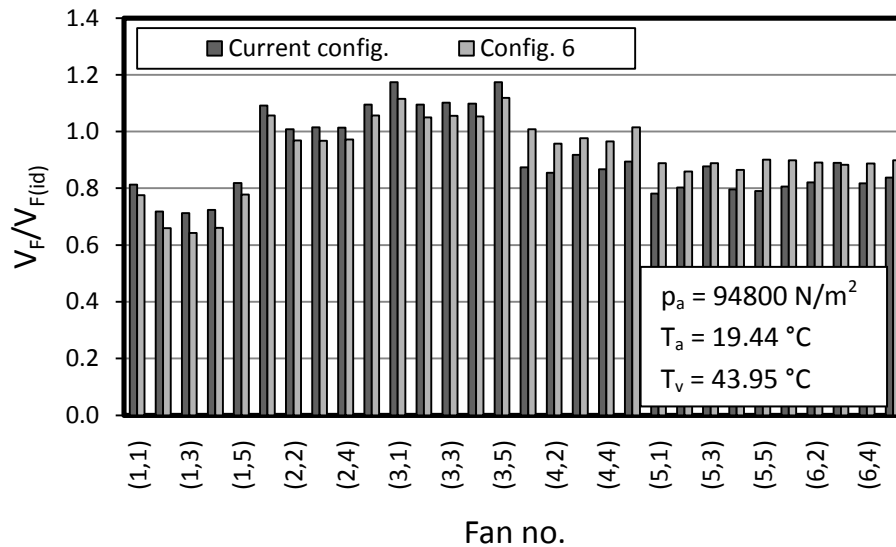
Figure 6.5: **A comparison of the effect of an alternative wind screen configuration on ACSC fan performance at El Dorado**

It appears that an improved wind screen configuration has been identified in the form of Configuration 6. It was hypothesized that reducing the wind screen loss coefficient in this configuration may result in further ACSC performance improvement. The results of an investigation into the effect of the wind screen loss coefficient on ACSC performance, illustrated in Figure 6.6, indicate that an optimum loss coefficient exists in the range $5 \leq K_{sc} \leq 10$ for Screen Configuration 6. For $v_w = 9\ m/s$ the optimum lies closer to $K_{sc} = 10$. Since ACSC performance is most severely affected at high wind speeds, $K_{sc} = 10$ was selected as the optimum wind screen loss coefficient for Configuration 6.
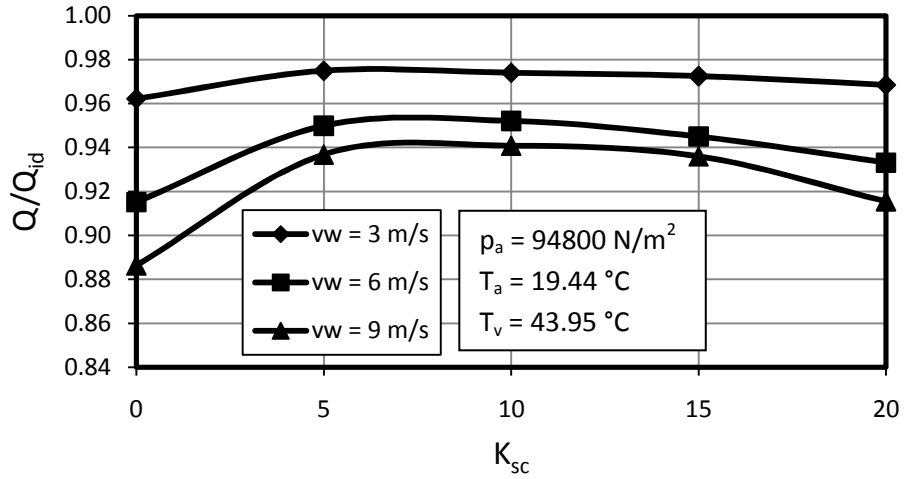
(a)
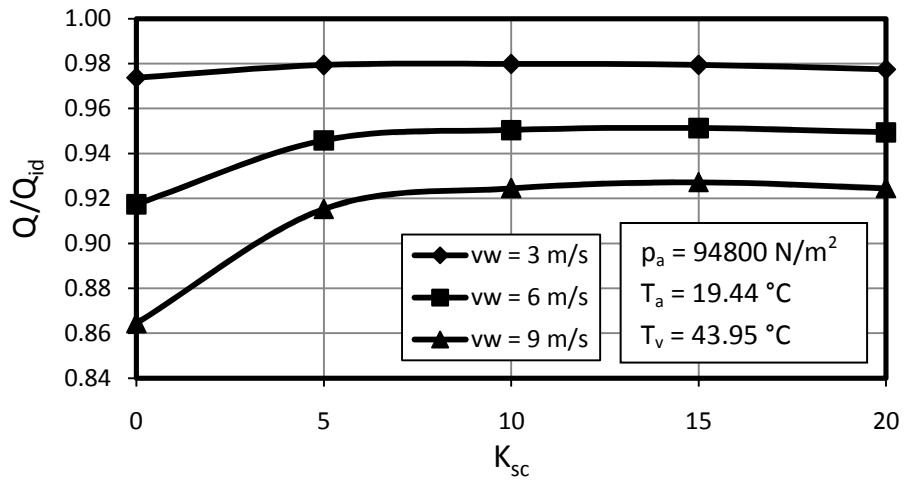
(b)

Figure 6.6: **Effect of wind screen loss coefficient on ACSC performance under (a) Straight-flow, and (b) Cross-flow wind conditions for Screen Configuration 6**

The question now remains whether the wind screen height, $H_{sc}/H_i = 0.5$, remains the optimum height if the screen loss coefficient is reduced to $K_{sc} = 10$. Figure 6.7 shows the results of an investigation into the effect of wind screen height on ACSC performance for a screen loss coefficient of $K_{sc} = 10$, and indicates that $H_{sc}/H_i = 0.5$ remains the optimum screen height.

55
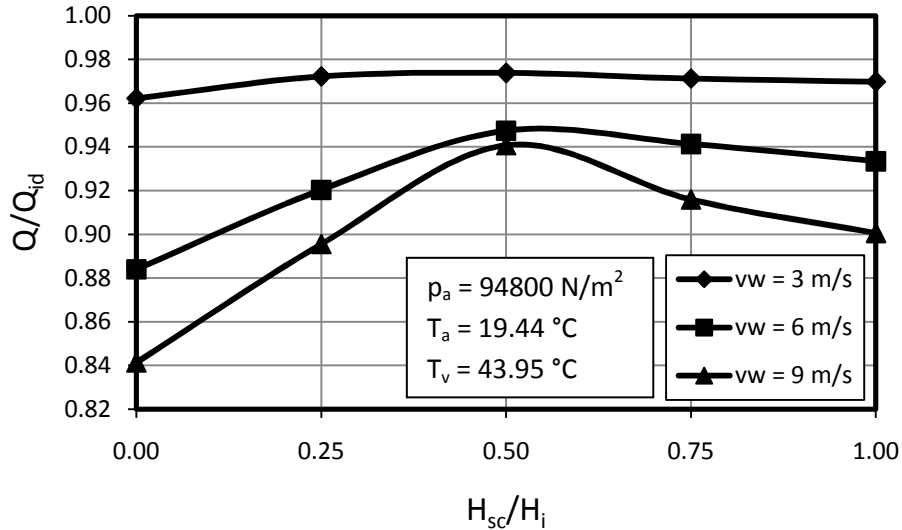
Figure 6.7: **Effect of wind screen height on ACSC performance for $K_{sc} = 10$ under straight-flow wind conditions**

6.2 Walkways

The effect of the addition of solid walkways on ACSC performance under windy conditions has been investigated in previous studies. Salta and Kröger (1994) recommend the addition of a solid walkway along the periphery of the fan platform, with a width in the range *0.159 ≤ L_w/d_F ≤ 0.476* (where L_w is the walkway width), based on experimental data. Bredell (2006) numerically investigated the effect of a solid walkway ($L_w/d_F = 0.333$) on fan performance in an ACSC and predicts a significant improvement in the performance of the edge fans under windy conditions.

El Dorado has solid walkways, of width *$L_w/d_F = 0.12$*, installed along the periphery of the fan platform. It was therefore decided not to investigate walkways as a wind mitigation measure at El Dorado. The use of walkways as a means of reducing the negative effects of wind on ACSC performance, however, remains an interesting topic and will be investigated here using the generic ACSC.

Bredell (2006) deduced that the installation of walkways along the periphery of the fan platform results in increased flow rates through the edge fans as a result of a reduction in the cross-flow velocity and abatement of the separation or distortion that occurs at the inlet of these fans. Figure 6.8 illustrates the effect of a solid walkway of width *$L_w/d_F = 0.29$* on the

static pressure distribution below the ACSC fan platform for a straight-flow wind speed of v_w = 9 m/s. The walkway appears to shift the low pressure region associated with separation, or distorted flow, further upstream. A smaller portion of the upstream fan row is therefore exposed to the distorted inflow conditions, resulting in improved performance at these fans relative to the no walkway case.
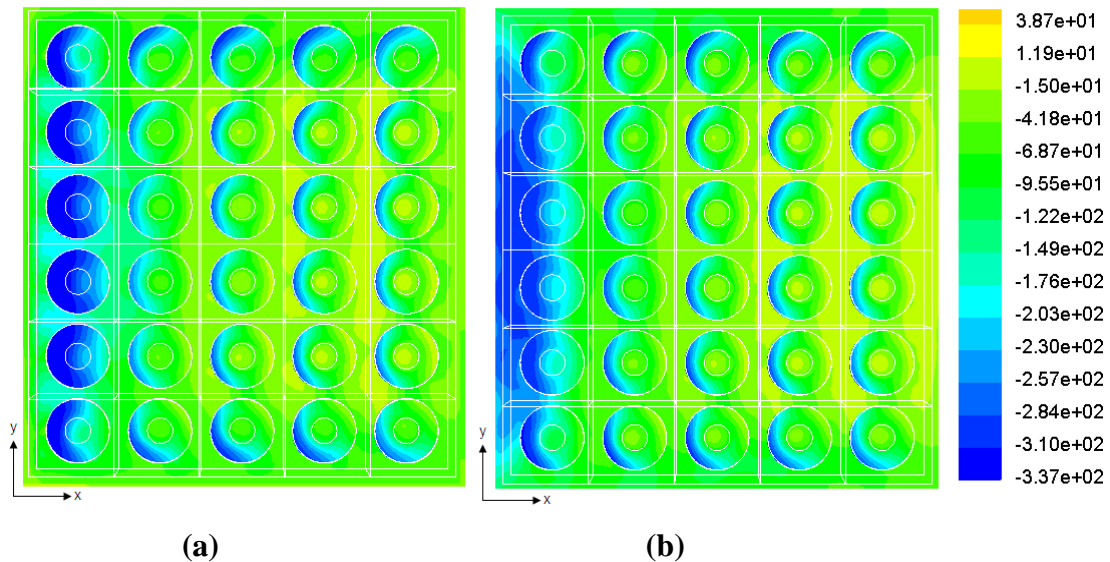
Figure 6.8: **Static pressure distribution below the fan platform (a) With no walkway present, and (b) With a solid walkway present ($L_w/d_F = 0.29$); for a straight-flow wind of $v_w = 9$ m/s**

While it is clear that the addition of a solid walkway along the periphery of the fan platform is valuable, some questions regarding optimum walkway width remain. The effect of walkway width on ACSC performance under windy conditions was subsequently investigated. The results illustrated in Figure 6.9 indicate that ACSC performance under windy conditions increases with walkway width but that the gain in ACSC performance per unit walkway width increase diminishes as the width increases.

57
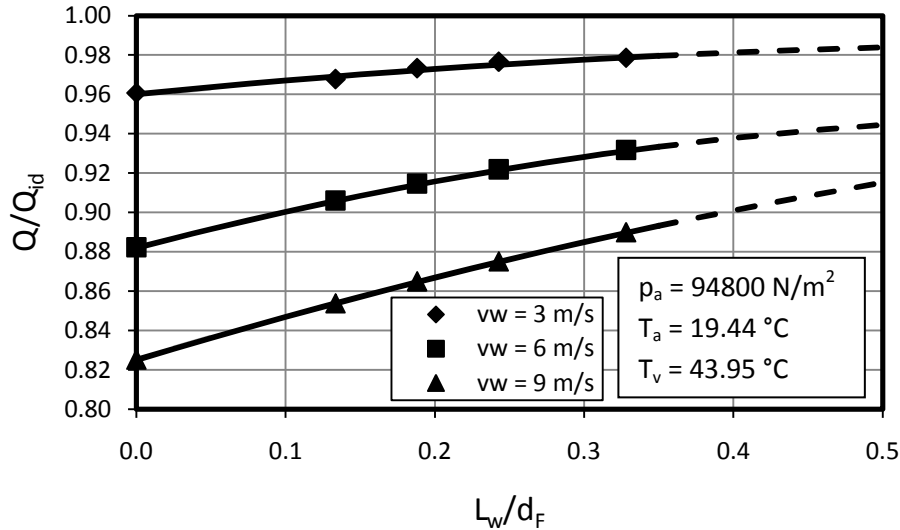
Figure 6.9: **Effect of walkway width on ACSC performance under windy conditions for the generic ACSC**

6.3 Increasing fan power

Since the ACSC heat transfer rate is directly proportional to the mass flow rate of air through the finned tube heat exchanger, it is possible to improve ACSC performance during periods of strong winds and/or high ambient temperatures by increasing the mass flow rate through the fans. One way of achieving this is to increase the fan power. However, while increasing fan power may result in improved ACSC and steam turbine performance under unfavourable operating conditions, the additional fan power required must be compared to the gain associated with the improved turbine performance in order to determine the net benefit of this method. The value of increasing fan power, as a method to improve net steam turbine power output under windy conditions, at El Dorado will be investigated here.

The effects of increasing the power of all the ACSC fans, hereafter referred to as the "all fans" case, as well as the effects of increasing the power of only the periphery fans, as suggested by Liu et al. (2008) and hereafter referred to as the "periphery fans" case, were investigated. Fan power increases of 5%, 12.5%, 20%, 30% and 40% were considered.

New fan performance characteristics were generated for the increased fan power cases based on the design fan performance characteristic and the fan laws, as given in Kröger (2004) and presented in equations (6.1) - (6.4).

$$\frac{P_F}{P_{Fd}} = \left(\frac{N_F}{N_{Fd}}\right)^3 \left(\frac{\rho_a}{\rho_{ad}}\right) \qquad (6.1)$$

$$\frac{\Delta p_{Fs}}{\Delta p_{Fsd}} = \left(\frac{N_F}{N_{Fd}}\right)^2 \left(\frac{\rho_a}{\rho_{ad}}\right) \qquad (6.2)$$

$$\frac{V_a}{V_{ad}} = \frac{N_F}{N_{Fd}} \qquad (6.3)$$

$$\eta_F = \eta_{Fd} \qquad (6.4)$$

In equations (6.1) to (6.4) N_F and N_{Fd} are the fan rotational speed at the increased fan power and the design power respectively. P_F is the increased fan power, while P_{Fd} is the design fan power. The same applies for the fan static pressure Δp_{Fs}, volume flow rate V_a, and static efficiency η_F. The actual and design air densities are ρ_a and ρ_{ad} respectively.

Figure 6.10 shows how increasing fan power results in decreased turbine backpressure and subsequently improved turbine efficiency. While this is expected, it remains to be proven whether or not increasing fan power results in a net plant power output gain.

In order to determine the net plant power output gain/loss it is necessary to know the relationship between the steam turbine power output and backpressure. In the absence of this information for the turbine used at El Dorado, the turbine characteristic illustrated in Figure 6.11 was used. This curve is typical of a steam turbine selected for use in a combined-cycle power plant with an ACSC (EPRI, 2005). It must therefore be noted that the results presented hereafter are not accurate for El Dorado but should, none the less, give some indication of the value of increasing fan power as a means of improving steam turbine performance under windy conditions.

(a)

(b)
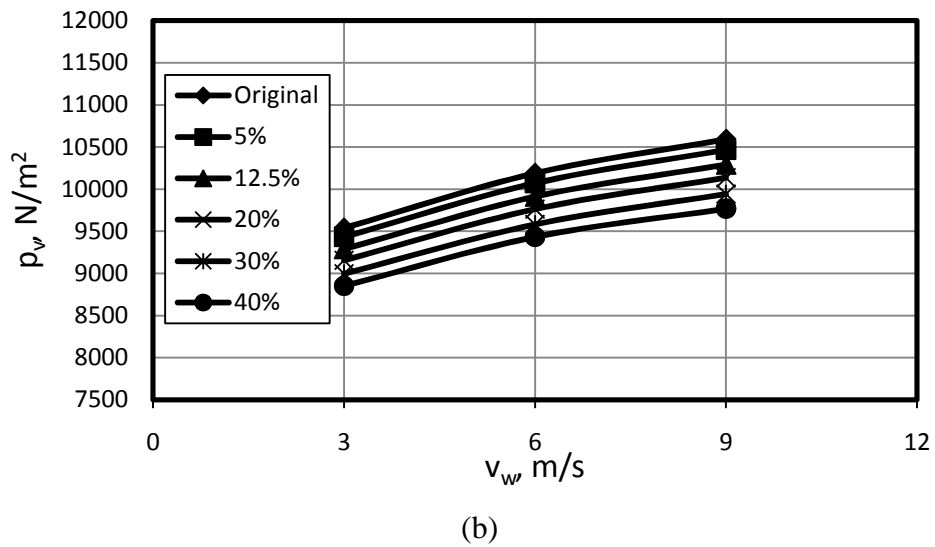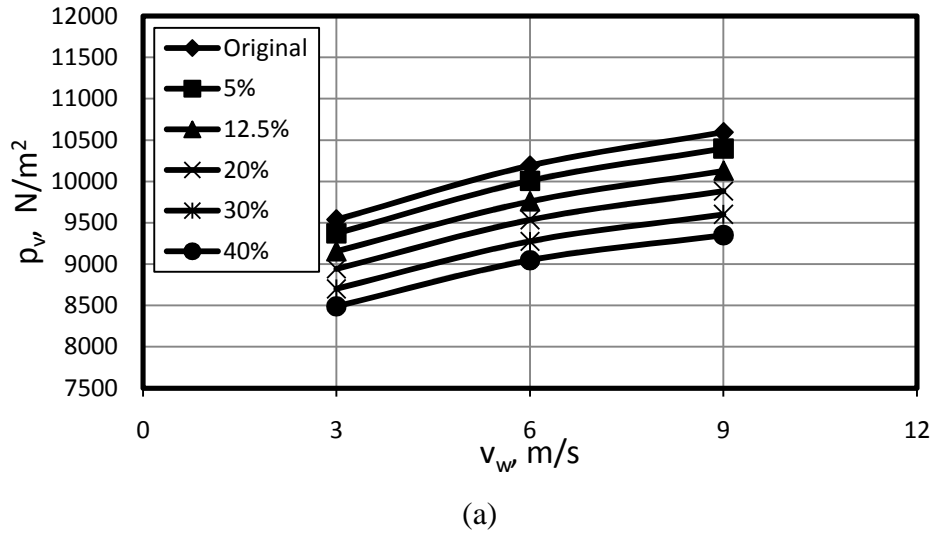
Figure 6.10:   Effect of increasing fan power on steam turbine backpressure under straight-flow wind conditions (a) All fans case, and (b) Periphery fans case
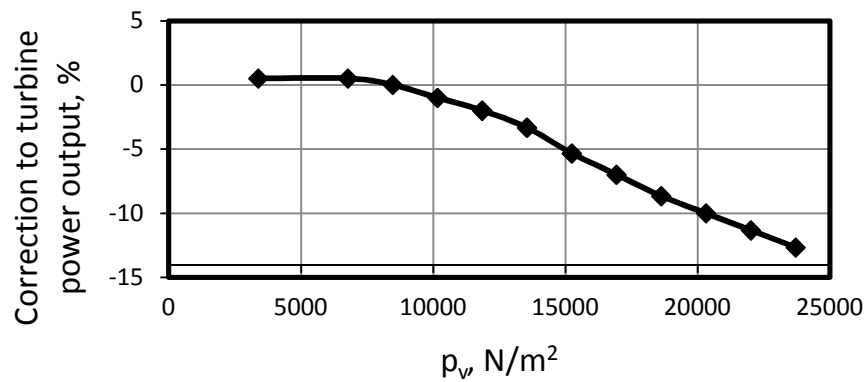
Figure 6.11:   Typical relationship between steam turbine power output and backpressure in a combined-cycle power plant with an ACSC

60

Using the gradient of the near linear portion of the curve illustrated in Figure 6.11, in the range $8500 \text{ N/m}^2 < p_v < 24000 \text{ N/m}^2$ it is possible to determine the percentage change in turbine output per unit backpressure change. The data presented in Figure 6.10 can now be used to determine the turbine output increase associated with increasing fan power.

The power required by the fan motors is calculated as illustrated in equation (6.5). It is assumed that the fan drive and gear box efficiencies are equal to unity.

$$P_F = \Delta p_{Fs} V_a / \eta_F \tag{6.5}$$

The net plant power output gain, ΔP_{net}, is calculated as shown in equation (6.6),

$$\Delta P_{net} = \frac{\left(P_{st(adj)} - P_{st(orig)}\right) - \left(\sum_{i=1}^{6}\sum_{j=1}^{5} P_{Fij(adj)} - \sum_{i=1}^{6}\sum_{j=1}^{5} P_{Fij(orig)}\right)}{P_{st(orig)}} \times 100\% \tag{6.6}$$

where $P_{st(orig)}$ and $P_{st(adj)}$ are the steam turbine outputs for the original case (no adjustment to fan power) and the increased fan power case respectively, while $P_{Fij(orig)}$ and $P_{Fij(adj)}$ are respectively the fan power consumptions of fan (i,j) for the original and increased fan power cases. The predicted net output gains are illustrated in Figure 6.12 for straight-flow wind conditions.

The results presented in Figure 6.12 indicate that at high wind speeds ($v_w \geq 6 \text{ m/s}$) increasing the power of all the fans by approximately 20% provides a maximised net turbine output. Increasing the fan power by more than 20% is not justifiable since the net output gain, although still positive, begins to diminish as a result of the large amount of power consumed by the fans. A fan power increase in the region of 20% should also be readily achievable without having to change the fan motors since most motors are designed with some reserve capacity. A maximum net plant power output increase of approximately 0.12% is predicted.
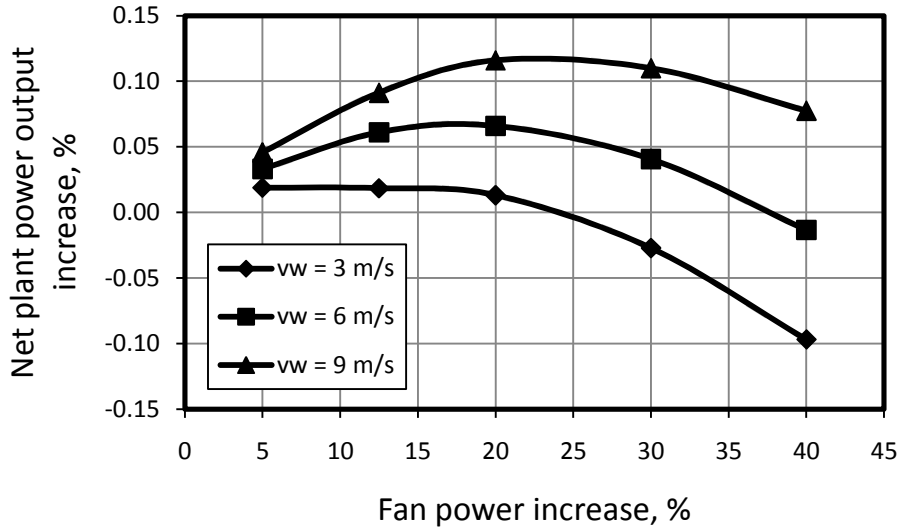
(a)
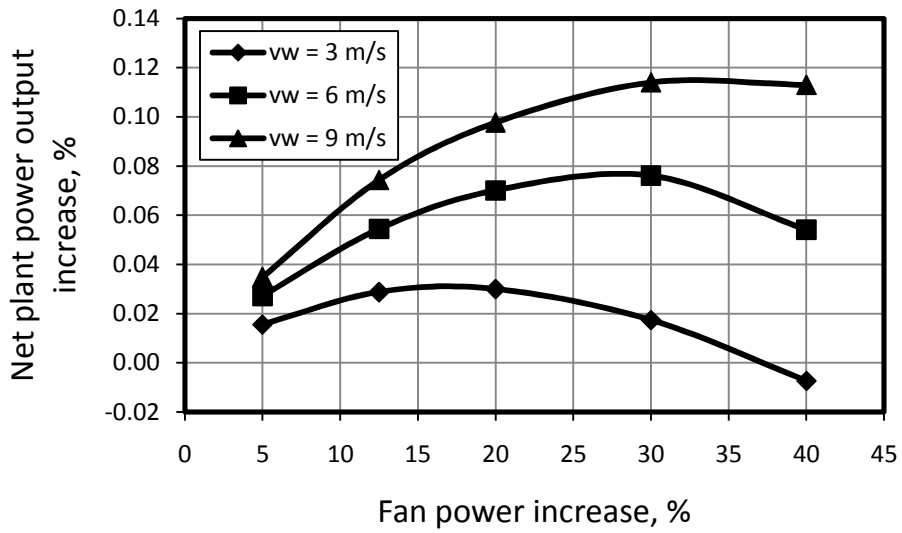
(b)

Figure 6.12: **Net plant output gain associated with increasing the power of (a) All fans, and (b) Periphery fans only**

7. Conclusion

The objective of this study was to develop an accurate and efficient way of modelling, and subsequently evaluating, ACSC performance using CFD. A suitable numerical model could then be used to evaluate the performance of a specific ACSC under windy conditions in an attempt to identify the causes of any wind induced heat transfer rate reductions. Finally, the model could be used to evaluate the effect of certain wind effect mitigation measures on ACSC performance.

7.1 The development of an accurate and efficient numerical ACSC model

In order to achieve these objectives an iterative two-step modelling approach was adopted whereby the numerical ACSC modelling was divided into global flow field and detailed ACSC modelling stages. This approach allows for larger ACSC installations to be modelled with relatively limited computational resources. Furthermore, the pressure jump fan model was used to further reduce the computational expense of the ACSC performance evaluation simulations.

A comparison of numerical results to test data was used to evaluate the accuracy of the numerical ACSC model developed in this study. The test data was collected during the full scale testing of El Dorado's ACSC carried out in September 2007. Good correlation was achieved between the numerical results and test data for a number of operating points. Discrepancies in the results, although small, can be attributed to instabilities in the ambient conditions over the test periods considered as well as numerical inaccuracies arising from the use of the pressure jump fan model, two step modelling approach, and other modelling assumptions. Nonetheless, the numerical model was able to predict the actual steam turbine backpressure to within a few percent of its measured value over each of the test periods (a 3.4% under prediction of the backpressure, corresponding to a $0.74°C$ discrepancy in the turbine exhaust temperature, being the greatest discrepancy).

The numerical results were also compared to the results presented by Van Rooyen (2008) as an additional model accuracy evaluation exercise. Van Rooyen (2008) investigated wind effects on fan performance in the generic ACSC considered in this study. A strong correlation

63

between the predicted fan performances in the two studies was achieved for most of the fans. However, discrepancies existed for the upstream fans. These discrepancies are thought to have three possible sources. Firstly, Van Rooyen (2008) uses the actuator disk fan model whereas this study employed the pressure jump method. Since the upstream fans are most severely impacted by inlet flow distortions caused by windy conditions, it is here that any inadequacies in the fan models will be most prevalent. It has been shown that the actuator disk model deviates from true fan behaviour under severely distorted inflow conditions (Thiart and von Backström, 1993) while the pressure jump method is said to provide limited accuracy under similar conditions (Van der Spuy et al., 2009). Neither fan model appears to be suited to modelling fan performance at the upstream fans and one model can therefore not be recommended above the other with confidence. The second cause of discrepancy between the results is that Van Rooyen (2008) used a two-step modelling approach without implementing an iterative procedure. This study found that at least a single global-to-detailed model iteration is necessary. Subsequent to the publication of his results, Van Rooyen applied the iterative solution procedure and predicted upstream fan performances that illustrate improved correlation with the results of this study. The third possible source of discrepancy is that Van Rooyen (2008) only modelled a single fan at a time in his detailed ACSC model. The influence of the remaining ACSC fans was accounted for using a uniform velocity inlet/outlet boundary similar to that used in the global-flow-field model. This study illustrated that the fan flow rates differ depending on the fan unit location in the ACSC. The effect of this flow rate maldistribution on the flow field in the vicinity, and subsequently the performance, of the fan under investigation is therefore not accounted for. Despite the discrepancies in the predicted performances of the upstream fans the overall heat transfer effectivenesses showed a strong correlation.

The strong correlation of the numerical results with previous numerical work and, more importantly, with test data instils confidence in the accuracy of the results and the suitability of the modelling method for use as an efficient ACSC performance evaluation tool.

7.2   ACSC performance under windy conditions

The results of an evaluation of El Dorado's ACSC under windy conditions identified reduced fan performance due to distorted flow at the fan inlets, particularly those in the windward fan rows, and hot plume recirculation as contributors to the reduction in ACSC heat transfer rate

associated with these conditions. These findings are consistent with literature relating to ACSC performance reductions under windy conditions (Duvenhage and Kröger, 1996).

It was further shown that reduced fan performance has a more significant impact on reduced ACSC heat transfer rates than plume recirculation at El Dorado. This finding is also supported by current literature (Maulbetsch, 2008). Despite this, many studies (Liu et al., 2009 for example) have focused on the mitigation of hot plume recirculation in an attempt to improve ACSC performance under windy conditions. It is clear from the findings of this study, however, that in this case greater ACSC performance enhancement potential lies in the mitigation of reduced fan performance under windy conditions. This topic therefore formed the focus of the wind effect mitigation measure evaluation portion of this study. It must however be stressed that the magnitude of the contribution of hot plume recirculation and reduced fan performance to the ACSC performance reduction under windy conditions will be influenced by the ACSC size, geometry and the wind direction.

It was also found that the presence of wind screens at El Dorado, while appearing to have a positive effect on the performance of the fans immediately upstream of the screen location, seemed to reduce the performance of the downstream fans. The identification of an optimum wind screen configuration that improves the performance of the upstream fans without being detrimental to the performance of the downstream fans was identified as a topic for further investigation.

7.3　Evaluation of wind mitigation measures

7.3.1　Wind screens

It was found that the installation of wind screens, in any configuration, was always beneficial to the performance of the fans upstream of the screen location but could be detrimental to the performance of the fans located downstream of the screen location. The magnitude of the upstream fan performance increase was sufficient that the net effect on ACSC heat transfer rate under windy conditions was positive for all screen configurations considered at El Dorado (relative to the case where no screens are present). It made sense, however, that some wind screen configuration must exist that provides the best overall performance. This would be achieved by a screen configuration that created a significant enough stagnation effect

under the ACSC fan platform to benefit the upstream fans measurably without providing too large an obstruction to the flow under the ACSC and effectively suffocating the downstream fans.

A screen configuration consisting of medium loss coefficient screens, $K_{sc} = 10$ in this case, installed to a height of $H_{sc}/H_i = 0.5$ was identified as an improved wind screen configuration for El Dorado. The screens provided a large enough obstruction to the flow under the ACSC to create a stagnation effect that benefited the upstream fans. On the other hand, the open space immediately below the fan platform and the use of a medium loss coefficient wind screen material allows for sufficient flow so as not to restrict the flow to the downstream fans.

This screen configuration is also attractive from an economic point of view. It requires no structural modification to the ACSC since the current wind screen location at El Dorado was not altered. Also, the new configuration requires less screen material than the current configuration and so future replacements of the screens will be cheaper. Finally, the new screen configuration is easier to maintain and clean since it doesn't extend to the full fan platform height.

7.3.2 Walkways

The installation of solid walkways along the ACSC periphery was shown to improve the performance of the edge fans, and subsequently the ACSC heat transfer rate, under windy conditions. It was also shown that increasing the width of the walkway has a positive influence on ACSC performance. The gain per unit walkway width increase, however, declines as the width increases. The selection of an appropriate walkway width depends on a combination of the ACSC geometry and prevailing wind conditions. The results of this study indicate the optimum walkway width increases with increasing wind speed and as such ACSCs operating in high wind regions would benefit from installing wider walkways. The installation of walkways is recommended for all ACSCs while the choice of walkway width should be based on an appropriate lifecycle cost analysis.

7.3.3 Increasing fan power

Increasing the fan power was investigated as a means of improving ACSC performance during windy periods by increasing the flow rate though the heat exchanger bundles. ACSC fans are typically installed with some reserve capacity over and above their rated power and so can be operated at higher powers safely without the need to install new, more powerful fan motors. At El Dorado, the problematic high prevailing wind speed period is also in summer. ACSC fans are typically specified based on a design air density associated with a specific design ambient temperature. In this case the design ambient temperature is lower than the average summer temperature and as such, according to the fan law presented in equation (6.1), the fan power in summer will be less than the design fan power. It follows that even more reserve power becomes available during the periods when it would be required most.

The results indicated that increasing the fan power by anything up to approximately 20% above rated can result in net plant power output gains, relative to the design fan power case, under windy conditions. The output gains are, however, predicted to be very small and this method is therefore not recommended for existing ACSCs with fixed speed fan motors already installed. The installation of variable speed motors on new ACSC installations may be justifiable in some cases.

It must be noted however that a number of approximations were made in this analysis and that the true value, or lack thereof, of this wind effect mitigation strategy should be evaluated with accurate steam turbine data for a specific ACSC installation.

7.4   Importance of this study

Due to their scale, ACSCs are difficult and expensive to investigate experimentally. Furthermore, due to the dynamic relationship between ACSC performance and ambient conditions, analytical investigations are able to provide only limited accuracy. The numerical ACSC modelling method developed in this study allows for the accurate and efficient evaluation of ACSC performance under a variety of ambient conditions.

This modelling method has the potential to allow for the relatively quick and easy evaluation of novel means of mitigating the negative impact of certain ambient conditions (wind in this

study) on ACSC performance. Due to the relative ease with which models can be generated, engineers have the freedom to investigate a larger variety of possible performance enhancing strategies than with traditional build-and-test methods (Kelecy, 2000). This fact, coupled with the fact that the consequences of a failed attempt at identifying a successful performance enhancing measure are negligible, means that engineers are able to experiment in a creative and innovative manner. The potential for identifying novel and attractive ways of enhancing ACSC performance under certain ambient conditions is therefore increased.

References

Air-Cooled Condenser Design, Specification, and Operation Guidelines. EPRI, Palo Alto, CA: 2005, 1007688.

Barker, B., *Running Dry at the Power Plant*, EPRI Summer Journal, pp 26 – 35, 2007.

Bredell, J., *Numerical Investigation of Fan Performance in a Forced Draft Air-cooled Steam Condenser*, MScEng Thesis, Department of Mechanical Engineering, University of Stellenbosch, 2005.

Bredell, J.R., Kröger, D.G., Thiart, G.D., *Numerical investigation of fan performance in a forced draft air-cooled steam condenser*, Applied Thermal Engineering, Vol. 26, pp 846 – 852, 2006.

British Standards Institution, *Fans for General Purposes, Part 1, Methods for Testing Performance*, BS 848, 1997.

Carney, B., Feeley, T.J., McNemar, A., *NETL Power Plant Water Research Program*, US Department of Energy, Presentation: EPRI workshop on Advanced Thermoelectric Cooling Technologies, Charlotte, 2008.

Comparison of Alternate Cooling Technologies for U. S. Power Plants: Economic, Environmental, and Other Tradeoffs, EPRI, Palo Alto, CA: 2004. 1005358.

DiFilippo M., *Reclaiming Water for Cooling at SCE's Mountainview Power Plant*, Presentation: EPRI workshop on Advanced Thermoelectric Cooling Technologies, Charlotte, 2008.

Duvenhage, K., Kröger, D.G., *The influence of wind on the performance of forced draft air-cooled heat exchangers*, Journal of Wind Engineering and Industrial Aerodynamics, Vol. 62, pp 259 - 277, 1996.

Duvenhage, K., Vermeulen, J.A., Meyer, C.J., Kröger, D.G., *Flow distortions at the fan inlet of forced-draft air-cooled heat exchangers*, Applied Thermal Engineering, Vol. 16, pp 741 – 752, 1996.

FLUENT 6.3 User's Guide, Fluent Inc., Lebanon, 2006.

Gadhamshetty, V., Nirmalakhandan, N., Myint, M., Ricketts, C., *Improving Air-cooled Condenser Performance in Combined Cycle Power Plants*, Journal of Energy Engineering, Vol. 132, No. 2, pp 81 – 88, 2006.

Hassani, V., Dickens, J., Bell, K., *The Fin-on-plate Heat Exchanger: A New Configuration for Air-cooled Power Plants*, Transactions – Geothermal Resources Council, Vol. 27, pp 583 – 586, 2003.

Hightower, M., *Energy and Water: Issues, Trends and Challenges*, Sandia National Laboratories, Presentation: EPRI workshop on Advanced Thermoelectric Cooling Technologies, Charlotte, 2008.

Hotchkiss, P.J., Meyer, C.J., von Backström, T.W., *Numerical investigation into the effect of cross-flow on the performance of axial flow fans in forced draft air-cooled heat exchangers*, Applied Thermal Engineering, Vol. 26, pp 200 – 208, 2006.

Kelecy, F., *Study demonstrates that simulation can accurately predict fan performance*, Journal Articles by FLUENT Software Users, JA108, 2000.

Kröger, D.G., *Air-cooled heat exchangers and cooling towers*, Penwell Corp., Tulsa, OK., 2004.

Launder, B.E., Spalding, D.B., *The numerical computation of turbulent flows*, Computer Methods in Applied Mechanics and Engineering, Vol. 3, Issue 2, pp 269 – 289, 1974.

Liu, P., Duan, H., Zhao, W., *Numerical investigation of hot air recirculation of air-cooled condensers at a large power plant*, Applied Thermal Engineering, Vol. 29, pp 1927 – 1934, 2009.

Maulbetsch, J., *Cooling Systems: Some things that might work*, Presentation: EPRI workshop on Advanced Thermoelectric Cooling Technologies, Charlotte, 2008.

Maulbetsch, J.S., DiFilippo, M.N., *Effects of wind on air-cooled condenser performance*, Cooling Technology Institute, Paper no. TP07-04, 2007.

McGowan, C., Zammit, K., Maulbetsch, J., *Field Testing of Wind Effects on Air-cooled Condensers*, Presentation: EPRI workshop on Advanced Thermoelectric Cooling Technologies, Charlotte, 2008.

Meyer, C.J., Kröger, D.G., *Numerical investigation of the effect of fan performance on forced draft air-cooled heat exchanger plenum chamber aerodynamic behaviour*, Applied Thermal Engineering, Vol. 24, pp 359 – 371, 2004.

Meyer, C.J., *Numerical investigation of the effect of inflow distortions on forced draft air-cooled heat exchanger performance*, Applied Thermal Engineering, Vol. 25, pp 1634 – 1649, 2005.

Mills, W., *Potential Impacts of Climate Change on Water Resources, and Implications for Power Plant Operations*, Presentation: EPRI workshop on Advanced Thermoelectric Cooling Technologies, Charlotte, 2008.

Owen, M.T.F., *Performance evaluation of an air-cooled steam condenser*, BEng Thesis, Department of Mechanical Engineering, University of Stellenbosch, 2007.

Patankar, S.V., *Numerical heat transfer*, McGraw-Hill, New York, 1980.

Salta, C.A., Kröger, D.G., *Effect of inlet flow distortions on fan performance in forced draft air-cooled heat exchangers*, Heat Recovery Systems and CHP, Vol. 15, No. 6, pp 555 – 561, 1995.

Shih, T., Liou, W., Shabbir, A., Yang, Z., Zhu, J., *A new k-ε eddy viscosity model for high Reynolds number turbulent flows*, Computers Fluids, Vol. 24, No. 3, pp 227 – 238, 1995.

Stinnes, W.H., von Backström, T.W., *Effect of cross-flow on the performance of air-cooled heat exchanger fans*, Applied Thermal Engineering, Vol. 22, pp 1403 – 1415, 2002.

Thiart, G.D., von Backström, T.W., *Numerical simulation of the flow field near an axial flow fan operating under distorted inflow conditions*, Journal of Wind Engineering and Industrial Aerodynamics, Vol. 45, pp 189 – 214, 1993.

Turnage, J., *Water Scarcity and Power Generation: A Perspective on a Societal Issue*, UniStar Nuclear, Presentation: EPRI workshop on Advanced Thermoelectric Cooling Technologies, Charlotte, 2008.

Van Aarde, D.J. and Kröger, D.G., *Vloeiverliese deur `n A-Raam Vinbuisbundel in `n Lugverkoelde Kondensator*, MScEng Thesis, Department of Mechanical Engineering, University of Stellenbosch, 1990.

Van der Spuy, S.J., von Backström, T.W., Kröger, D.G., *Performance of low noise fans in power plant air-cooled steam condensers*, Noise Control Engineering, J.57(4), July – August, 2009.

Van Rooyen, J.A., Kröger, D.G., *Performance trends of an air-cooled steam condenser under windy conditions*, Journal of Engineering for Gas Turbines and Power, Vol. 130, March 2008.

Versteeg, H.K., Malalasekera, W., *An introduction to computational fluid dynamics: The finite volume method*, Pearson Education Limited, Second edition, 2007.

Wurtz, W., Nagel, P., *Air cooled condensers: Application and innovative designs for today's power plants*, Power-gen International, Orlando, Florida, 2006.

Appendix A - System specifications

A.1 Finned tube heat exchanger

The geometric, heat transfer and flow resistance specifications of the finned tube bundles used in the finned tube heat exchangers for the generic ACSC are listed here.

Table A.1: Finned tube heat exchanger specifications (generic ACSC)

Description	Symbol	Value	Units
Number of heat exchanger bundles above one fan	n_b	8	
Effective frontal area of one bundle	A_{fr}	27.434	m^2
Finned tube length	L_t	9.55	m
Tube hydraulic diameter	d_h	0.02975	m
Inside area of tube per unit length	A_{ti}	0.21341	m
Inside cross sectional tube area	A_{ts}	0.00159	m^2
Inside tube height	H_t	0.097	m
Inside tube width	W_t	0.017	m
Number of finned tube rows	n_r	2	
Number of finned tubes per bundle in the first row	n_{tb1}	57	
Number of finned tubes per bundle in the second row	n_{tb2}	58	
Number of vapor passes	n_{vp}	1	
Heat exchanger half apex angle	θ	28	°
Ratio of minimum to free stream flow area through the finned tube bundle	σ	0.41	
Ratio of minimum to free stream flow area at the inlet of finned tube bundle	σ_{21}	0.86	

The characteristic heat transfer parameters through the first and second tube rows at the generic ACSC are described by equations (A.1) and (A.2) respectively, while the heat

73

exchanger loss coefficient under normal isothermal flow conditions is described by equation (A.3).

$$Ny_{1(Gen)} = 366.007945Ry^{0.433256} \tag{A.1}$$

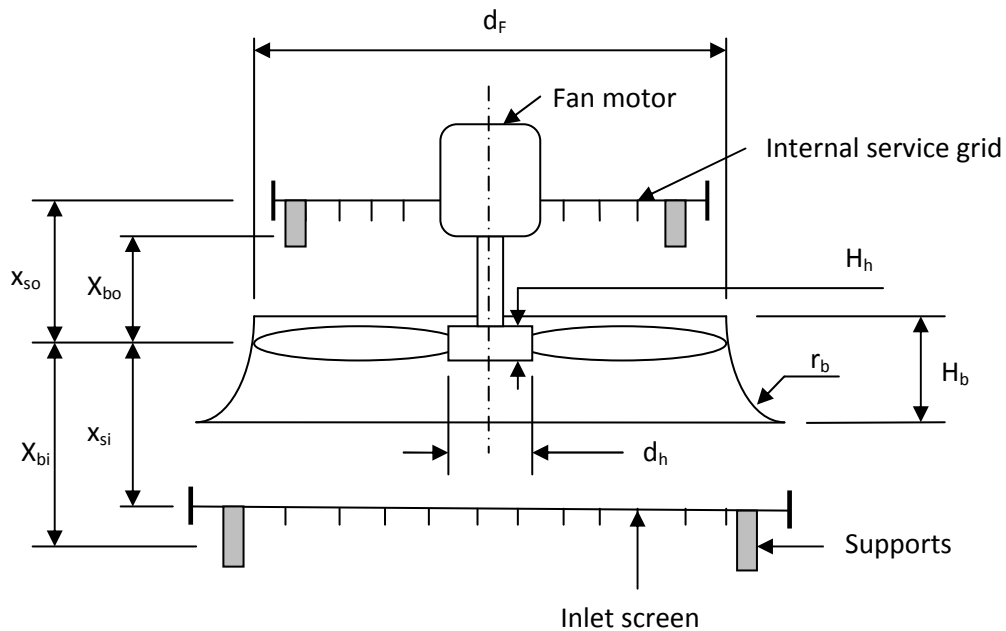$$Ny_{2(Gen)} = 360.588007Ry^{0.470373} \tag{A.2}$$

$$K_{he(Gen)} = 4464.831Ry^{-0.43927} \tag{A.3}$$

In equations (A.1) - (A.3),

$$Ry = m_a / \mu_a n_b A_{fr} \tag{A.4}$$

A.2   Axial flow fan

The supplier fan specifications are detailed in this section. Figure A.1 illustrates the fan dimensions for reference purposes.

Figure A.1:   **Fan dimensions**

74

Table A.2: Axial flow fan specifications (generic ACSC)

| Description	Symbol	Value	Units
Fan diameter	d_F	9.145	m
Fan casing diameter	d_c	9.17	m
Hub/tip ratio	d_h/d_F	0.4	
Ratio of hub height to fan diameter	H_h/d_F	0.1	
Height of inlet shroud	H_b	1.92	m
Inlet shroud radius	r_b	1.16	m
Number of blades	N_{bl}	8	
Blade angle	ψ	34.5	°
Rotational speed	N	125	rpm
Inlet screen distance from fan blade (upstream)	x_{si}	1.3	m
Support beam distance from fan blade (upstream)	x_{bi}	1.34	m
Support beam distance from fan blade (downstream)	x_{bo}	0.53	m
Walkway distance from fan blade (downstream)	x_{so}	1	m
Ratio of inlet screen area to fan casing area	σ_{si}	0.125	
Ratio of support beam area to fan casing area (upstream)	σ_{bi}	0.15	
Ratio of support beam area to fan casing area (downstream)	σ_{bo}	0.05	
Ratio of walkway area to fan casing area	σ_{so}	0.1	

The fan static pressure characteristic for the generic ACSC fans is illustrated in equation (A.5).

$$\Delta p_{Fs(Gen)} = 320.0452 - 0.2975 V_a + 6.3515 \times 10^{-4} V_a^2 - 8.14 \times 10^{-7} V_a^3 , N/m^2 \tag{A.5}$$

Appendix B - Supplementary results

B.1 A-frame vs. simple heat exchanger model

The effect of modelling the detailed A-frame heat exchanger, as opposed to using a simplified model, on the predicted performance of the fans in the numerical ACSC model is investigated in this document. Figure 3.7 illustrates the difference between the two heat exchanger models. A comparison of the volumetric effectivenesses predicted for three fans, using the two heat exchanger models, is illustrated in Figure B.1.
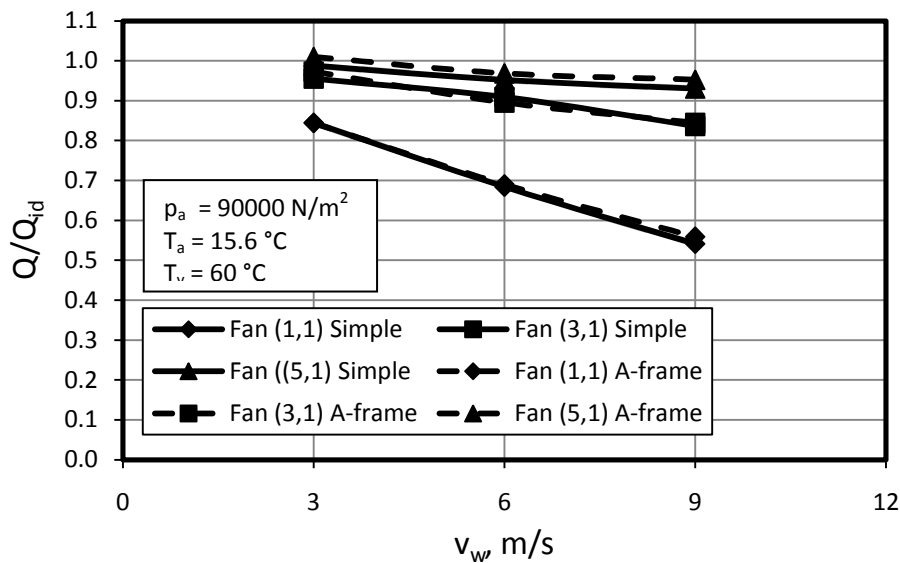

Figure B.1: **Comparison of fan volumetric effectivenesses using the A-frame and simplified heat exchanger models**

The fan volumetric effectivenesses predicted using the A-frame model are very similar to those predicted using the simplified heat exchanger model. Although slight discrepancies do exist, they are not of sufficient magnitude to warrant the additional complications and computational expense associated with modelling the A-frame instead of using the simplified heat exchanger model.

B.2   Verification of pressure jump fan and heat exchanger models

The accuracy of the pressure jump fan model and simplified heat exchanger model is verified through a comparison of the numerically predicted fan operating point under ideal flow conditions (using the model described in Section 3.2.3) to the theoretically determined operating point. The theoretical operating point is defined by the point of intersection of the effective system resistance curve, given in equation (3.16), and the fan performance curve, described by equations (A.8) and (A.9) for El Dorado and the generic ACSC respectively.

The determination of the theoretical operating point is illustrated in Figure B.2 for the generic ACSC system. Table B.1 lists the theoretical and numerically predicted operating points for both El Dorado and the generic system. A good correlation exists between the theoretical and numerical values indicating that the pressure jump fan model and simplified heat exchanger model are operating as desired.
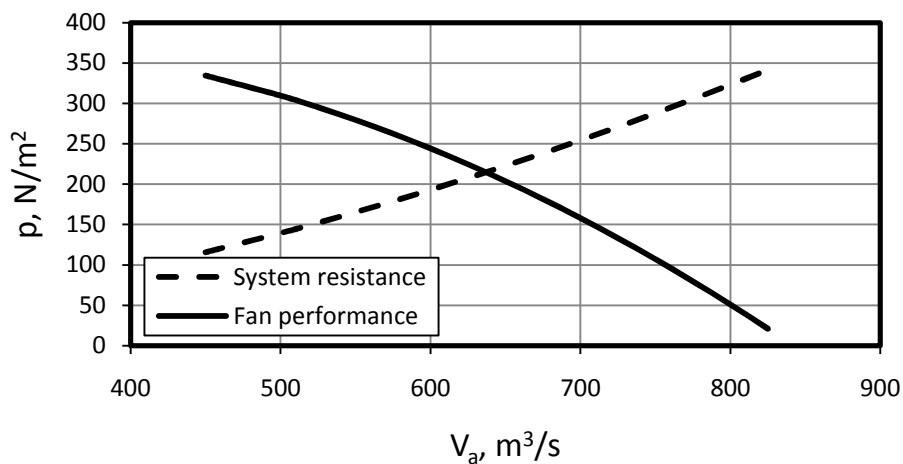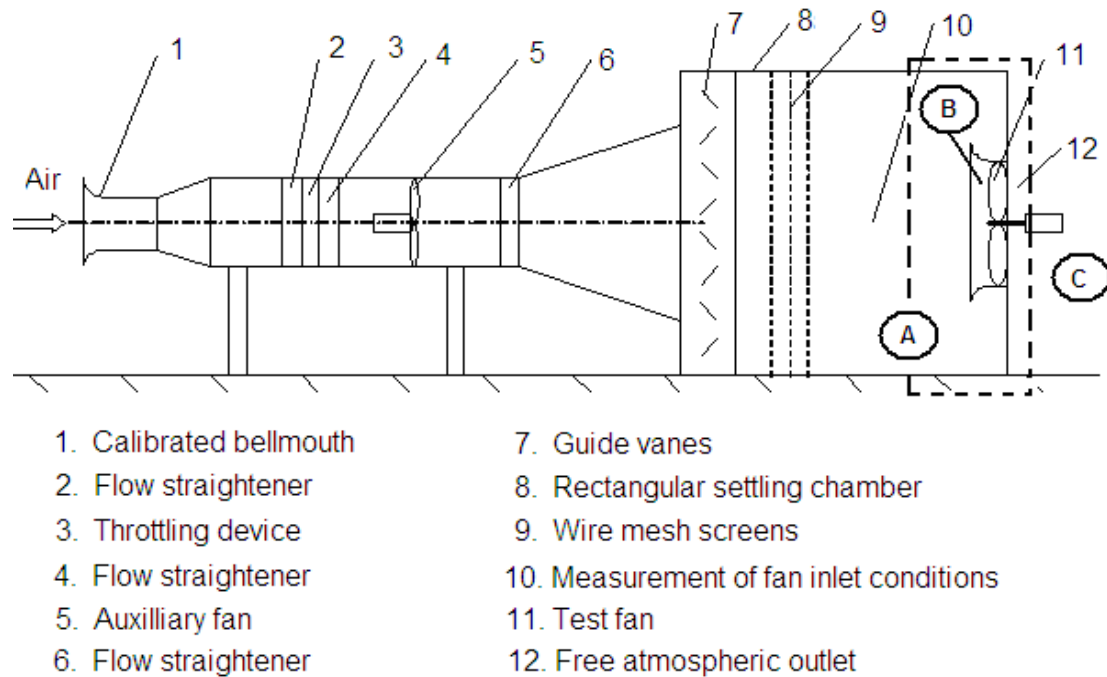

Figure B.2:   **Theoretical determination of the fan operating point under ideal operating conditions**

Table B.1:   **Comparison of theoretical and numerically determined operating points under ideal operating conditions**

	Theoretical operating point, m^3/s	Numerically determined operating point, m^3/s
El Dorado ($\rho_a = 1.128\ kg/m^3$)	595	600.177
Generic ACSC	636	637.565

Appendix C - Derivation of the fan performance characteristic for the pressure jump fan model

When fans are tested to determine their performance characteristics; a free inlet, free outlet (or type A) setup is typically used (Kröger, 2004). Figure C.1 shows a BS848 (British Standards, 1997) Type A fan test facility.

1. Calibrated bellmouth
2. Flow straightener
3. Throttling device
4. Flow straightener
5. Auxilliary fan
6. Flow straightener
7. Guide vanes
8. Rectangular settling chamber
9. Wire mesh screens
10. Measurement of fan inlet conditions
11. Test fan
12. Free atmospheric outlet

Figure C.1:   BS848 Type A fan test facility schematic (courtesy Bredell, 2005)

In this type of test setup, the static pressure difference is measured between the settling chamber at (A), and the atmosphere at (C). The magnitude of this pressure difference at different flow rates is given as the fan static pressure characteristic, Δp_{Fs}. Since the flow in the settling chamber is essentially stagnant, the fan static pressure characteristic actually describes the total-to-static pressure rise across the fan.

The pressure jump fan model requires a function describing the static-to-static pressure rise across the fan i.e. the static-to-static pressure rise between (B) and (C) in Figure C.1. The required function is derived as shown hereafter.

$$\Delta p_{Fs} = p_{sC} - p_{tA} \tag{C.1}$$

In equation (C.1) the subscripts s and t stand for static and total respectively. Ignoring the small pressure loss in the settling chamber,

$$p_{tA} = p_{tB} = p_{sB} + \rho_a v_a^2 / 2 \tag{C.2}$$

where v_a is the velocity through the fan based on the effective fan area A_e as described in equation (2.6).

Substituting equation (C.2) into (C.1) and rearranging yields the desired static-to-static pressure rise function, Δp_F.

$$\Delta p_F = p_{sC} - p_{sB} = p_{sC} - p_{tA} + \rho_a v_a^2 / 2 = \Delta p_{Fs} + \rho_a v_a^2 / 2 \tag{C.3}$$

Therefore, for the purpose of the pressure jump fan model, the fan static pressure characteristics given in equations (A.8) and (A.9) need to be modified through the addition of a dynamic pressure term.

Appendix D - System loss coefficients

D.1   Definition of losses in an ACSC system

Kröger (2004) derives equations for the major losses in an ACSC system based on extensive experimental and theoretical research. A description of the system losses is given here along with their appropriate equations.

The effective system loss for the entire ACSC is defined in terms of the draft equation, which is repeated here for convenience.

$$\Delta p_e = -\left[\frac{K_{ts}}{2\rho_{a56}} \left(\frac{m_a}{n_b A_{fr}} \right)^2 + \frac{K_{up}}{2\rho_{a3}} \left(\frac{m_a}{A_e} \right)^2 + \frac{K_{do}}{2\rho_{a3}} \left(\frac{m_a}{A_e} \right)^2 + \frac{K_{\theta t}}{2\rho_{a56}} \left(\frac{m_a}{n_b A_{fr}} \right)^2 \right] \tag{D.1}$$

K_{ts} accounts for loss due to the fan platform supports while K_{up} and K_{do} represent the losses due to obstacles upstream and downstream of the fan respectively. The primary contributors to the upstream losses are the fan inlet screen and its supports, while the primary downstream obstacles are the fan drive system and the walkway. Kröger (2004) gives empirical relations for K_{up} and K_{do} in terms of the projected area of the obstacle and its distance from the fan.

$K_{\theta t}$ is the total loss across the heat exchanger bundle and includes the kinetic energy losses at the heat exchanger outlet. The equation for this loss coefficient under isothermal flow conditions is given in equation (D.2).

$$K_{\theta t} = K_{he} + \left(\frac{1}{\sin \theta_m} - 1 \right) \left(\frac{1}{\sin \theta_m} - 1 + 2\sqrt{K_{ci}} \right) + K_{dj} + K_o \tag{D.2}$$

K_{he} is the heat exchanger loss coefficient for normal isothermal flow as described by equations (A.3) and (A.6) for El Dorado and the generic ACSC respectively. θ_m is the actual mean flow incidence angle at the heat exchanger inlet and is a function of the A-frame half apex angle θ.

$$\theta_m = 0.0019\theta^2 + 0.9133\theta - 3.1558 \tag{D.3}$$

K_{ci} is the heat exchanger entrance contraction loss coefficient for normal flow and is based on the normal approach free stream velocity. This loss coefficient is ultimately a function of the ratio of the minimum to free stream flow area through the heat exchanger bundle, σ, and the ratio of the minimum to free stream flow area at the bundle inlet, σ_{21}, as shown in equations (D.4) and (D.5).
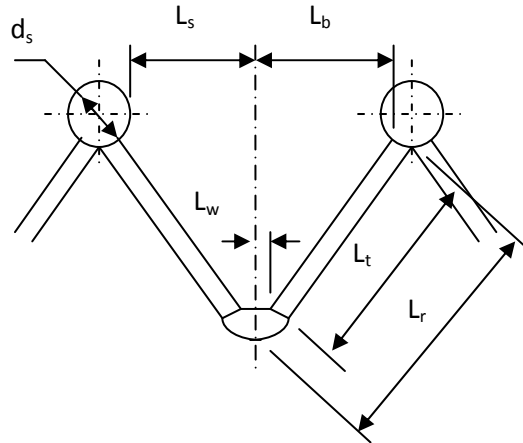
$$\begin{aligned}\sigma_c &= 0.6155417 + 0.04566493\,\sigma_{21} - 0.336651\sigma_{21}^2 + 0.4082743\,\sigma_{21}^3 \\ &\quad + 2.672041\sigma_{21}^4 - 5.963169\,\sigma_{21}^5 + 3.558944\,\sigma_{21}^6\end{aligned} \tag{D.4}$$

$$K_{ci} = \left(\frac{1 - 1/\sigma_c}{\sigma}\right)^2 \tag{D.5}$$

The kinetic energy loss at the heat exchanger outlet as a result of turbulent decay of the "jet" of air leaving the heat exchanger bundles is referred to as the jetting loss, K_{dj}, and is given by equation (D.6). The heat exchanger outlet loss, K_o, due to the final mixing process that is responsible for smoothing the outlet velocity profile is given by equation (D.7). Figure D.1 illustrates the dimensions used in equations (D.6) and (D.7).

$$K_{dj} = \left[\begin{array}{l}\left\{-2.89188\left(\dfrac{L_w}{L_t}\right) + 2.93291\left(\dfrac{L_w}{L_t}\right)^2\right\}\left(\dfrac{L_t}{L_s}\right)\left(\dfrac{L_b}{L_s}\right)\left(\dfrac{28}{\theta}\right)^{0.4}\right]^2 \\[2em] + \left\{\left(\dfrac{L_s}{L_b}\right)e^{2.36987 + 5.8601\times10^{-2}\theta - 3.3797\times10^{-3}\theta^2}\right\}^{0.5}\left(\dfrac{L_t}{L_r}\right)\end{array}\right]^2 \tag{D.6}$$

$$K_o = \left[\begin{array}{l}\left\{-2.89188\left(\dfrac{L_w}{L_t}\right) + 2.93291\left(\dfrac{L_w}{L_t}\right)^2\right\}\left(\dfrac{L_s}{L_b}\right)^3 + 1.9874 \\[2em] -3.02783\left(\dfrac{d_s}{2L_b}\right) + 2.0187\left(\dfrac{d_s}{2L_b}\right)^2\end{array}\right]\left(\dfrac{L_t}{L_s}\right)^2 \tag{D.7}$$

Figure D.1:   Section of an array of A-frames illustrating relevant dimensions

D.2   Evaluation of loss coefficients for the generic ACSC

Based on the empirical relations presented by Kröger (2004),

$$K_{ts} = 1.6$$

$$K_{up} = 0.28$$

$$K_{do} = 0.35$$

Substituting $\sigma = 0.41$ and $\sigma_{21} = 0.86$ in equations (D.4) and (D.5) yields,

$$\sigma_c = 0.6155417 + 0.04566493(0.86) - 0.336651(0.86)^2 + 0.4082743(0.86)^3$$
$$+ 2.672041(0.86)^4 - 5.963169(0.86)^5 + 3.558944(0.86)^6 = 0.761$$

$$K_{ci} = \left(\frac{1 - 1/0.761}{0.41}\right)^2 = 0.587$$

Furthermore, with $\theta = 28°$, $L_t = 9.55\ m$, $L_w = 0.397\ m$, $L_s = 4.102\ m$, $L_b = 4.924\ m$, $L_r = 10.6$ m and $d_s = 2.34\ m$, find according to equations (D.6) and (D.7),

82

$$K_{dj} = \left[\begin{array}{c} \left\{-2.89188\left(\dfrac{0.397}{9.55}\right) + 2.93291\left(\dfrac{0.397}{9.55}\right)^2\right\}\left(\dfrac{9.55}{4.102}\right)\left(\dfrac{4.924}{4.102}\right)\left(\dfrac{28}{28}\right)^{0.4} \\[2mm] + \left\{\left(\dfrac{4.102}{4.924}\right)e^{2.36987 + 5.8601\times10^{-2}(28) - 3.3797\times10^{-3}(28)^2}\right\}^{0.5}\left(\dfrac{9.55}{10.6}\right) \end{array}\right]^2 = 1.696$$

$$K_{o} = \left[\begin{array}{c} \left\{-2.89188\left(\dfrac{0.397}{9.55}\right) + 2.93291\left(\dfrac{0.397}{9.55}\right)^2\right\}\left(\dfrac{4.102}{4.924}\right)^3 + 1.9874 \\[2mm] -3.02783\left(\dfrac{2.34}{2\cdot4.924}\right) + 2.0187\left(\dfrac{2.34}{2\cdot4.924}\right)^2 \end{array}\right]\left(\dfrac{9.55}{4.102}\right)^2 = 7.129$$

From equation (D.3) find,

$$\theta_m = 0.0019(28)^2 + 0.9133(28) - 3.1558 = 23.91°$$

Substitution of equation (A.4) into equation (A.3), and considering for this case an ambient temperature of $T_a = 15.6\ °C$, yields,

$$K_{he} = 4464.831\left(\dfrac{m_a}{1.849\times10^{-5}\cdot8\cdot27.434}\right)^{-0.43927} = 397.3837\,m_a^{-0.43927}$$

The resulting total loss over the heat exchanger can now be calculated according to equation (D.2).

$$K_{\theta t} = 397.3837 m_a^{-0.43927} + \left(\dfrac{1}{\sin23.91°} - 1\right)\left(\dfrac{1}{\sin23.91°} - 1 + 2\sqrt{0.587}\right) + 1.696 + 7.129$$

$$= 397.3837 m_a^{-0.43927} + 13.232$$

Substituting the loss coefficients determined above into equation (D.1) yields,

$$\Delta p_e = -\left[\begin{array}{l} \dfrac{1.6033}{2\cdot 1.085}\left(\dfrac{m_a}{8\cdot 27.434}\right)^2 + \dfrac{0.28}{2\cdot 1.085}\left(\dfrac{m_a}{82.245}\right)^2 + \dfrac{0.35}{2\cdot 1.085}\left(\dfrac{m_a}{82.245}\right)^2 \\[2mm] + \dfrac{397.3837 m_a^{-0.43927} + 13.232}{2\cdot 1.085}\left(\dfrac{m_a}{8\cdot 27.434}\right)^2 \end{array}\right]$$

$$= -\left(2.1029\times 10^{-4} m_a^2 + 3.8018\times 10^{-3} m_a^{1.680601}\right)$$

Since volumetric flow rate is related to mass flow rate as shown in equation (D.8), it is possible to write the effective system resistance as a function of volumetric flow rate, as shown in equation (D.9).

$$V_a = m_a / \rho_a \tag{D.8}$$

$$\Delta p_e = -\left(2.4756\times 10^{-4} V_a^2 + 4.3181\times 10^{-3} V_a^{1.56073}\right) \tag{D.9}$$

Appendix E - Derivation of the viscous and inertial loss coefficients

Viscous and inertial loss coefficients are used in the heat exchanger model to account for the effective resistance of the ACSC system to flow, as described in Section 3.2.2.2. The derivation of these loss coefficients for the generic ACSC is illustrated here.

For the rectangular heat exchanger model, as shown in Figure 3.5, equation (E.1) holds.

$$V_a = |w|(L_x \times L_y) \tag{E.1}$$

Equation (D.9) can be approximated by a second order polynomial as shown in equation (E.2).

$$\begin{aligned} \Delta p_e &= -\left(2.4756 \times 10^{-4} V_a^2 + 4.3181 \times 10^{-3} V_a^{1.56073}\right) \\ &\approx -\left(4.132315 \times 10^{-4} V_a^2 + 5.6295 \times 10^{-2} V_a\right) \end{aligned} \tag{E.2}$$

Substitution of equation (E.1) into equation (E.2), with $L_x = 11.8\ m$ and $L_y = 10.56\ m$ (see Table 3.4), results in an expression for the effective system resistance in terms of the air velocity through the heat exchanger.

$$\begin{aligned} \Delta p_e &= -\left(4.132315 \times 10^{-4} V_a^2 + 5.6295 \times 10^{-2} V_a\right) \\ &= 4.132315 \times 10^{-4} (L_x \times L_y)^2 |w|w + 5.6295 \times 10^{-2} (L_x \times L_y)w \\ &= 6.4163|w|w + 7.1048w \end{aligned} \tag{E.3}$$

The body force acting in the z-direction of each cell in the heat exchanger model is given by equation (E.4) for $L_z = 0.2\ m$.

$$F_z = \Delta p_e / L_z = 32.082|w|w + 35.075w \tag{E.4}$$

The body force in the z-direction is defined by Bredell (2005) as shown in equation (E.5).

$$F_z = C_z \frac{1}{2} \rho_a |\vec{v}| w + \frac{\mu_a}{\alpha_z} w \tag{E.5}$$

Since the flow is restricted to the z-direction in the heat exchanger model, $|\vec{v}| = |w|$ in equation (E.5). The viscous and inertial loss coefficients, C_z and $1/\alpha_z$ respectively, can now be determined by comparing equations (E.4) and (E.5).

$$C_z = 59.1634 \, m^{-1}$$

And,

$$1/\alpha_z = 1.897 \times 10^6 \, m^{-2}$$

Appendix F - Derivation of the heat exchanger energy source term

The derivation of the source term added to the energy equation of the flow through the heat exchanger to account for the heat transfer between the process steam and the ambient air is described here.

The heat transfer in the first tube row is given by,

$$Q_1 = m_a c_{pa} \left(T_{ao1} - T_{ai1} \right) = e_1 m_a c_{pa} \left(T_v - T_{ai1} \right) \tag{F.1}$$

Equation (F.1) can be rearranged to yield an expression for the air temperature immediately after the first tube row.

$$T_{ao1} = e_1 T_v + \left(1 - e_1 \right) T_{ai1} \tag{F.2}$$

Similarly, for the second tube row,

$$Q_2 = m_a c_{pa} \left(T_{ao2} - T_{ao1} \right) = e_2 m_a c_{pa} \left(T_v - T_{ao1} \right) \tag{F.3}$$

and,

$$T_{ao2} = e_2 T_v + \left(1 - e_2 \right) T_{ao1} \tag{F.4}$$

Substitution of equation (F.2) into (F.4) results in an expression for the air temperature at the heat exchanger exit in terms of the steam, and heat exchanger air inlet, temperatures.

$$T_{ao2} = e_2 T_v + \left(1 - e_2 \right) \left[e_1 T_v + \left(1 - e_1 \right) T_{ai1} \right] \tag{F.5}$$

The total heat transfer through the heat exchanger is,

$$Q = Q_1 + Q_2 = m_a c_{pa} \left(T_{ao2} - T_{ai1} \right) \tag{F.6}$$

The energy source term to be added to the flow as it passes through the numerical heat exchanger model is defined as,

$$S_E = \delta Q / \delta V \tag{F.7}$$

Substitution of equation (F.6) into equation (F.7) yields,

$$S_E = \frac{\delta m_a}{\delta V} c_{pa} \left(T_{ao2} - T_{ai1} \right) = \frac{\rho_a |w|}{L_z} c_{pa} \left(T_{ao2} - T_{ai1} \right) \tag{F.8}$$

Appendix G - Test operating periods

The four periods selected from the test data, collected during the full scale testing of El Dorado's ACSC (Owen, 2007), for comparison with numerical results are described in detail here. The parameters extracted from the data for use in the numerical simulations are listed in Table 4.2. A diagram illustrating the layout of El Dorado's ACSC is presented in Figure G.1 for reference purposes.
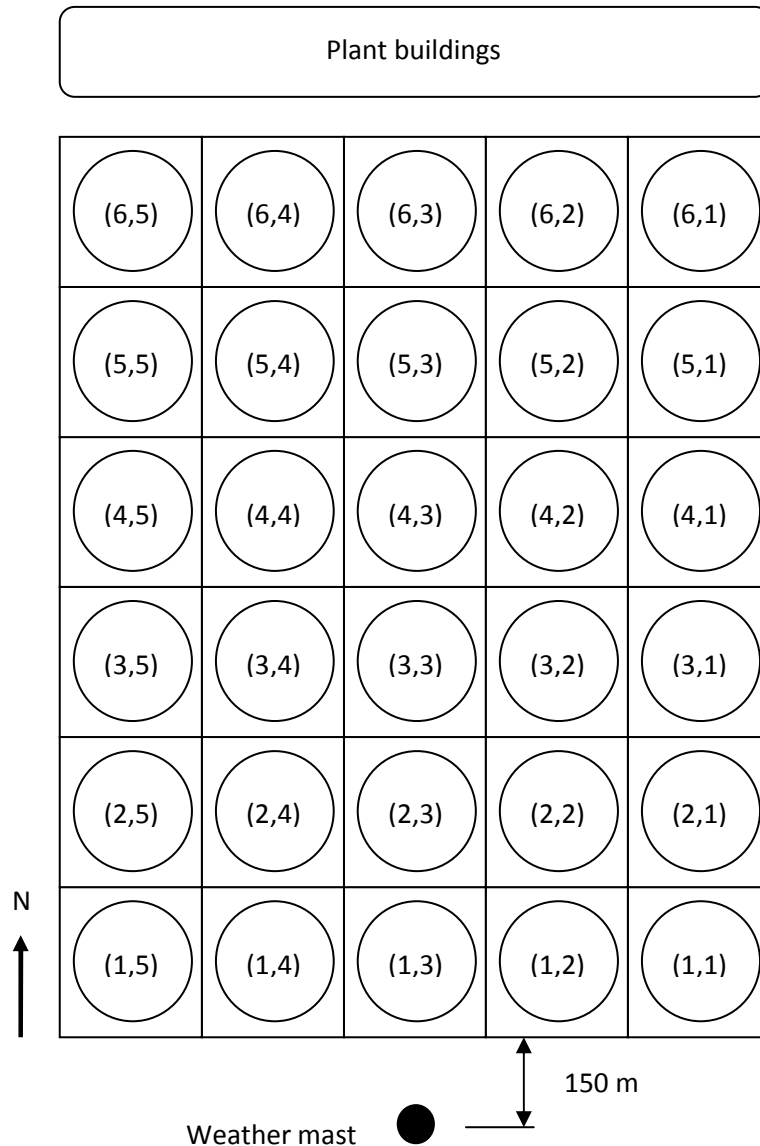
Figure G.1: **El Dorado ACSC layout and fan numbering scheme**

Ambient temperature and wind velocity measurements were recorded at elevations of 2 m, 5 m and 11 m above ground level on a weather mast located approximately 150 m to the south of the ACSC. Power law wind and temperature profiles of the form shown in equations (G.1)

and (G.2) respectively were fitted through the data. The wind profile was used to determine the nature of the input wind profile in the global flow field model, while the temperature profile was used to determine the ambient temperature at fan platform height for use in the simulations.

$$v_z = v_{ref} \left(z / z_{ref} \right)^b \tag{G.1}$$

$$T_z = T_{ref} \left(z / z_{ref_T} \right)^{b_T} \tag{G.2}$$

The ambient temperature at fan platform height was used in the simulations since it was noticed that air is drawn into most of the fans from an average height corresponding approximately to the fan platform height, as illustrated in Figure G.2. The downstream fans draw air from a lower elevation but it can be seen that this elevation increases with wind speed. The use of the ambient air temperature at fan platform height as the bulk fluid temperature in the numerical simulations is therefore a reasonable approximation especially at higher wind speeds.

Fan (1,3)   Fan (3,1)   Fan (5,3)

(a)

Fan (1,3)   Fan (3,1)   Fan (5,3)

(b)
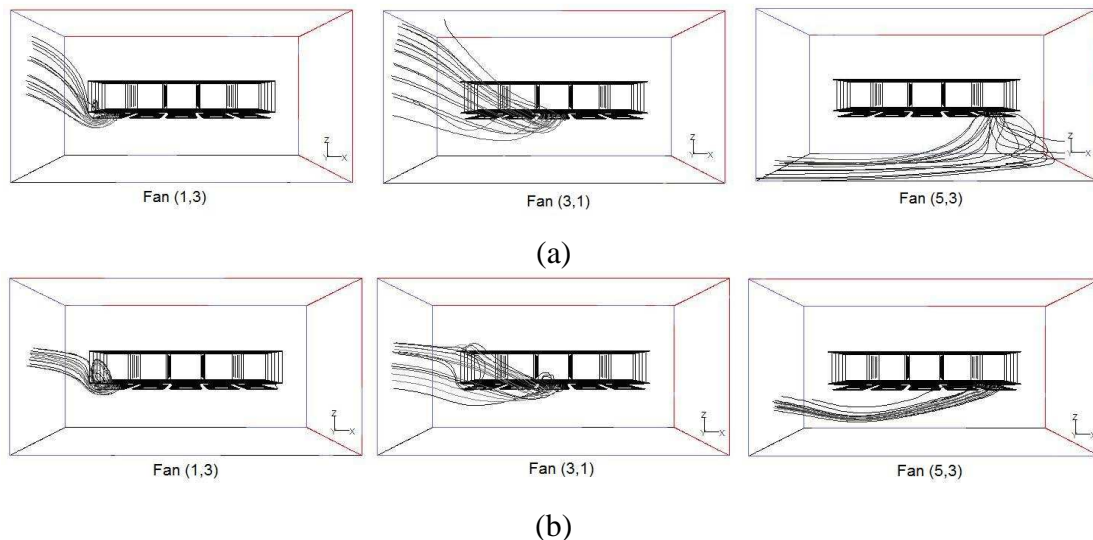
Figure G.2: Illustration of the source elevation of the air for certain fans for straight-flow wind speeds of (a) $v_w = 3$ *m/s* **and (b)** $v_w = 9$ *m/s*

The wind direction used in the numerical simulations is taken as the average of the directions recorded at the different elevations over the time period in question. The steam temperature under ideal operating conditions is determined using equations (4.1) and (4.2). The actual steam temperature, measured at the turbine exhaust and used for comparison with the numerical results, is taken as the average of the temperatures measured over the period in question.

G.1   Test period 1 (TP1)

Test period 1 is a 20 minute period between 21:37 and 21:59 on 14 September 2007.
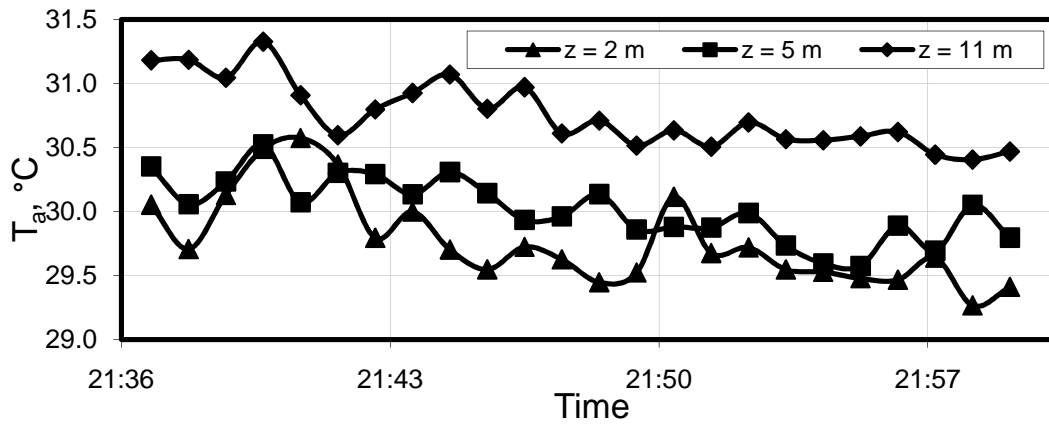
Figure G.3:   **Ambient temperature data recorded for TP1**
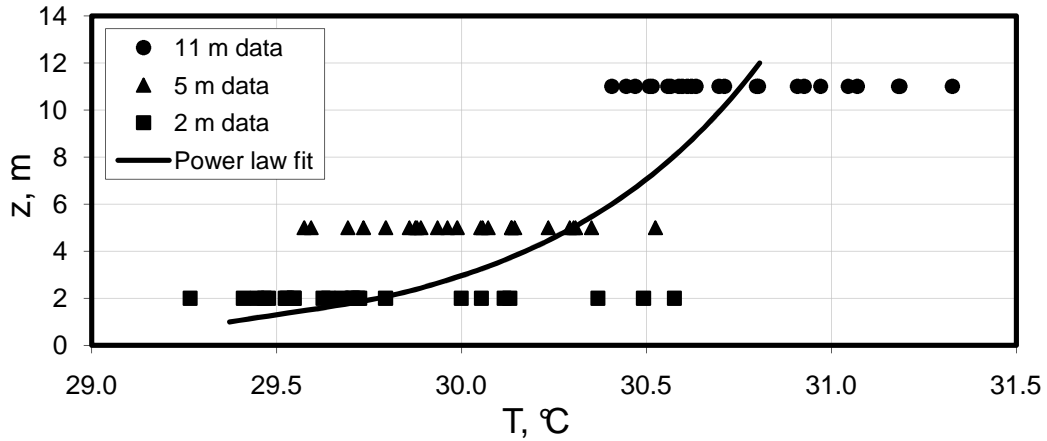
Figure G.4:   **Power law fit through temperature data for TP1**
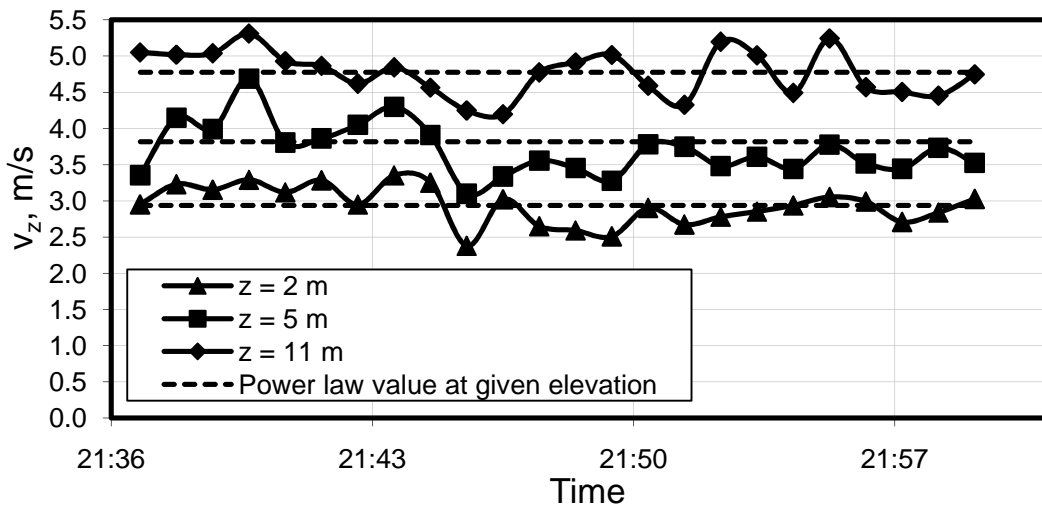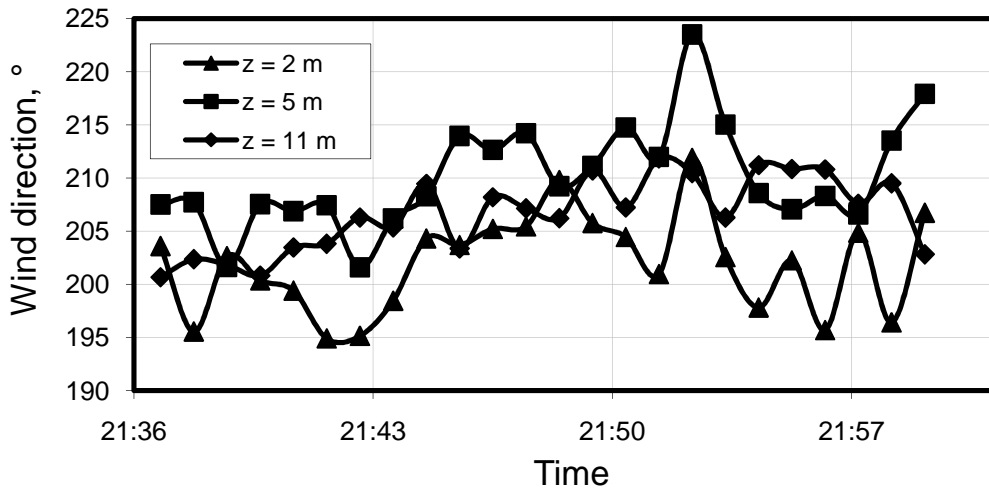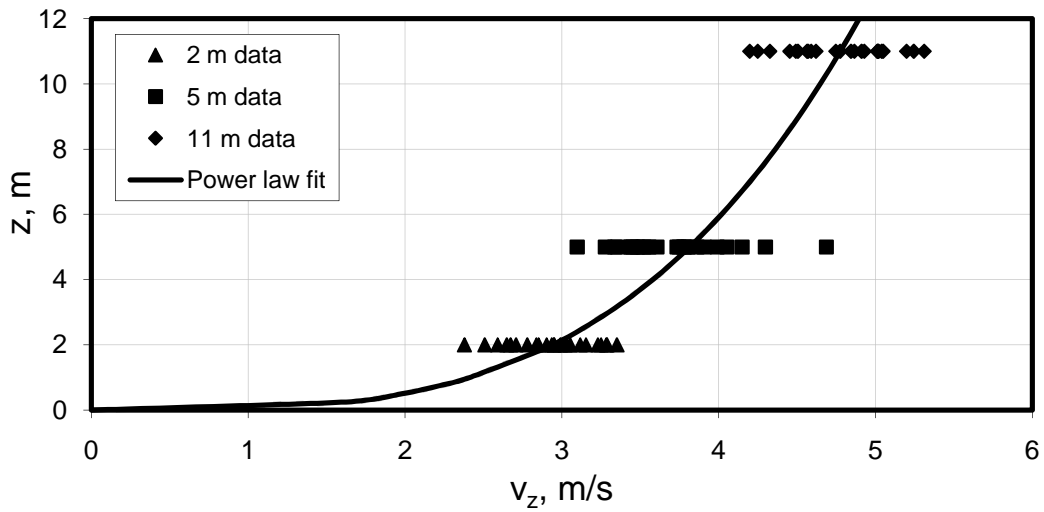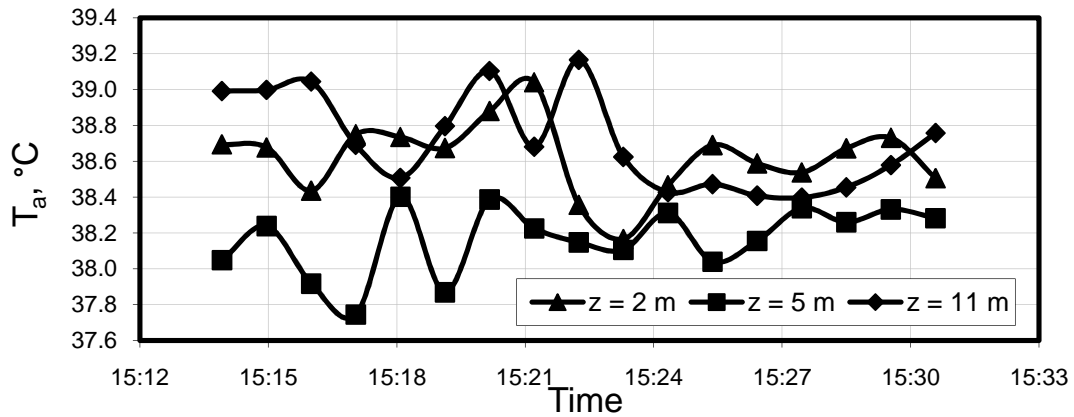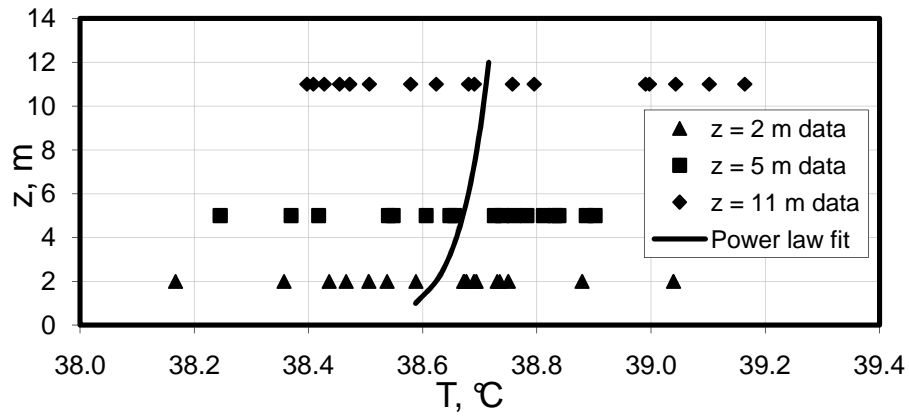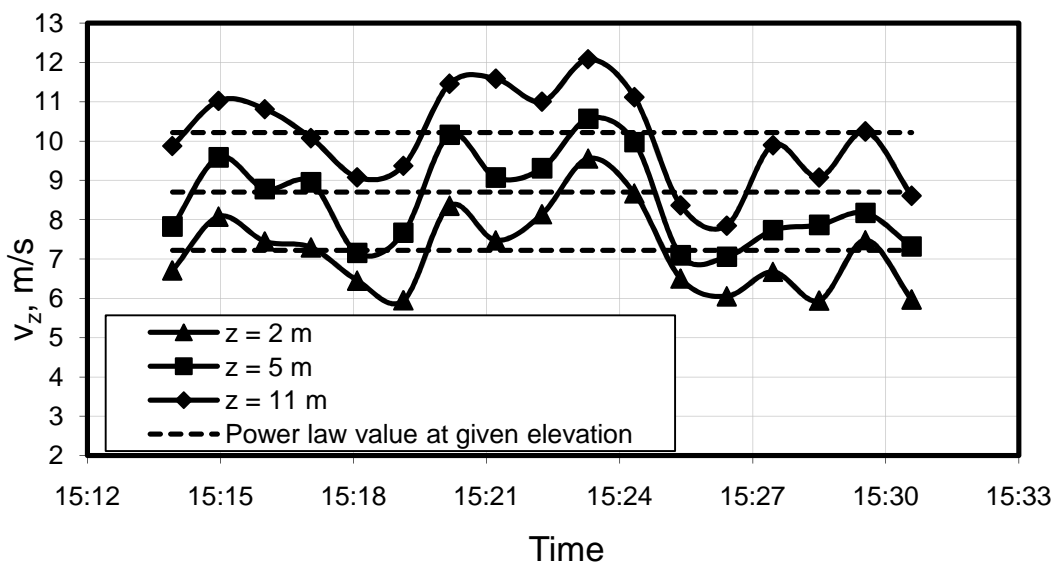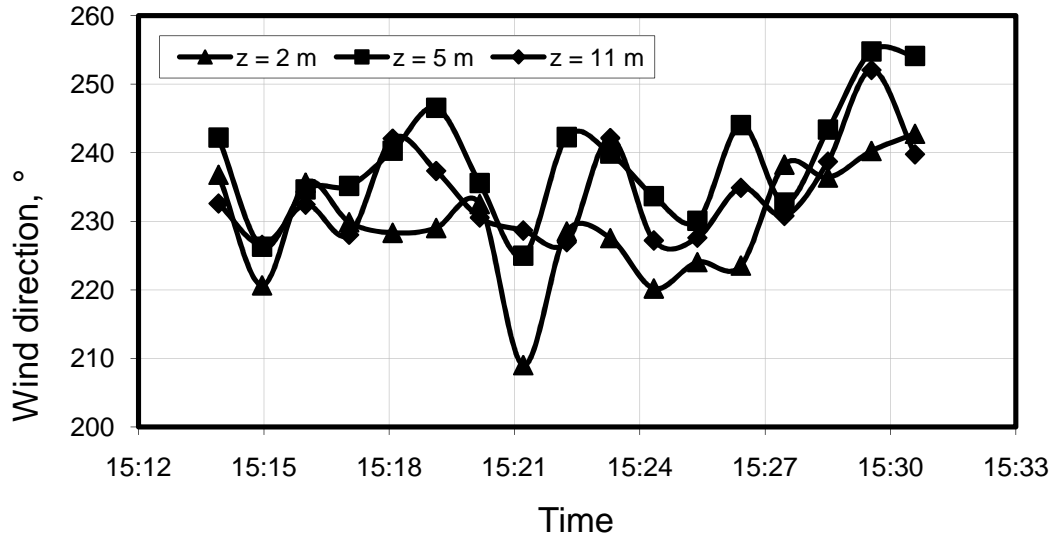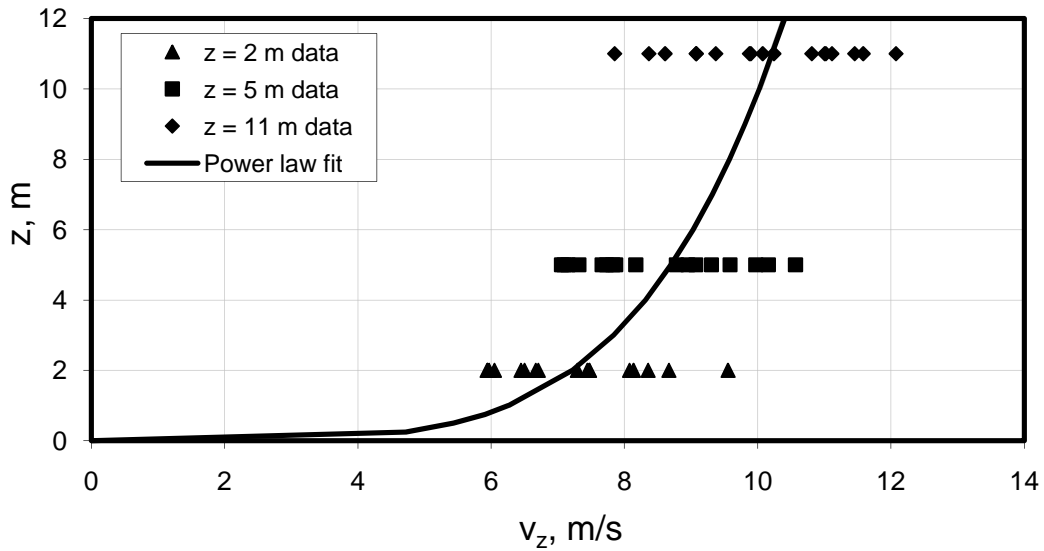
Figure G.5:   **Wind speed data recorded for TP1**

91

Figure G.6: **Wind direction data recorded for TP1**

Figure G.7: **Power law fit through wind data for TP1**

G.2 Test period 2 (TP2)

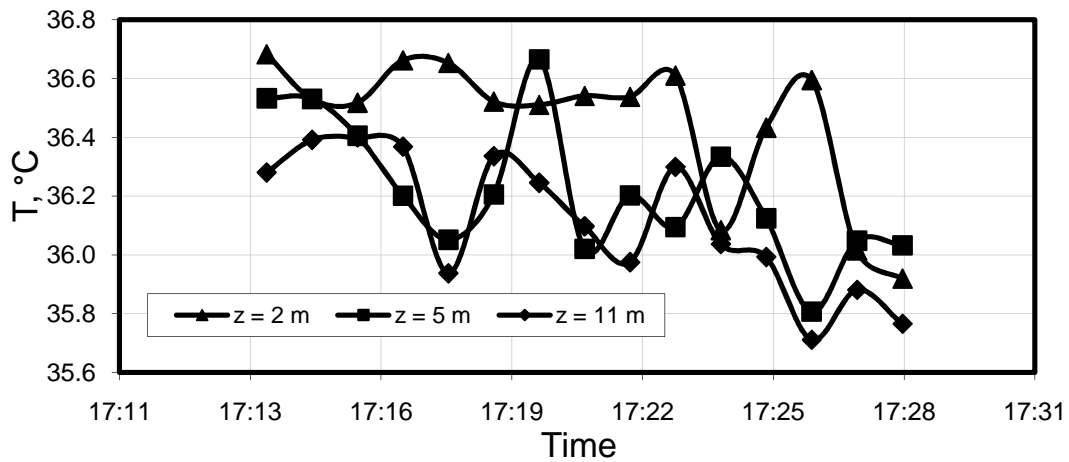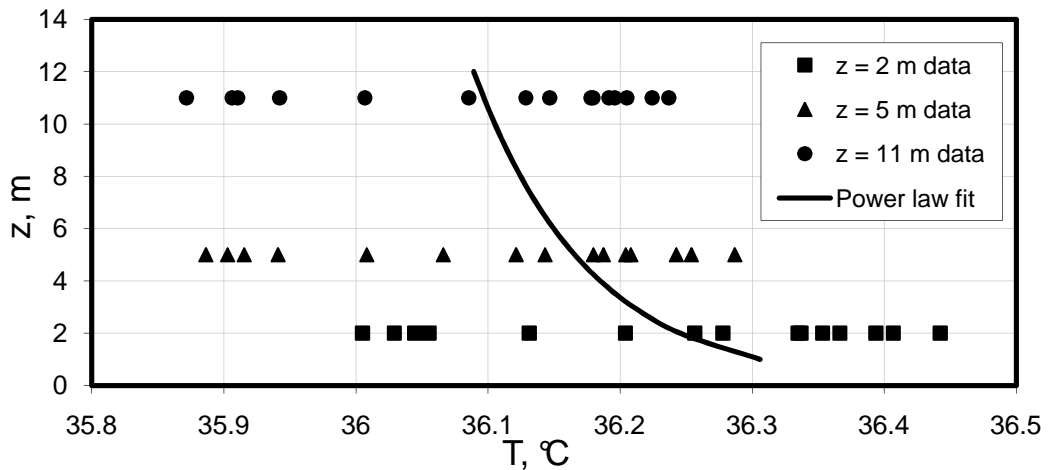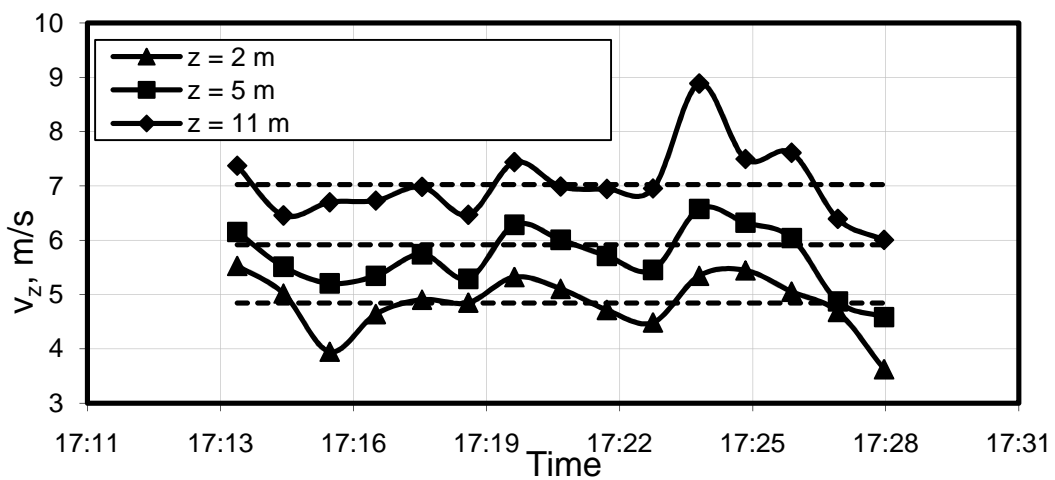Test period 2 is a 17 minute period between 15:14 and 15:31 on 14 September 2007.

Figure G.8: **Ambient temperature data recorded for TP2**

Figure G.9: **Power law fit through temperature data for TP2**
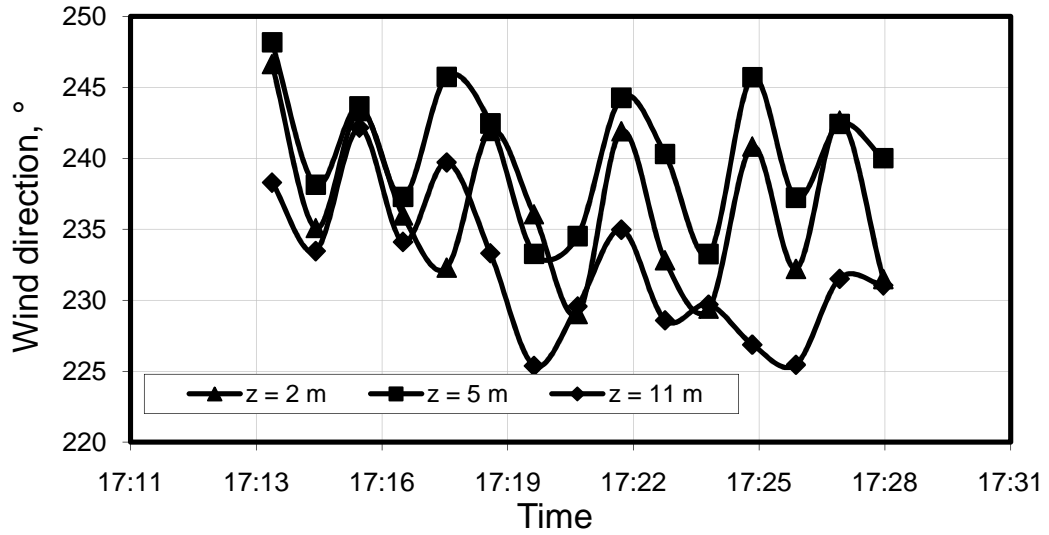

Figure G.10: **Wind speed data recorded for TP2**

Figure G.11:   **Wind direction data recorded for TP2**

Figure G.12:   **Power law fit through wind data for TP2**

G.3   Test period 3 (TP3)

Test period 3 is a 14 minute period between 17:14 and 17:28 on 15 September 2007.

Figure G.13: **Ambient temperature data recorded for TP3**
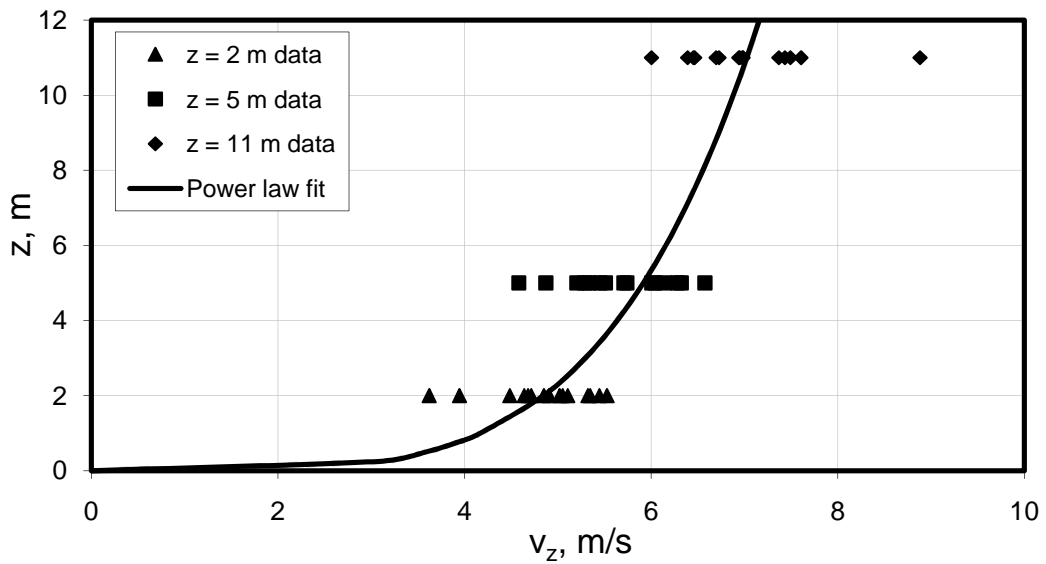
Figure G.14: **Power law fit through temperature data for TP3**

Figure G.15: **Wind speed data recorded for TP3**

95

Figure G.16: **Wind direction data recorded for TP3**

Figure G.17: **Power law fit through wind data for TP3**

G.4   Test period 4 (TP4)

Test period 4 is a 14 minute period between 17:28 and 17:43 on 17 September 2007.
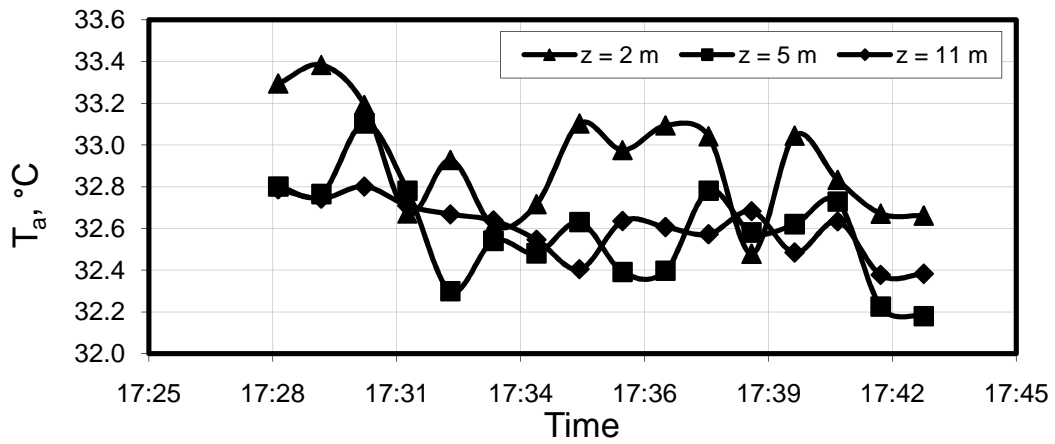

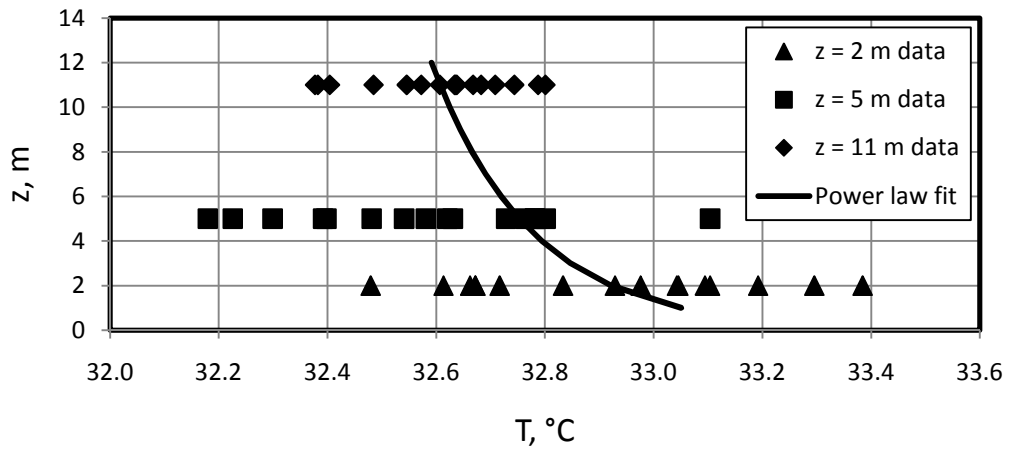**Figure G.18:**   **Ambient temperature data recorded for TP4**

Figure G.19:   **Power law fit through temperature data for TP4**

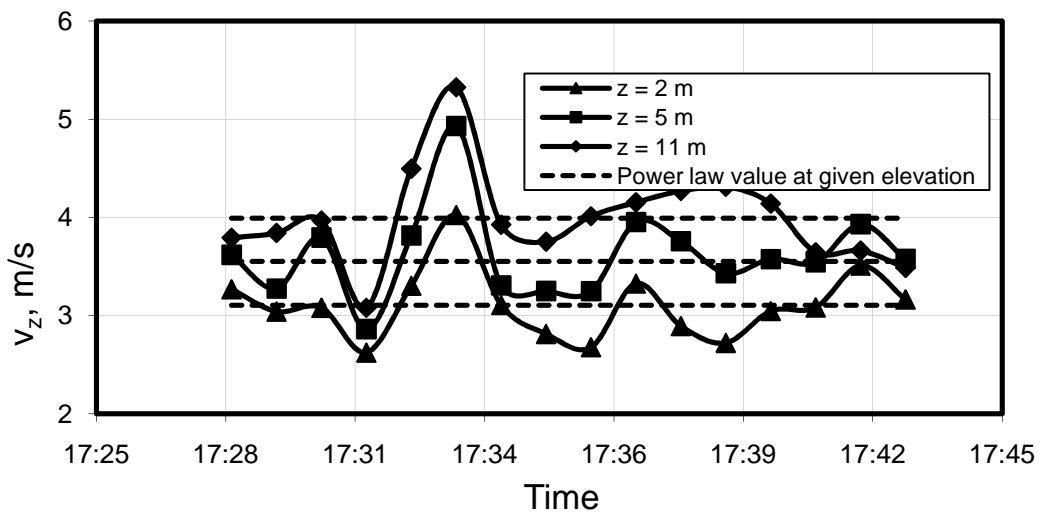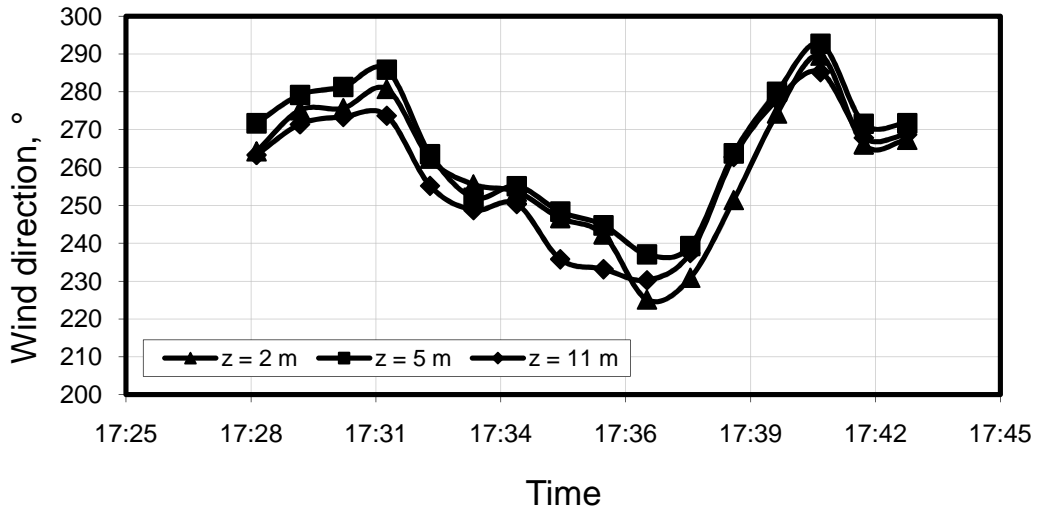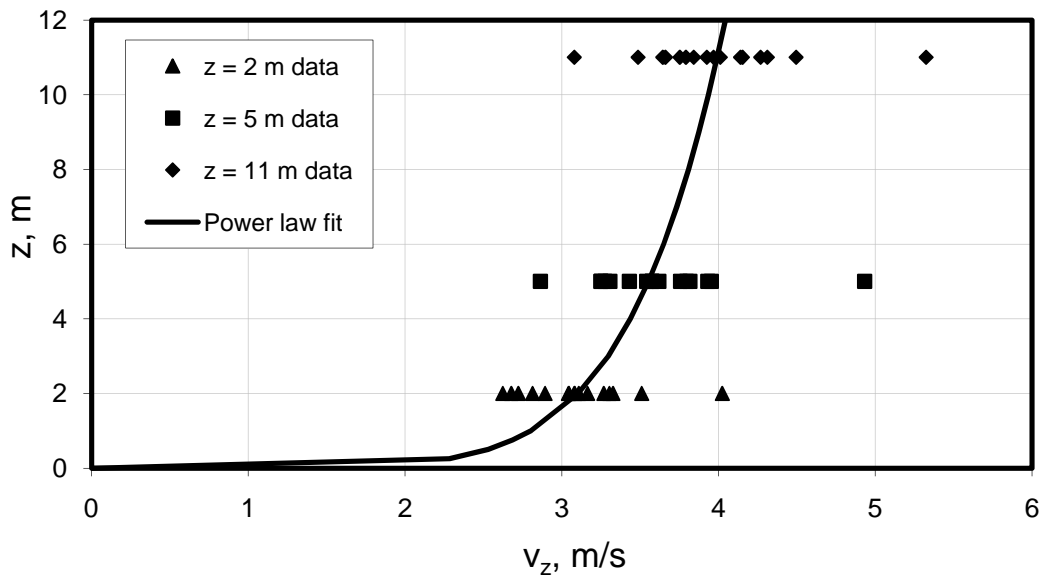**Figure G.20:**   **Wind speed data recorded for TP4**

Figure G.21:   **Wind direction data recorded for TP4**

Figure G.22:   **Power law fit through wind data for TP4**

G.5 Power law profiles for wind and temperature data

The following power law equations, described by equations (G.1) and (G.2), were fitted through the wind and temperature data presented in this section. In equation (G.1) v_{ref} is the average wind velocity over the test period measured at a height of $z_{ref} = 11\ m$ in equations (G.3), (G.5), (G.7) and (G.9). The average temperature, T_{ref} in Kelvin, measured at an elevation of $z_{refT} = 2\ m$, over the test period in question is used in equations (G.4), (G.6), (G.8) and (G.10).

$$v_{z(TP1)} = 4.7764(z/11)^{0.2850}, m/s \tag{G.3}$$

$$T_{z(TP1)} = 302.4559(z/2)^{0.001278} - 273.15, °C \tag{G.4}$$

$$v_{z(TP2)} = 10.2197(z/11)^{0.2040}, m/s \tag{G.5}$$

$$T_{z(TP2)} = 311.5336(z/2)^{0.000165} - 273.15, °C \tag{G.6}$$

$$v_{z(TP3)} = 6.8169(z/11)^{0.2719}, m/s \tag{G.7}$$
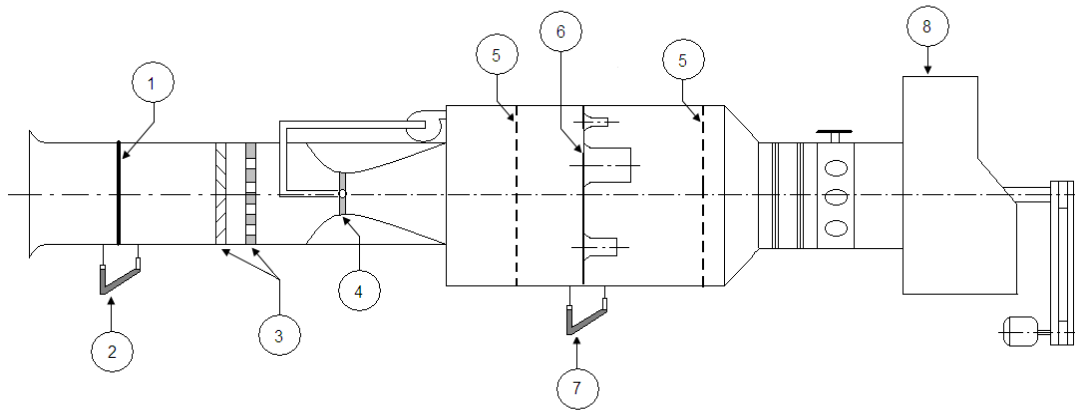
$$T_{z(TP3)} = 309.6110(z/2)^{-0.00028} - 273.15, °C \tag{G.8}$$

$$v_{z(TP4)} = 3.9915(z/11)^{0.1475}, m/s \tag{G.9}$$

$$T_{z(TP4)} = 306.2702(z/2)^{-0.0006} - 273.15, °C \tag{G.10}$$

Appendix H - Wind screen material tests

The wind tunnel test setup used to determine the wind screen material loss coefficient is illustrated in Figure H.1 and described thereafter (Kröger, 2004).

Figure H.1: **Wind tunnel test setup**

Air is drawn through the rounded inlet, where the drybulb temperature is measured, and through a sample of the wind screen material at (1) under the influence of a radial fan (8).The static pressure difference across the screen is measured at points located in the duct wall at (2). After passing through the screen, the air moves through two sets of mixers at (3) and a venturi in which a sampling tube is located at (4). The mixers and sampling tube are used to allow for accurate measurement of the air temperature in this section of the wind tunnel. The air mass flow rate is determined by measuring the static pressure drop at (7) across one or more elliptical nozzles mounted in a plate at (6). The nozzle plate is located between two perforated plates (5). The mass flow rate through the tunnel is given by equation (H.1).

$$m_a = C_n \phi_g Y A_n \sqrt{2\rho_a \Delta p_n} \qquad\qquad\text{(H.1)}$$

A_n and $\varDelta p_n$ are the nozzle cross sectional area and the pressure drop across the nozzle plate respectively. The nozzle coefficient of discharge, C_n, is a function of the nozzle Reynolds number, Re_n, as illustrated in equations (H.2) - (H.4).

For *30 000 < Re_n < 100 000*

$$C_n = 0.945803 + 6.37817 \times 10^{-7} \, Re_n - 4.65394 \times 10^{-12} \, Re_n^2 + 1.33514 \times 10^{-17} \, Re_n^3 \tag{H.2}$$

For *100 000 < Re_n < 350 000*

$$C_n = 0.9758 + 1.08 \times 10^{-7} \, Re_n - 1.6 \times 10^{-12} \, Re_n^2 \tag{H.3}$$

For *Re_n > 350 000*

$$C_n = 0.994 \tag{H.4}$$

The gas expansion factor, ϕ_g, is approximated using equation (H.5).

$$\phi_g = 1 - 3\Delta p_n / \left(4 p_{up} \, c_p / c_v \right) \tag{H.5}$$

where p_{up} is the pressure upstream of the nozzles and c_p/c_v = *1.4* for air.

The approach velocity factor, *Y*, for a compressible fluid is given by equation (H.6).

$$Y = 1 + 0.5 \left(A_n / A_{up} \right)^2 + 2 \left(A_n / A_{up} \right)^2 \Delta p_n / \left(p_{up} \, c_p / c_v \right) \tag{H.6}$$

where A_{up} is the area of the wind tunnel upstream of the nozzles.

The wind screen material loss coefficient is determined according to equation (H.7).

$$K_{sc} = 2\Delta p_{sc} / \rho_a v_{sc}^2 \tag{H.7}$$

where v_{sc} is the flow velocity through the screen, as given by equation (H.8) where A_{sc} is the screen material sample cross sectional area.

$$v_{sc} = m_a / \rho_a A_{sc} \tag{H.8}$$

The test results for the 55% and 65% closed area screen materials are illustrated in Figure H.2. The 90% closed area screen material behaved as a solid obstruction to the flow.
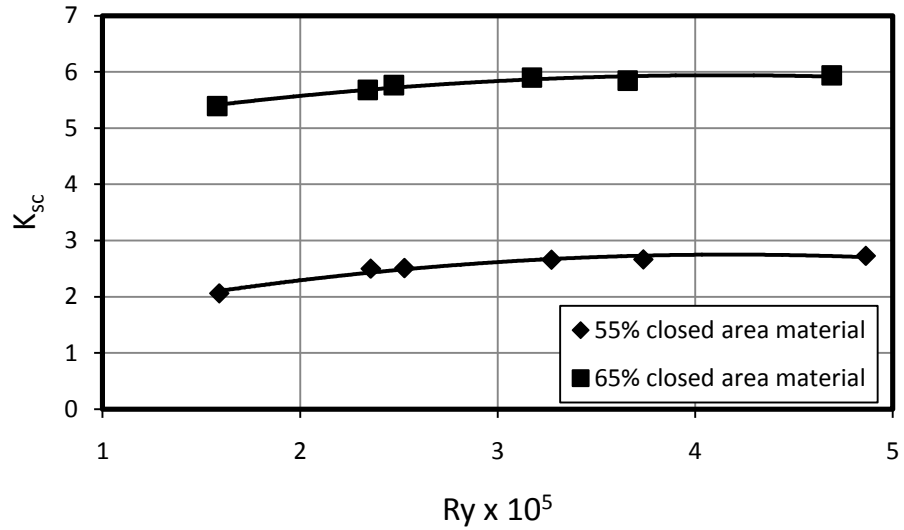
Figure H.2: **Wind screen material loss coefficients**

The screen material loss coefficients are very near to constant values and were subsequently modelled as such to reduce the computational requirements of the analyses carried out in this study. The average characteristic flow parameter through the screens is typically less than $Ry = 2.0 \times 10^5$ m^{-1} and values of $K_{sc} = 2$ and $K_{sc} = 5$ were selected for the 55% and 65% closed area screen materials respectively.